POLITECNICO DI TORINO
Repository ISTITUZIONALE

# Toward closed-loop quality assurance in powder bed fusion additive manufacturing: Defect detection, machine learning, and computational modeling

*Original*
Toward closed-loop quality assurance in powder bed fusion additive manufacturing: Defect detection, machine learning, and computational modeling / Taghian, M., Pilehvar Meibody, A., Saboori, A., Iuliano, L.. - In: JOURNAL OF MANUFACTURING PROCESSES. - ISSN 1526-6125. - 160:(2026), pp. 50-81. [10.1016/j.jmapro.2026.01.026]

*Availability:*
This version is available at: 11583/3011248 since: 2026-05-22T09:10:57Z

*Publisher:*
Elsevier Ltd

*Published*
DOI:10.1016/j.jmapro.2026.01.026

*Terms of use:*

This article is made available under terms and conditions as specified in the corresponding bibliographic description in the repository

*Publisher copyright*

(Article begins on next page)

13 November 2026

Journal of Manufacturing Processes 160 (2026) 50–81

Contents lists available at ScienceDirect

Journal of Manufacturing Processes

journal homepage: www.elsevier.com/locate/manpro

Review article

# Toward closed-loop quality assurance in powder bed fusion additive manufacturing: Defect detection, machine learning, and computational modeling

Mohammad Taghian [a,b], Ali Pilehvar Meibody [c,*], Abdollah Saboori [a,b,**], Luca Iuliano [a,b]

[a] Department of Management and Production Engineering, Politecnico di Torino, Corso Duca Degli Abruzzi 24, 10129, Turin, Italy
[b] Integrated Additive Manufacturing Center (IAM@PoliTo), Politecnico di Torino, Corso Castelfidardo 51, 10129, Turin, Italy
[c] Department of Applied Science and Technology, Politecnico di Torino, Corso Duca Degli Abruzzi 24, 10129, Turin, Italy

ARTICLE INFO

*Keywords:*
Additive manufacturing
Powder bed fusion
Defect detection
Multiscale modeling
Machine learning
Process monitoring
Reliability

ABSTRACT

Powder Bed Fusion (PBF) is a critical enabling technology in metal additive manufacturing (AM) to produce high-performance components deployed in extreme environments, including aerospace, energy, and biomedical applications. However, internal defects, such as lack of fusion porosity, gas-entrapped pores, and keyhole-induced voids continue to impose limitations on structural integrity, fatigue life, and process reliability. Achieving defect-free manufacturing under demanding performance requirements necessitates advanced detection and control strategies. Several recent reviews have addressed either in-situ monitoring techniques or machine-learning-based quality analytics in PBF, but typically in isolation. By contrast, this work provides an integrated review of defect detection across the PBF process chain, with emphasis on in-situ sensing, ex-situ characterization, machine learning-based classification, and mechanistic, numerical, and simulation approaches across micro-, meso-, and macro-scales. Particular focus is placed on computational models that capture critical physical phenomena at different scales, providing insight into defect formation and mitigation in PBF processes. The article also identifies current research gaps and outlines future directions for developing robust defect detection frameworks that support the qualification of AM components for mission-critical and extreme applications. These insights contribute to advancing the state-of-the-art in high-reliability additive manufacturing and accelerating its industrial adoption.

*Abbreviations:* AE, Acoustic Emission; AES, Acoustic Emission Spectroscopy; AM, Additive Manufacturing; AUC, Area Under the Curve; ANN, Artificial Neural Networks; CA, Cellular Automata; CSI, Coherence Scanning Interferometry; CMOS, Complementary Metal-Oxide-Semiconductor; CT, Computer Tomography; CFD, Computational Fluid Dynamics; CNN, Convolutional Neural Networks; CAD, Computer-Aided Design; CCD, Charge-Coupled Devices; DT, Decision Trees; DCNN, Deep Convolutional Neural Network; DNN, Deep Neural Network; DBSCAN, Density-Based Spatial Clustering with the Application of Noise; DEM, Discrete Element Method; DED, Directed Energy Deposition; EB-PBF, Electron Beam Powder Bed Fusion; EM, Expectation Maximization method; FE, Finite Element; FV, Finite Volume; GEPs, Gas-Entrapped Pores; GAN, Generative Adversarial Neural Network; HPC, High-Performance Computing; HDGPN, Hybrid Deep Generative Prediction Network; ICA, Independent Component Analysis; IR, Infrared; KNN, K-Nearest Neighbors; KH, Keyhole; KED, Knife Edge Detector; LED, Linear Energy Density; LoF, Lack of Fusion; LBM, Lattice Boltzmann method; L-PBF, Laser Powder Bed Fusion; LU, Laser Ultrasonic; LR, Linear Regression; ML, Machine Learning; MD, Molecular Dynamics; MLP, Multi-Layer Perceptron; NIR, Near-Infrared; NDT, Non-Destructive Testing; OM, Optical Microscopy; OCT, Optical Coherence Tomography; PF, Phase Field; PBF, Powder Bed Fusion; PCA, Principal Component Analysis; RF, Random Forests; RL, Reinforcement Learning; SLM, Selective Laser Melting; SOM, Self-Organizing Map; SSL, Semi-supervised Learning; SVD, Singular Value Decomposition; SPH, Smoothed Particle Hydrodynamics; SRAS, Spatially Resolved Acoustic Spectroscopy; SVM, Support Vector Machines; SAWs, Surface Acoustic Waves; UT, Ultrasonic Testing; XCT, X-ray Computed Tomography; YOLO, You Only Look Once.

* Corresponding author.
** Correspondence to: A. Saboori, Department of Management and Production Engineering, Politecnico di Torino, Corso Duca Degli Abruzzi 24, 10129, Turin, Italy.
*E-mail addresses:* alipilehvar1999@gmail.com (A. Pilehvar Meibody), abdollah.saboori@polito.it (A. Saboori).

https://doi.org/10.1016/j.jmapro.2026.01.026
Received 11 November 2025; Received in revised form 25 December 2025; Accepted 11 January 2026
Available online 21 January 2026
1526-6125/© 2026 The Authors. Published by Elsevier Ltd on behalf of The Society of Manufacturing Engineers. This is an open access article under the CC BY license (http://creativecommons.org/licenses/by/4.0/).

## 1. Introduction

Powder Bed Fusion (PBF) has emerged as one of the most important metal additive manufacturing (AM) processes for producing geometrically complex, high-performance components in aerospace, energy, automotive, and biomedical industries. Its layer-wise consolidation strategy enables unprecedented design freedom and near-net-shape manufacturing, while offering the potential for part consolidation and reduced material waste. Despite these advantages, the widespread adoption of PBF for safety-critical and load-bearing applications remains limited by persistent challenges related to process reliability, reproducibility, and internal defect formation [1,2]. While this review addresses PBF in general, particular emphasis is placed on L-PBF, as it dominates current research on in-situ monitoring and machine-learning-based defect detection.

Among the various limitations of PBF, internal defects such as lack-of-fusion (LoF) porosity, gas-entrapped pores (GEPs), and keyhole-induced voids (KHs) represent the most critical barriers to achieving consistent mechanical performance. These defects act as stress concentrators, severely degrading fatigue life, fracture resistance, and long-term structural integrity. Their formation is governed by a complex interplay between process parameters, powder characteristics, melt-pool dynamics, and thermal gradients, making defect suppression through conventional parameter optimization alone highly inefficient and material-dependent [3,4].

When excessive energy is supplied to the powder material, KHs-shaped defects are formed in the melt pool, and their filling is mainly impaired by Marangoni flow and recoil pressure. This phenomenon is known as KH porosity. This defect tends to collapse because of its intrinsic instability, trapping inert shielding gas and creating usually round pores [5,6]. Typically characterized by small spherical voids, gas porosity may result from vaporized alloy elements, inherent porosity in the powder particles, or gas trapped within the shielding environment [7,8]. Porosity and LoF defects can adversely affect static and dynamic mechanical performance, limiting the application of AM components in mission-critical applications [9,10].

In addition, additively manufactured parts are associated with poor surface finish and tensile residual stresses, which worsen fatigue performance [11]. Several post-processing methods, such as heat treatment, hot isostatic pressing, and surface modification, have been used to overcome such problems and improve fatigue performance [11,12]. The reliable detection and precise characterization of internal defects are vital to ensure the quality and performance of AM components [13]. As these defect categories are classified, minimizing the requirement of extensive optimization of the process parameters is possible, which is usually laborious and time-consuming. This strategic approach to defect categorization also significantly improves AM parts' mechanical properties without the painstaking parameter-tuning process [14].

Against this backdrop, the present review aims to integrate these previously disparate threads into a cohesive framework for defect detection and control in L-PBF. We emphasize how understanding the physical mechanisms of defect formation can inform sensor interpretation and guide the development of hybrid physics-informed ML models. To the authors' knowledge, this is the first review to systematically link defect mechanisms, in-situ sensing, multiscale modeling, and ML-based classification within a unified perspective oriented toward closed-loop quality assurance in L-PBF. By critically examining current limitations and identifying emerging opportunities, this work seeks to support the transition from open-loop monitoring toward adaptive, self-corrective manufacturing strategies, enabling more reliable production of mission-critical AM components.

## 2. Overview of the PBF methods

Powder Bed Fusion (PBF) is a frequently used metal AM technique utilized for the production of high-performance components in the aerospace, biomedical, and automotive industries [15]. In PBF, thin layers of metal powder are distributed over a build platform and selectively melted by a focused energy source, such as a laser or an electron beam, in accordance with the digital model [16]. The primary alternatives, L-PBF and EB-PBF, mainly differ in their energy sources, processing atmospheres, and defect-formation behaviors, which are essential for real-time defect detection. Fig. 1(a) and (b) show the schematic illustration of each method regarding their energy sources and structures [17,18].

In L-PBF, the laser beam melts powder in an inert atmosphere, typically argon or nitrogen, maintaining oxygen levels below 1000 ppm to avoid oxidation. The selection of gas affects melt-pool stability and spatter generation, thereby affecting surface quality and the ability to detect defects [19]. For example, Ti-6Al-4V is highly sensitive to oxygen and nitrogen, while 316L stainless steel is less reactive [11]. Recent studies have proposed helium as an alternative gas to reduce spatter and stabilize the melt pool [12]. Gas composition and purity thus directly impact both defect formation and signal clarity in optical or thermal monitoring [13].

Defect types such as keyhole-induced porosity and lack-of-fusion (LoF) porosity originate from inappropriate energy input. High laser power and low scan speeds increase melt-pool depth and vaporization, promoting keyhole instability, while insufficient power or excessive speed produce LoF voids [20–23]. Optimal parameter ranges achieve dense microstructures, whereas extremes alter surface emissivity and monitoring response. For instance, higher scan speeds in NiTi alloys accelerate Ni evaporation, shifting phase-transformation behavior detectable via spectral monitoring [24].

Hatch spacing and layer thickness also influence overlap uniformity and signal consistency: narrow spacing increases overlap but may create convection-induced pores, while large spacing reduces intertrack bonding [25,26]. These relationships between process parameters and defect signatures provide the foundation for adaptive, sensor-assisted PBF control.

In EB-PBF, melting occurs under vacuum using a focused electron beam, which minimizes oxidation and residual stress while maintaining high density [27,28]. The vacuum environment benefits reactive materials such as titanium alloys and enables high deposition rates for large parts [29]. Advances in electron-beam guns and powder recycling have enhanced production capability [23], although higher energy input can still induce warping and surface roughness that affect post-build inspection [30,31]. For defect detection, EB-PBF relies primarily on electron-optical imaging, pyrometry, and beam-current analysis, as visible-light access is limited. Overall, both L-PBF and EB-PBF share common detection challenges—dynamic melt-pool behavior, layer-wise variations, and atmosphere-dependent signal sensitivity. Understanding these processing principles is essential for designing robust in-situ monitoring frameworks capable of identifying defect precursors during fabrication.

## 3. Defect formation mechanisms and their detection relevance in PBF

Defect formation in PBF arises from the complex interplay of process parameters, thermal gradients, melt-pool dynamics, and powder characteristics. Understanding these mechanisms is crucial not only for optimizing build quality but also for designing effective defect-detection and monitoring strategies, since each mechanism produces distinct thermal, optical, or geometric signatures that can be captured by in-situ sensors or ex-situ characterization tools.

At high energy densities, the melt pool transitions from conduction to the keyhole regime, where intense vaporization generates a deep depression within the liquid metal. The keyhole itself is a melt-pool phenomenon, but its instability during collapse can trap vapor and form keyhole-induced porosity [32]. Synchrotron imaging has revealed rapid oscillations in the keyhole walls and bubble nucleation that

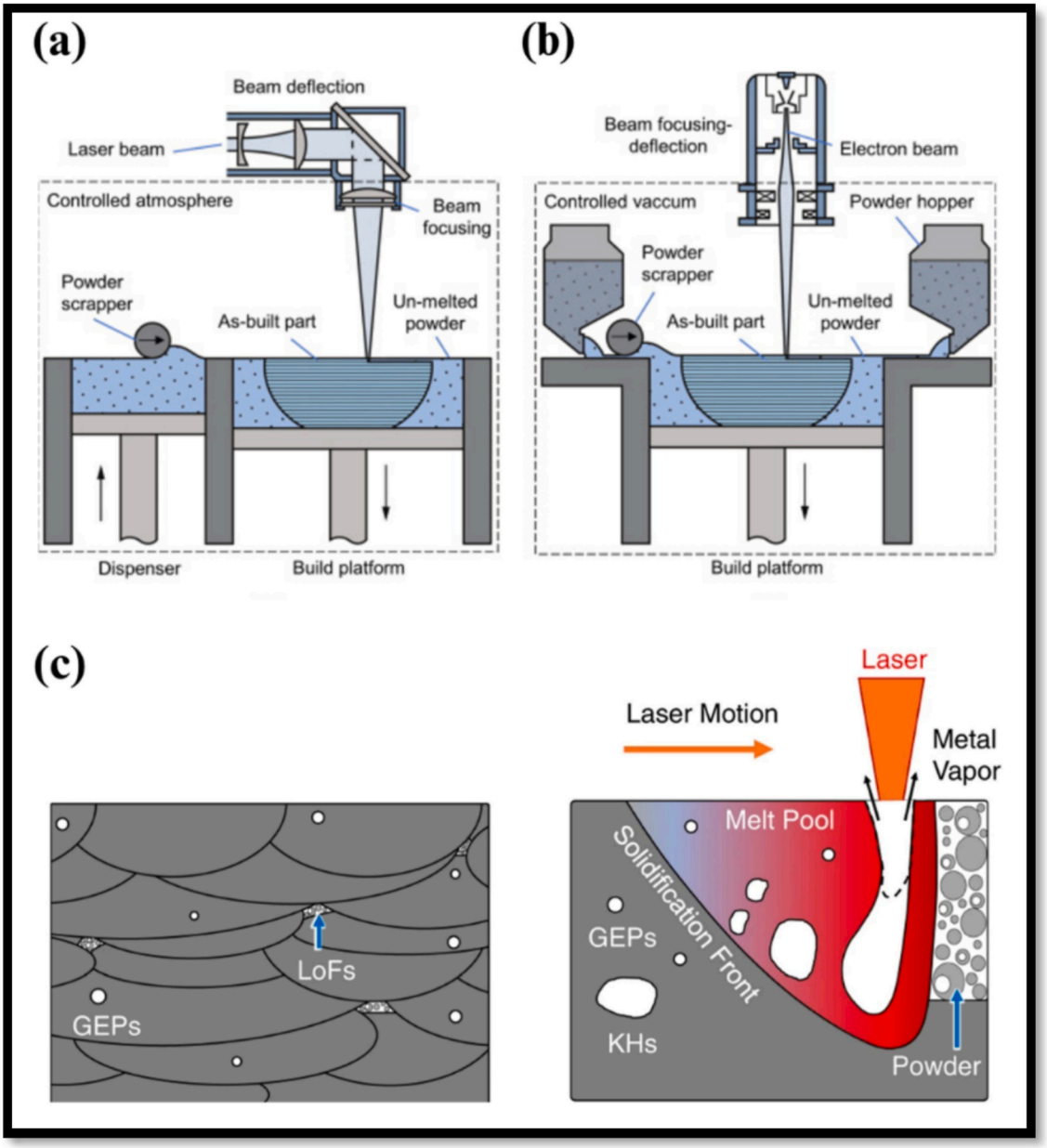



**Fig. 1.** The schematic illustration of two PBF machines: (a) L-PBF and (b) EB-PBF [47]. (c) Explanation of the formation of various defects in L-PBF [48].

stabilizes through gas diffusion or collapses to form subsurface pores [33]. Disturbances in shielding-gas flow or recoater motion can further localize these pores at cell boundaries [34]. Zhao et al. focused on time-resolved synchrotron X-ray imaging to show that KH-induced porosity can form before visible melt pool trenching is observed. The synchrotron imaging revealed that KH-induced porosity stem from vapor-induced instabilities that appear in the melt pool [35].

When the energy input is insufficient, incomplete melting and poor overlap between adjacent tracks or layers produce LoF porosity [9]. These elongated, crescent-shaped voids align with the scan path and act as stress concentrators that severely reduce mechanical strength. LoF initiation has been statistically correlated with spatter redeposition that disturbs powder uniformity [36]. Analytical models express the fusion condition through a LoF index, the ratio of melt-pool depth to layer thickness, where values below unity indicate incomplete bonding. For instance, Zhang et al. showed that for a given melt pool size, the critical parameter for achieving complete fusion is the minimum depth of overlap, denoted as $M_{d0}$ [37]. In-situ detection of LoF regions relies on reduced melt-pool temperature or height-map anomalies detected by thermography and optical imaging, while real-time control of laser power or scan speed can correct insufficient fusion [38].

Another important mechanism is preferential evaporation, caused by the selective loss of volatile alloying elements under excessive power density. In Ti-6Al-4V, aluminum depletion alters local composition and mechanical response [39] while in Ni-based superalloys, elements such as Al, Co, and Cr can evaporate by up to 1.2 at.% [40,41]; Klassen et al. reported as much as 8 at.% Al loss in Ti-6Al-4V [42]. It has been shown that keeping the LED between 0.1 and 0.2 J/mm can limit elemental losses to <0.5% in Ti-6Al-4V while still achieving complete melting and eliminating LoF defects [5]. Additionally, reducing the hatch distance and layer thickness increases the total exposure time of the material to high temperatures, further exacerbating evaporation. Thus, carefully balancing these parameters is essential to maintain the desired alloy composition [43]. Fig. 1(c) shows the schematic of the formation of different defects during L-PBF.

The formation of residual stress is another primary concern in PBF,

especially in L-PBF, due to the process's large thermal gradients and relatively high solidification rates [44]. Uneven cooling, resulting in tensile and compressive stresses, leads to distortion and cracking of the part. Residual stresses are classified as Type I: macroscale, Type II: grain-scale, and Type III: atomic-scale. Type I stresses dominate PBF and tend to warp larger components [45]. Residual stress can be influenced directly by the scan strategy and the hatch spacing. Longer scan lines lead to larger thermal gradients, which result in more significant residual stresses. Using smaller part areas, islands, or alternating scan pattern directions can significantly reduce the thermal gradient and residual stresses [46].

In summary, defect formation in PBF is governed by energy-balance instability, melt-pool overlap, vaporization kinetics, and thermal-stress evolution. Each mechanism leaves measurable signatures: transient thermal and optical variations indicate keyhole instability; cooler melt pools and height deficits reveal LoF; spectral and compositional shifts signal evaporation; and geometric distortions reflect residual stress buildup.

## 4. In-situ and ex-situ sensing techniques for defect detection

AM uses two main imaging methods for defect identification and process monitoring: ex-situ (post-process) and in-situ imaging. Both strategies have unique advantages, and they also have some restrictions. In-situ imaging becomes especially useful because of its capacity to provide opportunities for real-time monitoring during the AM process. This approach directly observes phenomena such as changes in material properties, structural dynamics, and changing process conditions. In-situ imaging gives rapid insights into the production process by collecting and evaluating data in the operating environment, allowing errors to be detected as they occur.

On the other hand, ex-situ imaging provides extensive post-process characterization of the constructed objects, but it doesn't have the speed of real-time data. This process often includes high-resolution photography and analysis of the final component's mechanical and structural characteristics. Ex-situ techniques have long been used in industry for quality control, research, and development. A range of advanced sensors, including acoustic sensors [49], high-resolution optical cameras [50], high-speed cameras [51], infrared (IR) thermography [52], IR cameras [53], and optical tomography [54], are employed to monitor the AM process, either during or after production. These technologies enable detailed insights into crucial phenomena occurring within the powder bed and melt pool, such as surface topography (pre- and post-exposure), spattering, balling, pore formation, cracking, and deformation.

Furthermore, these sensors are essential for recognizing certain defect types and for more accurate identification and characterization. These sophisticated monitoring systems are critical because they provide crucial data for better process control. This review will go over each instrumentation category in detail, evaluating the sensor types and how they contribute to improving the reliability and precision of AM technologies.

### 4.1. Optical-based monitoring

Electromagnetic wave-based optical technologies in the visible band are widely used as in-situ monitoring systems in AM. These methods apply multiple detector types to capture high-resolution images of the process and provide critical information about material deposition and quality assurance. Real-time visual data extracts structural characteristics like component height, width, and POSSIBLE distortions due to the compaction of the assembly through optical techniques. However, vision sensing has proven to be a cost-effective approach for tracking individual layers' geometric accuracy and ensuring the parts' structural stability and dimensional accuracy during the AM process [55]. Examples of typical optical monitoring configurations are shown in Fig. 4(a), including high-resolution camera systems and schematic setups integrated into L-PBF machines [56]. Surface images are typically obtained by CMOS or CCD cameras. These techniques are best suited for detecting gross defects, such as interruptions in the powder supply or surface defects. The process starts by exposing the material's surface to a light source, like a ring or dome configuration. The camera then captures the light reflected off the surface, generating a grayscale image that reveals the surface roughness and features. The result is represented by an integer pixel, where each pixel corresponds to a separate intensity level (gray value) of the surface. The raw image data is typically compressed into formats like PNG or JPG to process it further.

Modern image processing algorithms can extract surface texture information, revealing key surface characteristics such as topography, defects, and scan-path patterns. In the context of AM, these features can be continuously monitored to identify process instabilities or deviations in the beam trajectory that may influence surface quality. This enables dynamic surface defect detection and adaptive quality control during PBF operations [57].

As mentioned, CCD or CMOS cameras equipped with suitable waveband filters are standard visual sensing devices used in AM. The precision and efficiency of these visual sensing devices are strongly dependent on camera resolution, which is crucial in showing dimension input during the AM process. This technology is essential for monitoring the powder layer recoating process since it allows the detection of any anomalies or disruptions in the powder bed. These devices facilitate the overall quality of the construction by providing exact visual data that ensures the consistency of powder distribution.

In-situ optical imaging has been extensively employed to investigate the melt pool dynamics during AM processes. By leveraging advanced image processing techniques, significant research has focused on analyzing the size and behavior of the melt pool [58]. Beyond typical photography, remarkable technologies such as laser coaxial CMOS cameras and trinocular optical detectors, which consist of three separate components, are used to record molten pool features [59].

Stereo vision methods provide a viable method for recreating the melt pool's three-dimensional structure. This approach relies on triangulation to identify the location of objects by looking at matching points obtained from two cameras [60]. Several studies have focused on developing in-situ techniques for rapid defect localization and quantification through visual sensing [61]. Felix et al. introduced a high-resolution optical monitoring system to detect layer deviation defects in L-PBF, integrating a 3D measurement system with a recoater-based line camera (Fig. 2(a)) [56]. By extracting brightness and periodicity data from superimposed images, they achieved a resolution of 5.97 μm/pixel (Fig. 2(b)). To further validate the relationship between the extracted image features and build quality, topographical data were collected ex-situ using the Alicona Infinite Focus system, as depicted in Fig. 2(c).

Optical monitoring offers high spatial resolution, low cost, and non-intrusive integration, making it effective for detecting surface defects such as recoating anomalies or layer shifts. However, it is limited to surface features, sensitive to spatter and lighting, and depends on camera resolution. These limitations are more pronounced in EB-PBF, where vacuum and high temperatures hinder visible-light imaging, whereas L-PBF benefits from stable optical access, making optical monitoring more practical.

### 4.2. Thermal-based monitoring systems

Thermal-based monitoring systems encompass infrared and near-infrared imaging as well as thermographic and pyrometric techniques. While all these approaches rely on detecting thermal radiation, they differ in terms of spectral range, measurement strategy, and application focus within additive manufacturing processes.

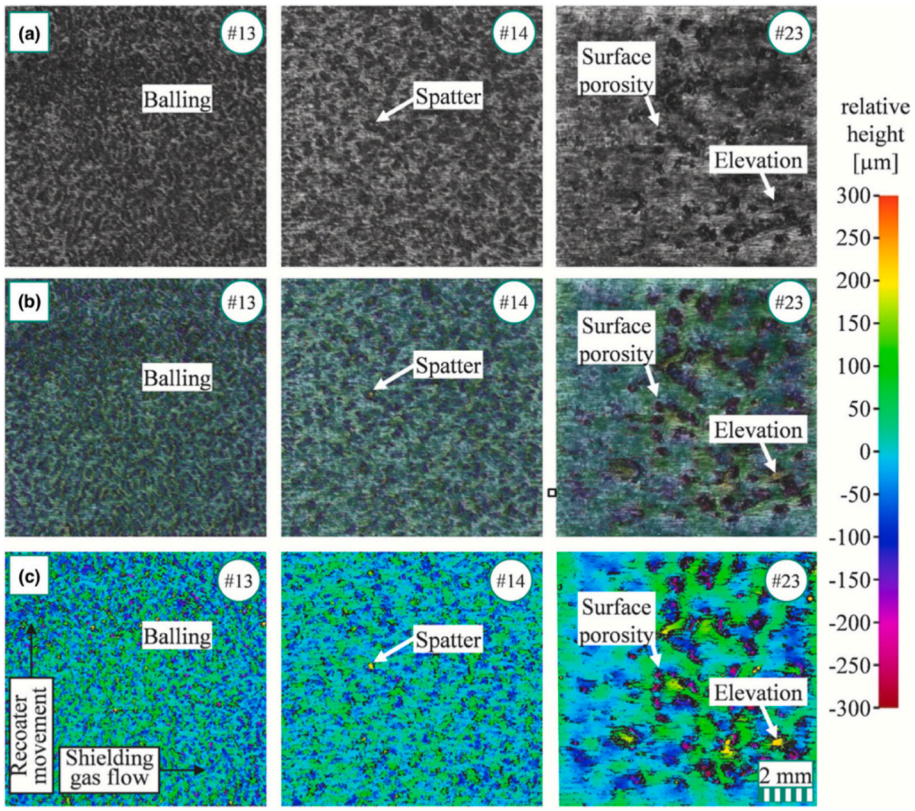



**Fig. 2.** Surface images of samples produced in the experiment: (a) captured in-situ using the camera system, (b) both superimposed images, and (c) a topographical image acquired ex-situ using an Alicona Infinite Focus, where "0" indicates the mean plane [56].

#### 4.2.1. *Infrared imaging and NIR-based monitoring*

CMOS and CCD cameras are commonly used for general defect detection in AM, such as the detection of discontinuities in powder supply operations. However, infrared (IR) cameras are more suitable for monitoring thermal fields and identifying pores and other defects caused by insufficient heat dissipation [57].

IR-based systems are especially useful in AM because they can record thermal data and diagnose subsurface defects like incomplete fusing or overheating, which optical systems cannot because these methods focus on surface characteristics. Unlike optical monitoring, IR systems provide insights into temperature distributions inside the process, providing more knowledge of thermal anomalies that may result in defect formation. Furthermore, IR cameras can perform well in high-energy laser interactions, where splatter and bright light may block traditional optical approaches.

IR radiation has wavelengths longer than visible light and is critical for obtaining comprehensive temperature data during research. This makes IR-based monitoring systems suitable for temperature measurement, defect identification, and melt pool monitoring in AM processes. When setting up an IR camera for such applications, selecting an appropriate camera type based on the required temperature range and resolution is critical to achieve accurate and effective AM monitoring.

Near-infrared (NIR) imaging has developed as an effective method for real-time defect detection during AM, and it offers vital insights into manufactured parts [62]. Craeghs et al. explored powder bed monitoring in the PBF process using optical imaging techniques, highlighting the wide range of thermal data accessible through this method [63]. While optical imaging operates similarly to thermal imaging, it circumvents the need for IR-specific sensors by leveraging the NIR spectral range of commercial cameras to estimate melt pool temperatures. Despite challenges in acquiring precise thermal measurements from optical data, melt pool irregularities can be effectively examined, offering valuable indirect insights into potential defect formation.

Criales et al. investigated the behavior of the melt pool in PBF by using in-situ video imaging during the processing of IN625 super alloy, which captured the dynamic character of the melt pool and provided a greater understanding of the process [58]. Mazzoleni et al. extended this by using a CMOS imaging system to collect visible and infrared wavelengths. They provided the capabilities of CMOS sensors to capture more precise melt pools utilizing the sensor's dynamic range in the IR spectrum [59]. Fig. 3(a) shows NIR pictures taken for both bulk and thin-wall geometries, demonstrating NIR imaging's capacity to detect minor differences in thermal behavior that could show defect development. Infrared monitoring provides the advantage of capturing subsurface thermal information, enabling the detection of incomplete fusion, overheating, or other heat-related defects that optical systems cannot observe. It is particularly robust under high-energy laser conditions, where spatter and bright light can obscure visible-light imaging. Limitations include lower spatial resolution compared with optical cameras and sensitivity to emissivity variations. While IR monitoring is widely applied in LPBF due to the controlled inert gas environment, EB-PBF's high-temperature vacuum poses challenges for thermal imaging, often requiring specialized IR or pyrometric sensors to obtain reliable data (Fig. 4(b)) [64].

#### 4.2.2. *Thermography and pyrometric techniques*

Thermography, a popular non-contact sensing technique, tracks temperature changes during AM. This technology detects infrared radiation generated by materials during processing and allows real-time temperature distribution monitoring. In AM, thermography is critical to discovering defects by analyzing temperature changes throughout the melting and solidification phases. Typically, an infrared camera is used to continually monitor the work area, gathering thermal data and creating dynamic thermal maps that show temperature variations between layers. These maps are analyzed to discover anomalies such as hotspots or inadequate heating, which might result in defects like pores,

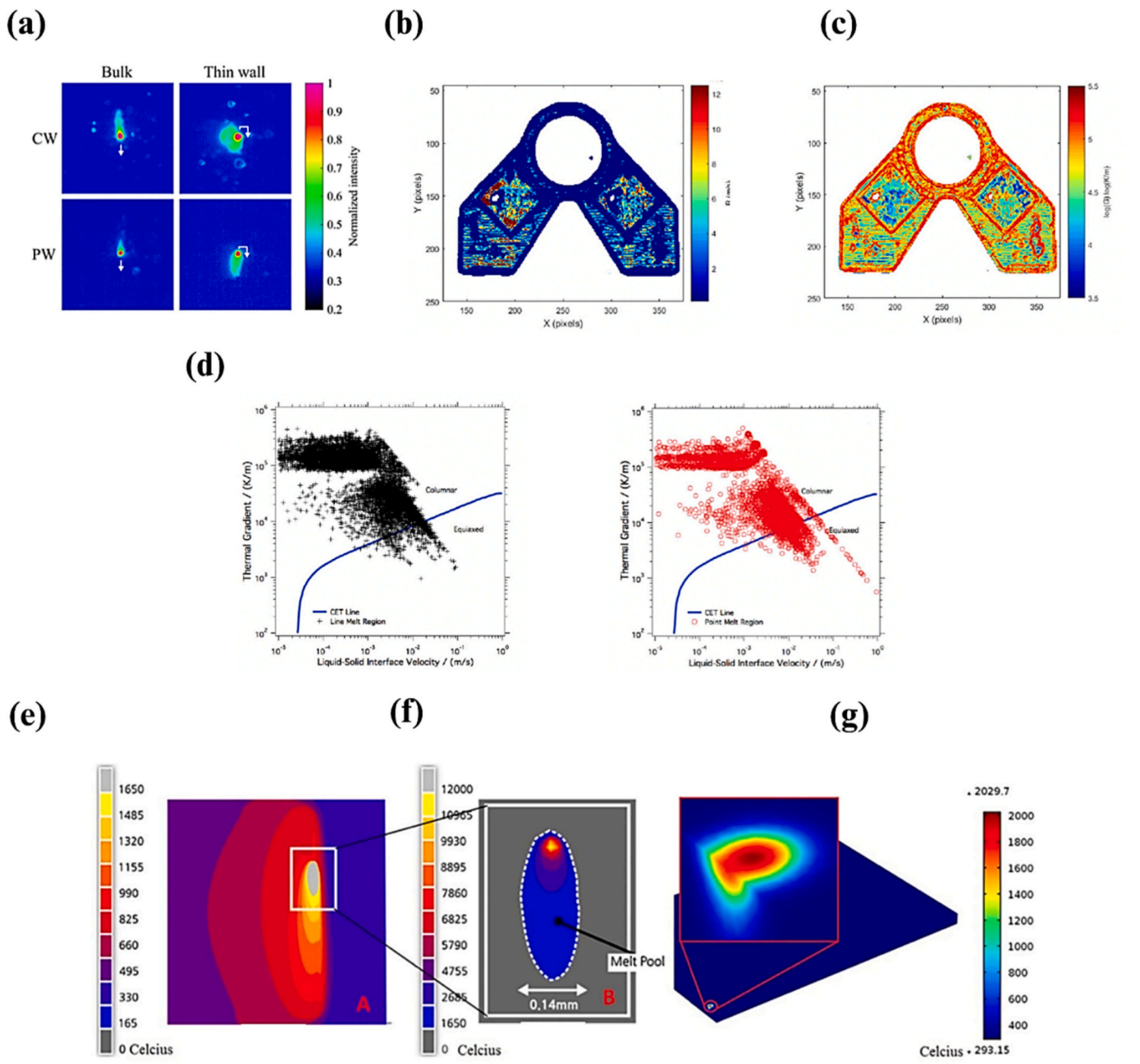



**Fig. 3.** (a) NIR images captured for both bulk and thin wall geometries under various emission modes. White arrows highlight the beam trajectory [70]. The layer Thermal Gradients (b), Interface Velocity (c), and CET curve (d) [71]. Performing precision process of thermal measurement (e, f); Zoomed-in melt pool geometry and temperature distribution (g) [69].

cracks, or incomplete fusing. [65]. Heat monitoring is a typical non-contact sensing technique in advanced manufacturing laser processes like welding, thermal hardening, cladding, and, more recently, L-PBF [66] and EB-PBF [67]. Inhomogeneous mechanical characteristics result from variations in the microstructures and forming dimensions of as-built components caused by local heat fluctuations over time during material processing.

Fig. 3(b) displays the layer thermal gradients using thermography. The interface velocity contour in Fig. 6a shows that regions using the point melt approach have considerably greater velocities than the remainder of the construct. In contrast, the thermal gradient contour in Fig. 3(c) demonstrates that line melt locations have larger thermal gradients than point melt zones. When plotted against a columnar-to-equiaxed transition curve (Fig. 3(d)), the equiaxed region points move closer to the chart's equiaxed area [68]. Another study further supports the role of thermography in precision thermal measurement, with Fig. 3 (e, f) demonstrating real-time melt pool monitoring. This setup enables precise temperature control, which is crucial for maintaining process stability. Fig. 3(g) provides a detailed view of the melt pool geometry and its temperature distribution, offering a high-resolution perspective on temperature variations directly influencing material properties in the final build [69].

Thermographic systems are widely applied to assess process stability and determine melt pool dimensions [72]. In L-PBF, Zheng et al. utilized a coaxially aligned thermal camera with the laser beam to monitor melt pool temperature [73]. Dimer et al. developed a multi-sensor system incorporating NIR and visible wavelength cameras alongside a photo-diode to track porosity formation, analyzing laser absorption rates and

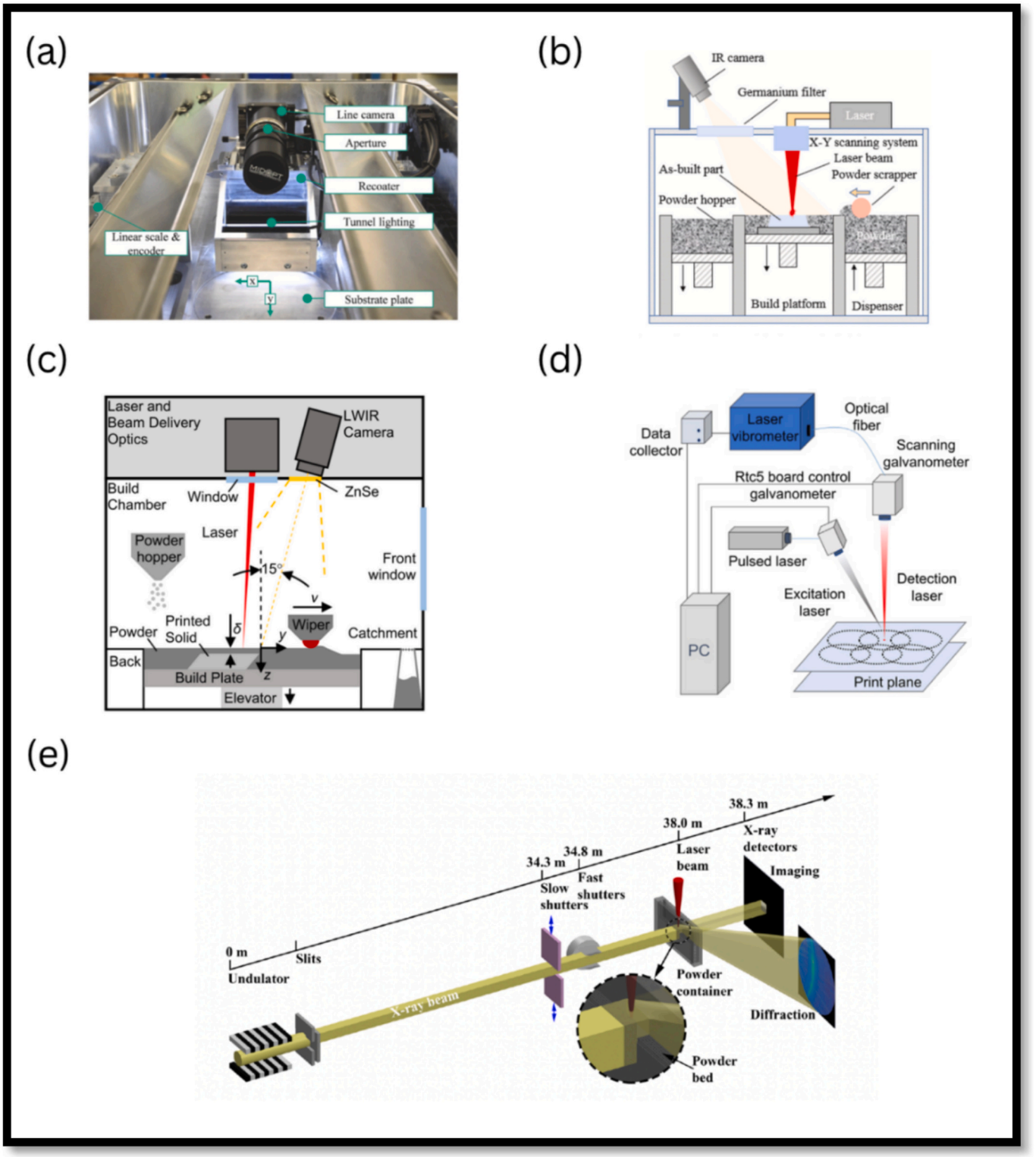



**Fig. 4.** (a) Optical monitoring system integrated into an L-PBF machine [56]. (b) Schematic diagram of the IR monitoring system integrated into the L-PBF experimental setup [64]. (c) Illustration of the L-PBF experimental setup, including the LWIR camera [90]. (d) Multi-circle scanning using a laser ultrasonic system [77]. (e) Schematic of the high-speed X-ray imaging and diffraction setup for L-PBF at the Advanced Photon Source [91].

temperature field dynamics [74]. Mitchell et al. monitored L-PBF anomalies using a two-color pyrometer, providing insights into thermal gradients that significantly impact part microstructure [75].

By measuring the thermal radiation emission from the powder bed under laser irradiation, insight into the thermal gradients present in the PBF process, which significantly influence final part properties such as microstructure, can be gained.

Berumen et al. employed a 10 kHz camera and a photodiode to capture the geometry of the melt pool and the average radiation intensity emitted [71]. Heigel et al. investigated how laser features affect melt pool temperature and form in DED systems, demonstrating significant connections between laser parameters and thermal management

[72]. Arısoy et al. used in-situ IR monitoring of an IN625 process and finite element simulations to improve thermal behavior predictions [73]. Unlike L-PBF techniques, EB-PBF procedures do not allow for the coaxial mounting of lenses with the electron beam. Furthermore, vaporized particles may condense in the vacuum environment on the system's viewing windows and optics. As a result, some changes must be made to enable thermal imaging [67]. Schwerdtfeger et al. presented a suitable solution by placing a ZnSe window at a 15° angle to the e-beam axis within the EB-PBF chamber, successfully adapting IR thermal imaging to EB-PBF settings [76].

Thermographic monitoring offers the advantage of capturing real-time thermal distributions, allowing the detection of subsurface defects, hotspots, and melt pool instabilities that optical systems cannot reveal. Its non-contact nature and high temporal resolution make it suitable for process control in L-PBF. Limitations include sensitivity to emissivity variations, reduced spatial resolution compared with optical imaging, and challenges in vacuum environments. While L-PBF allows straightforward integration of LWIR cameras (Fig. 4(c)), EB-PBF requires adaptations such as angled windows to accommodate thermal imaging under high-temperature vacuum conditions [77].

### 4.3. Acoustic-based monitoring systems

While previous sections discussed the benefits of visual, infrared, and thermal signals for monitoring surface-level characteristics, these methods are restricted in exposing underlying conditions in manufactured components. When the laser interacts with metal materials in the PBF process, transient elastic waves are formed inside the molten pool, revealing important internal details such as pores and cracks [78]. Acoustic sensing in PBF detects generated sonic or ultrasonic waves caused by laser operation or sound waves sent by transducers into the sample. These waves carry essential interior information like pores and cracks [79]. Advancing Acoustic Emission (AE) sensor technologies are critical for recognizing defects in PBF. Contact-type piezoelectric sensors are commonly used to detect AE signals, which include structural-borne, air-borne, and ultrasonic signals.

The two most common acoustic-based sensing in PBF operations are ultrasonic testing (UT) and AE spectroscopy. Ultrasonic testing (UT) is a common NDT technique that tests a part using ultrasonic waves and records time-resolved acoustograms of the reflected or transmitted waves. This enables the detection of subsurface defects. UT is commonly used for fatigue testing during a part's lifespan in industrial contexts such as aerospace [80]. Because of their short wavelength and accuracy, ultrasonic pulses are widely used in NDT, especially for offline quality assurance and real-time monitoring with data correlation across processes. Although producing ultrasonic waves in AM requires more equipment, UT may be scaled up with many transducers to cover more prominent regions [77]. Dai et al. developed an in-situ Laser Ultrasonic (LU) system for sub-millimeter crack detection in L-PBF, identifying crack faults of approximately 0.5 mm depth. Additionally, Lamb wave behavior facilitated the estimation of crack positions and dimensions [81]. Additionally, the behavior of Lamb waves was used to estimate the positions and size of crack defects. Using a Doppler vibrometer, Lv et al. recorded ultrasonic waves produced by a pulsed laser in L-PBF with a high signal-to-noise ratio [82]. Notably, UT holds promise as a metrological tool for AM-produced parts, especially with materials prone to large voids or porosities [83]. Offline metrology may utilize pulser/receivers, phased arrays of ultrasonic transducers, or lasers for ultrasonic wave generation [84]. In an innovative in-situ application, Rieder et al. attached a single ultrasonic transducer under the build plate to transmit waves into the part, recording reflections with a pulse/receive unit, which enabled the detection of simple void geometries during PBF [85].

As ultrasonic waves penetrate porous layers, they undergo scattering and reflection, subsequently recorded and mapped to specific build layers [86]. Defects such as cracking, delamination, and pore formation can be detected by listening to AE during PBF processes. For instance, Ye et al. documented in situ AE monitoring of PBF of 304 stainless steel, employing recorded acoustograms alongside optical micrographs for comprehensive analysis [87]. Smith et al. further explored in-situ part porosity through spatially resolved Acoustic Emission Spectroscopy (AES) during PBF, providing qualitative data on part quality despite the current limitations in precise defect quantification [88].

In addition to electromagnetic waves, mechanical wave-based technologies like Spatially Resolved Acoustic Spectroscopy (SRAS) and LU imaging are effective NDT techniques for in-situ monitoring. SRAS and LU imaging can identify and analyze various defect types, including internal, surface, and subsurface defects. LU imaging, in particular, is frequently used to determine surface geometry and morphology in AM components. This technology combines laser generation and ultrasonic sensing to provide high-resolution photographs of a material's internal structure. The selection of UT methods, such as SRAS or LU imaging, is significantly influenced by the manufacturing process, material characteristics, and the unique capabilities of each UT technique, all of which impact the success of defect identification and material characterization in AM. Surface Acoustic Waves (SAWs) are a fundamental tool in SRAS, a laser ultrasonic method used to evaluate the elastic properties of materials [89].

Acoustic-based monitoring provides unique access to subsurface and internal defects, such as pores, cracks, and delamination, which optical or thermal methods cannot reveal. Techniques like ultrasonic testing and laser ultrasonic imaging (Fig. 4(d)) offer high spatial resolution and depth penetration, enabling precise defect localization [90]. Limitations include complex instrumentation, sensitivity to material heterogeneity, and the need for careful sensor placement. While these methods are effectively integrated into L-PBF, EB-PBF poses additional challenges due to the vacuum environment and high substrate temperatures, requiring specialized transducer arrangements or non-contact laser-based setups for reliable in-situ monitoring.

### 4.4. Tomography-based monitoring

Tomography-based monitoring is being developed as an effective tool for detecting defects in L-PBF processes, and it outperforms standard NDT methods like optical, infrared, thermographic, and acoustic approaches. Optical and infrared monitoring, which identifies surface-level defects, has limitations in the depth resolution needed to detect subsurface or internal defects. Although thermographic techniques may identify some near-surface thermal abnormalities, they are often restricted in detecting deeper structural characteristics. While acoustic monitoring methods help detect cracks or voids, they frequently need direct material contact, which might interfere with the L-PBF process.

Tomography, particularly X-ray computed tomography, addresses these challenges by acquiring high-resolution, volumetric pictures of the structure, allowing for the diagnosis of surface and interior defects with remarkable precision. Researchers and manufacturers may better understand L-PBF defect formation mechanisms by employing tomographic imaging to view layer-by-layer material deposition and discover defects such as pores, inclusions, and cracks in real-time. This enables us to provide quality assurance and adaptive process control, considerably improving part dependability in high-performance applications.

A 3D model can be reconstructed from many 2D cross-sectional photos obtained throughout the manufacturing process to generate tomographic data for AM parts. PBF's underlying layer-by-layer approach is ideally suited to tomographic techniques, allowing for component analysis using optical or other imaging modalities at each construction stage. Optical tomography, particularly at visible wavelengths, has successfully detected LoF defects during the melting process [92]. Despite scan quality fluctuations, μ-CT is a commonly used post-fabrication metrology technology that provides non-destructive insights into the interior structure of AM components [93].

Townsend et al. developed a method for producing areal data from volumetric XCT scans of PBF parts to build intricate interior features,

internal surface inspection, and quality evaluation [94]. μ-CT/XCT captures high-resolution X-ray images while the sample spins and reconstructs them into a 3D model. This allows a detailed internal investigation without physical sectioning. This method is useful for detecting interior problems, such as pores, cracks, and LoF defects, that are not evident from the surface. Additionally, its high-resolution capacity guarantees visualization of micron-scale features, which is crucial for PBF components.

Furthermore, μ-CT/XCT enables in-situ sensing throughout the PBF process, detecting real-time defects like porosity, balling, and LoF [95]. Another tomographic technique suitable for in-situ monitoring is optical coherence tomography (OCT), based on Coherence Scanning Interferometry (CSI). Neef et al. demonstrated OCT in a PBF process, which allowed them to examine each layer's formed component surface, melt pool, and powder bed [96]. Compared to other approaches, OCT is more suitable for sub-micrometer resolution, improving fault identification and assessment accuracy despite significant uncertainty in topographical details [97].

Tomography provides unparalleled insight into internal and surface defects, offering high-resolution, volumetric imaging that surpasses optical, infrared, thermographic, and acoustic methods. Its advantages include non-contact, subsurface defect detection and the ability to reconstruct 3D models for layer-by-layer analysis. Limitations include high equipment cost, slower acquisition times, and complexity in integrating in-situ setups. While tomography is effectively applied in L-PBF (Fig. 4(e)), EB-PBF monitoring is more challenging due to vacuum conditions and high temperatures, often requiring specialized X-ray or optical arrangements to ensure reliable defect detection [91].

### 4.5. X-ray in-situ melt pool monitoring

X-ray in-situ monitoring has emerged as a critical approach for observing melt pool dynamics and defect formation in PBF processes, including porosity, solidification cracks, and other microstructural anomalies. Unlike post-mortem inspection, in-situ X-ray imaging allows real-time visualization of solidification phenomena at multiple length and time scales, providing detailed insights into the process–structure–property relationships essential for high-performance metallic components. As highlighted by Karagadde et al., in-situ and operando X-ray imaging can capture nucleation, dendrite growth, phase transformations, and the evolution of defects during solidification [98]. Laboratory-based X-ray sources enable high-resolution imaging of microstructural features, while synchrotron-based techniques offer fast imaging of transient melt pool phenomena with sub-micrometer resolution. These observations are invaluable for validating predictive models and improving the understanding of defect formation mechanisms in AM.

In parallel, 3D surface topography monitoring complements X-ray techniques by providing practical, layer-wise insights into the AM process [99]. Methods such as fringe projection, laser scanning, and multi-view imaging allow detection of surface irregularities, powder layer inconsistencies, and early indications of defects that may lead to porosity or fusion problems. Although surface monitoring primarily captures external features, its integration with X-ray imaging and other sensing modalities can provide a more comprehensive defect detection strategy. Together, X-ray in-situ monitoring and advanced 3D surface techniques enhance our ability to understand, predict, and control defects, supporting the development of mechanism-aware, high-quality AM processes.

Table 1 summarizes the key in-situ and ex-situ monitoring techniques discussed in this section. The table contrasts optical, infrared/thermal, thermographic, acoustic, tomographic, and X-ray-based approaches in terms of spatial resolution, relative cost, detectable defect types, key advantages, and inherent limitations for PBF processes.

## 5. Mechanistic, numerical, and simulation approaches

Computational modeling plays a pivotal role in advancing defect detection and process understanding in AM, providing accurate predictions and reducing experimental effort in certification procedures. Metal component production via AM involves complex transitions from microscale particle interactions to macroscale part fabrication, spanning multiple spatial and temporal scales—from microseconds during powder melting to hours or days for full components. To address this complexity, researchers have developed a wide range of mechanistic, numerical, and simulation approaches, each tailored to capture critical physical phenomena at specific scales [100].

These methods are commonly categorized into micro-, meso-, and macroscale models, each offering unique insights into AM process dynamics [101]. Microscale models focus on melt pool behavior, layer formation, temperature fluctuations, and microstructure evolution. Macroscale models capture residual stresses, part distortion, and overall thermal cycles, enabling prediction of component-scale effects. Mesoscale models bridge these extremes, connecting local phenomena to global outcomes. By systematically reviewing these approaches, this section highlights the state-of-the-art computational strategies that underpin defect detection, process optimization, and quality control in PBF AM.

At the macroscale, models are focused on estimating residual stresses and distortions generated by heat loads during the process. Unlike microscale models, macroscale techniques primarily concern heat cycles, allowing for more straightforward physics with coarser

**Table 1**
Comparison of sensing modalities for defect detection in metal PBF processes.

| Technique | Typical spatial resolution | Relative cost | Detectable defects | Key advantages | Main limitations |
|---|---|---|---|---|---|
| Optical (Visible cameras) | High (≈5–25 μm/pixel) | Low–Medium | Surface defects, recoater streaks, balling, layer shifts, surface cracks | Low cost, high spatial resolution, easy integration, effective for layer-wise monitoring | Surface-only, sensitive to spatter/lighting, limited in EB-PBF |
| Infrared/Thermal | Moderate (≈50–100 μm/pixel) | High | Lack-of-fusion, overheating, keyhole instability (indirect), thermal anomalies | Captures subsurface thermal signatures, robust under bright laser emission | Emissivity-dependent, lower spatial resolution, challenging in EB-PBF |
| Thermography/Pyrometry | Moderate–High (process dependent) | Medium–High | Melt pool instability, hot spots, thermal gradients linked to pores/cracks | High temporal resolution, suitable for process control | Requires calibration, sensitive to emissivity and optics fouling |
| Acoustic (AE/UT/LU) | Moderate (sub-mm) | Low–Medium | Internal pores, cracks, delamination, spatter events | Subsurface sensitivity, non-optical, suitable for internal defect detection | Complex signal interpretation, noise sensitivity, localization challenges |
| Tomography (XCT/OCT) | Very high (≈1–10 μm) | Very High | Internal porosity, LoF, cracks, inclusions, 3D defect morphology | Full volumetric insight, high accuracy, non-destructive | High cost, slow acquisition, limited in-situ applicability |
| In-situ X-ray (Synchrotron) | Very high (μm-scale) | Extremely High | Keyhole pores, gas bubbles, solidification cracks, melt pool dynamics | Direct observation of defect formation mechanisms | Limited to research facilities, small FOV, not industrially deployable |

discretization suited for modeling complete industrial components [102,103]. Fig. 5(a) shows temperature field modeling at the laser scan track cross-section, demonstrating how these computational methods handle thermal gradients crucial to part integrity.

### 5.1. Heat input modeling

Heat input modeling is critical in powder-based AM techniques, where high-density energy beams melt the powder. Like those used in fusion welding, established heat source models from welding simulations can work well with sophisticated AM processes. Goldak and Akhlaghi studied various heat source models in welding situations, providing valuable insights for AM applications [104]. This procedure includes predicting the distribution and absorption of heat, which is critical since uneven heat input can result in defects like bending, porosity, and microcracks in the final product. Researchers use mathematical representations of heat flow to describe heat input accurately, such as surface and volumetric Gaussian models, which reflect how the laser's energy penetrates and disperses throughout the material.

Accurate heat input models provide more control over the size and temperature of the melt pool, allowing for defect reduction by changing factors like laser power and speed to optimize material melting and solidification. These models, which analyze heat dispersion in L-PBF, are essential in improving component quality and dependability in advanced manufacturing applications. In laser-based AM, numerous heat flux models are used to satisfy the requirements of different laser types and applications. Fu et al. provide an overview of standard laser heat flux models, such as surface, volumetric, and conical flux types. Fig. 5(b) demonstrates a laser cut prediction for clarity [105].

The literature further explores alternative heat flux models, including volumetric Gaussian flux (Fig. 5(c)) [107,109], parabolic heat distribution [110], and other laser-based geometries tailored to AM specifications [111]. In EB-PBF, volumetric heat flux models, particularly those with Gaussian distributions, are preferred due to the beam's capacity for deeper material penetration.

Recent work has introduced more sophisticated heat source models that account for laser–powder interactions and beam characteristics. For example, volumetric heat sources based on Monte Carlo ray-tracing and electromagnetic wave absorption have been developed to capture how a laser's energy is absorbed through the depth of the powder bed [112].

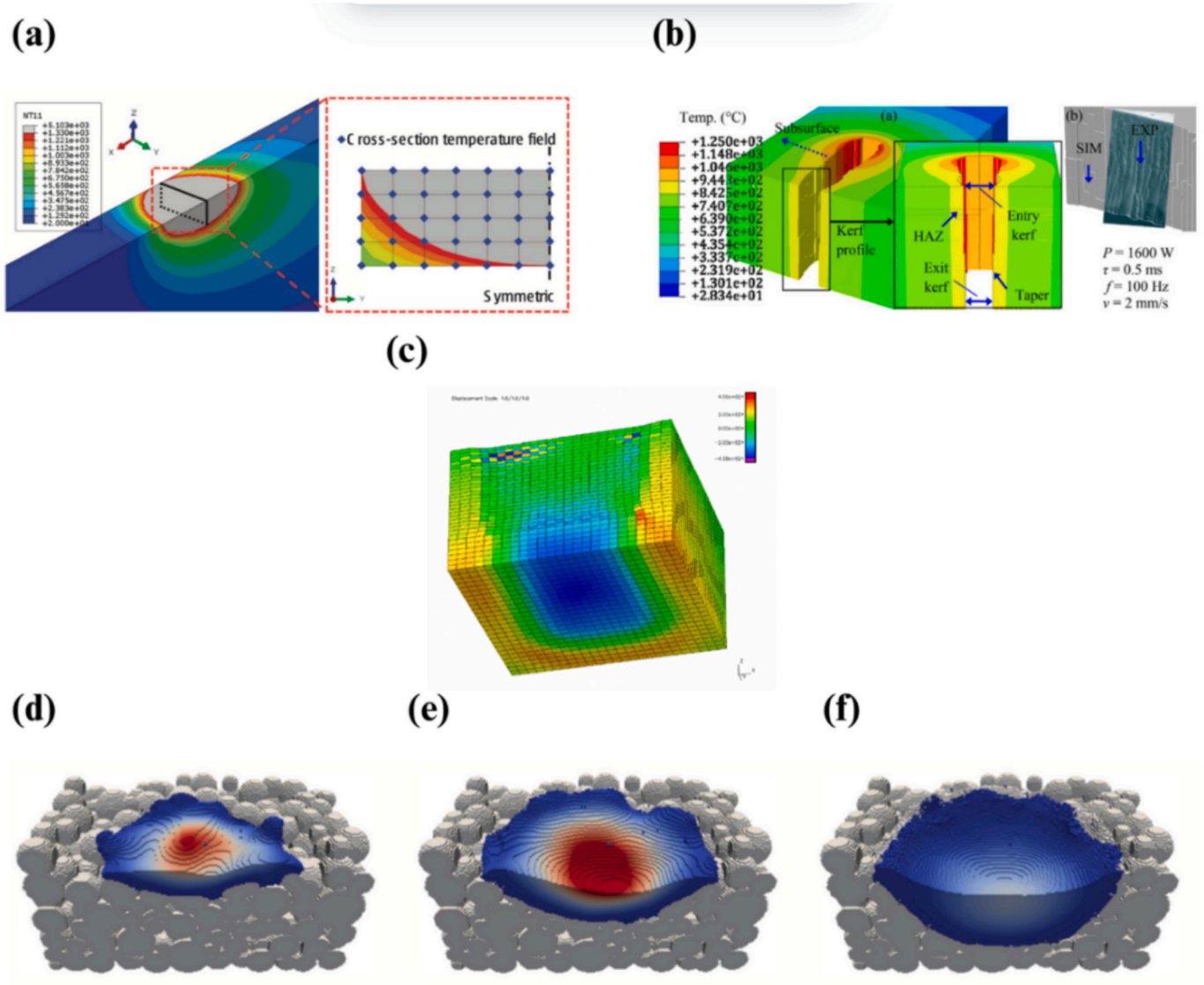



**Fig. 5.** (a) Temperature field in the cross-section of laser scanning track [106], (b) Representative prediction of laser cut kerf and comparison between predicted and measured striated surfaces [105], (c) Cube example after 12 layers deposited, Tzz stress [MPA] [107], (d) Snapshots of spot melting in a powder bed at different time steps; the beam pulse duration in 2500-time steps, (e) 5000-time steps (f) 10,000-time steps [108].

Such models show that powder layer thickness and multiple reflections significantly affect the vertical energy distribution, deviating from a simple exponential decay. Monte Carlo approaches have even been extended to EB-PBF, revealing phenomena like particle eruptions under electron irradiation [113]. Moreover, beyond the standard Gaussian or Goldak's double-ellipsoid heat source, new parameterized shapes (e.g., conical and depth-decaying profiles) and hybrid heat source models spanning conduction and keyhole regimes have been proposed to better represent shallow vs. deep melt pools [114]. To use these advanced models effectively, calibration across different process settings is essential.

Physics-informed ML techniques are emerging to calibrate heat source parameters over wide process windows without repeated experiments. For instance, Bayesian optimization and regression have been employed to tune volumetric heat flux profiles (effective absorptivity, shape dimensions, etc.) so that a single heat source model remains valid for various laser powers and scan speeds [114,115]. This approach eliminates the need to re-fit the heat source for each condition, significantly broadening the predictive capability of thermal FE simulations. Notably, effective laser absorptivity in a powder bed is higher than on a flat plate due to multiple scattering and the laser trapping in vapor depressions; models calibrated with in situ measurements confirm absorptivity can nearly double (e.g., from ~0.35 to 0.7 for stainless steel) when transitioning from conduction to keyhole mode [115]. By incorporating such physical insight, modern heat input models improve the accuracy of temperature field predictions and lay a more reliable foundation for downstream melt pool and stress analyses.

From a defect detection perspective, heat input models provide critical thresholds for identifying conditions that promote lack-of-fusion porosity, keyhole instability, or excessive evaporation. By correlating simulated energy density distributions with experimentally observed defects, these models establish process windows that support both physics-based defect prediction and the interpretation of in-situ thermal and emission signals.

### 5.2. Temperature gradient modeling

Temperature changes during AM fabrication are critical, affecting melt pool formation, microstructure development, stress distribution, and part distortion. Although directly detecting immediate temperature offers difficulties, thermal modeling has been widely researched. Zeng et al. shared an in-depth review of thermal modeling techniques [116], encompassing FE-based [117], finite volume (FV)-based [118], and Lattice Boltzmann method (LBM) approaches [108,119].

Zeng et al., in particular, rigorously validated their LBM technique for rigorously simulating the EB-PBF process in AM. The validation process comprised developing two electron beam absorption algorithms—constant and exponential—based on electron beam properties such as acceleration voltage and energy dissipation, which ensured accurate penetration and absorption dynamics predictions across beam intensities [108]. These algorithms were carefully evaluated against analytical solutions to ensure the model's reliability.

Further validation entailed modeling interactions inside a powder bed, emphasizing critical characteristics such as melt pool formation, energy distribution, and beam-material interactions. The model's melt pool size, form, and duration predictions were then compared to empirical results, which closely matched the experimental data and validated the computational outputs against observed behaviors. Fig. 5 (d, e, and f) depicts Zeng et al.'s research on spot melting in PBF during simulation. To maintain integrity and precision, any robust prediction model must have a trustworthy heat flux model, correct material parameters, and thorough heat transfer dynamics. Temperature gradient models provide the foundation for understanding thermal distributions, which underpin melt pool dynamics; thus, melt pool simulations can be considered a detailed, localized case of temperature field modeling incorporating fluid flow, surface tension, and Marangoni effects.

Temperature gradient models play a key role in supporting defect detection by providing reference thermal fields against which in-situ infrared, thermographic, and pyrometric measurements can be interpreted. These models help distinguish true process-induced anomalies from measurement artifacts related to emissivity variations or limited sensor resolution, thereby supporting sensor calibration and improving confidence in temperature-based defect indicators.

### 5.3. Surface roughness modeling

The surface quality of PBF-fabricated parts is another aspect receiving attention in modeling. The as-built surface is often irregular due to partially fused particles and track instabilities, which can reduce fatigue performance. While a part's global geometry is set by the CAD model, the microscale surface topography is a by-product of melt pool fluid behavior and ejected material. High-fidelity melt pool simulations have recently been used to predict surface morphology. By tracking the free surface of the molten metal and its solidification, these models can reproduce the waviness of scan tracks and the formation of surface beads or ripples. For example, simulations in FLOW-3D showed that a combination of capillary action and gravity leads to a slightly convex bead profile, and the predicted melt track height and width matched well with experimental cross-sections [120].

Such predictions are valuable for estimating surface roughness without costly builds. Another contributor to surface roughness is spatter, droplets of ejected melt that land and fuse onto the top surface. Comprehensive CFD models that include recoil pressure-driven melt ejection can capture the size and trajectory of spatter particles [121]. By coupling these models with Lagrangian particle tracking or discrete droplets, researchers have started to simulate spatter deposition on the powder bed and resulting surface defects. For instance, numerical studies have shown that high laser power keyhole regimes produce larger melt ejections, which, upon redeposition, create protrusions on the layer surface [122].

These insights align with experimental observations of increased surface roughness at higher energy densities despite better melting, due to the presence of re-solidified droplets. Finally, some models link process parameters to an expected roughness value ($R_a$ or $S_a$) by simulating a few layers and statistically characterizing the top surface profile. This provides a virtual metrology tool to optimize parameters for smoother surfaces. As computing capabilities grow, it is foreseeable that multiphysics PBF simulations will concurrently predict not only internal properties (microstructure, porosity, residual stress) but also external surface finish, providing a comprehensive understanding of part quality. Each of the modeling approaches discussed – thermal, fluid, mechanical, microstructural, and surface – forms a piece of the overall PBF simulation puzzle. The ongoing integration of these models, aided by reduced-order techniques and data-driven enhancements, is steadily pushing us toward a true “digital twin” of the PBF process, wherein all key phenomena can be simulated and controlled [123].

Surface roughness is a critical factor in determining the texture of AM components, having a significant effect on fatigue performance. Todhunter et al. investigated major surface texture characteristics often employed in industry, focusing on the functions of $R_a$ (arithmetic average roughness) and Sa (arithmetical mean height). The $R_a$ parameter, which determines the arithmetic mean of height deviations from a central baseline over a given surface length, is especially useful for characterizing roughness. In contrast, $S_a$, an areal roughness measure, provides improved dimensional insights by considering the texture over a specific region [124]. Accurate modeling of surface roughness, which considers characteristics like $R_a$ and $S_a$, requires addressing complicated multiphysics interactions. Wei shares an extensive examination of surface phenomena and underlying mechanisms that influence surface roughness in the context of welding, giving insight into parallel aspects pertinent to AM processes [125]. Surface roughness models further support defect detection by explaining variations in optical reflectivity

and infrared emissivity, which directly influence the interpretation of in-situ imaging and thermal monitoring signals used for surface defect identification.

### 5.4. Melt pool modeling

Melt pool modeling represents a localized and detailed application of temperature field simulations, focusing on the molten region where thermal gradients, fluid flow, surface tension, and Marangoni effects interact. Understanding melt pool dynamics is critical for predicting microstructural evolution, defect formation, and overall part quality in AM. In this section, we review computational approaches and experimental validations that capture melt pool geometry, thermal-fluid behavior, and solidification phenomena.

Creating melt pools in AM procedures plays a fundamental role in shaping the microstructural integrity of produced components. Melt pool geometry is influenced by process parameters like hatch spacing and layer thickness, which also help identify microscale defects such as LoF between neighboring scans or layers. Understanding thermal fluid dynamics inside the melt pool provides insights into microstructural properties such as grain shape, microcracks, partly melted powders, and porosity. Helmer et al. discovered correlations between melt pool geometries and grain morphology under specified processing settings, revealing the impact of thermal dynamics on the final microstructure. Fig. 6 depicts pole figures in 2D from simulation studies, which capture the effect of energy factors on grain formation [126].

Studies by King et al. [127] and Markl and Körner [128] provide a comprehensive overview of powder-level simulation techniques, including methods like the LBM, discrete particles method, FV method [129], and computational fluid dynamics (CFD) method [130]. Conversely, continuum models represent powders as low-thermal-conductivity solid continua to reduce computational complexity. Notable examples of continuum modeling include FE method simulations conducted by researchers for L-PBF and EB-PBF processes [131–133].

Based on the literature, Repossini et al. investigated maraging steel melt pool behavior using high-speed off-axis in-situ imaging [134]. The melt pool dynamic is mainly governed by capillary and Marangoni forces, evaporation pressure, and powder particle wetting ability, as observed by Scharowsky et al. [135]. The melt pool shape and size were calculated using heat conduction models [136], which do not account for the effect of melt metal convection, which is frequently the primary mechanism of heat transfer within the melt pool [7]. Their work illustrated how the LoF defects during PBF can be minimized by using heat transfer and fluid flow calculations LoF in the L-PBF, and it presents a methodology to predict and prevent these defects based on a numerical heat transfer and fluid flow model for the L-PBF. These defects can be avoided by adjusting laser power, scanning speed, layer thickness, and hatch spacing.

Lee and Zhang pioneered the development of an FV model to analyze both the geometry of melt pools and the morphology of grains within a dual-track L-PBF process [137]. Their model incorporated multiple reflections to enhance the simulation of laser-material interaction. The relatively little heat input kept the melt pool regime in a steady, shallow-depth state, notwithstanding these advances.

Qiu et al. used an FV model to investigate the impact of laser scanning speed on porosity levels in further detail [138]. Similarly, they continued concentrating on high laser speeds, producing shallow melt pools. Leitz et al. used an FE model to investigate the effects of different powder properties on melt pool geometry [139]. Simultaneously, Matthews et al. investigated the denudation of powder under various process conditions using a FEM-based model [140]. In a fundamental inquiry, Wu et al. scrutinized the effect of evaporation on melt pool profiles within a single-track L-PBF process [141]. Moving further, Bayat et al. modeled the evolution of lack-of-fusion voids across a multi-track, multi-layer L-PBF process [142].

Shen and Chou's work on electron beam and thermal modeling for Ti6Al4V, and then they go for comparison with numerical results, which were obtained by Wang et al. [143]. Their finite element model correctly anticipated the melt pool size for the 316L stainless steel LENS process.

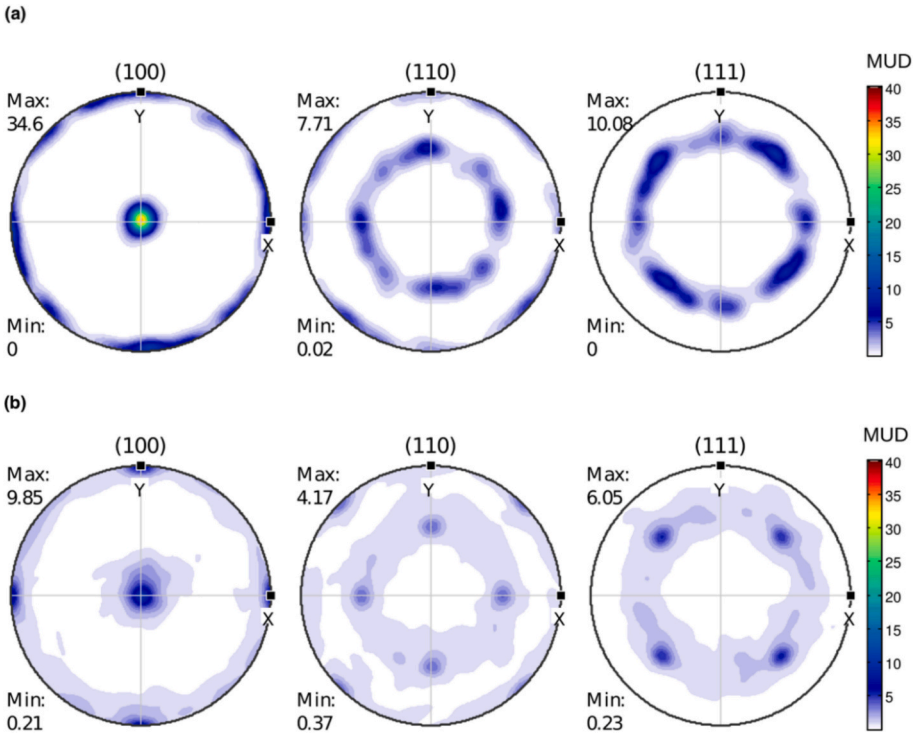



**Fig. 6.** Representative pole figures in the XY-plane: (a) Columnar grains. Parameters: EA = 1.8 J $mm^{-2}$, v = 2.2 $ms^{-1}$, Loff = 150 μm, (b) Equiaxed grains. Parameters: EA = 1.9J$mm^{-2}$, v = 8.8 $ms^{-1}$, Loff 1/437.5 mm [126].

Shen and Chou [144] went deeper into numerical analysis, investigating the impact of porosity and beam diameter on melt pool size in EB-PBF. They found that increasing porosity, which indicates higher powder density, resulted in higher temperatures, deeper melt depths, and shorter melt pool lengths.

Expanding upon the thermal model introduced by Shen and Chou [144], subsequent research enhanced mechanical properties to simulate residual stresses in the EB-PBF process of Ti6Al4V [145]. This advancement incorporated temperature-dependent Young's modulus, thermal coefficient, and yield stress. Introducing cooling phases and employing the element activation technique enabled the simulation of layer-by-layer manufacturing. To distinguish between variations in melt pool dynamics, another research used computational thermal-fluid dynamics simulations in conjunction with single-bead melting experiments in EB-PBF and L-PBF [146]. The highest temperatures in L-PBF molten pools were substantially lower than those in their EB-PBF equivalents. Variations in preheating temperature also affected the vapor recoil pressure; on the melt surface, the effect was exacerbated by ambient pressure and numerous laser reflections in L-PBF.

In contrast to FE and its subset discrete element method (DEM), to simulate powder-based AM processes, other methods, like Molecular Dynamics (MD) modeling, can handle rotational degrees of freedom, non-spherical particles, and polydisperse particle systems. While there are some similarities between DEM and MD, there are also significant differences, with DEM providing a wider variety of particle system properties [147]. Another popular particle-like technique is Smoothed Particle Hydrodynamics (SPH) [148]. Fluid and solid mechanics may be simulated using SPH since particles in the model have a spatial smoothing length across which a kernel function interpolates their characteristics [149]. Also, to integrate all of them, multiphysics modeling and simulation in this context can be proposed, like this article, to incorporate all aspects of different approaches in all scales [150].

Melt pool modeling represents one of the most direct numerical links to defect detection in PBF processes. Simulated melt pool geometry, stability, and lifetime are strongly correlated with defect mechanisms such as lack-of-fusion porosity, keyhole-induced voids, balling, and spatter formation. By establishing quantitative relationships between process parameters, melt pool dynamics, and defect occurrence, these models enable the prediction of defect-prone regimes and provide a physical basis for interpreting in-situ optical, thermal, and acoustic signatures associated with melt pool instabilities.

### 5.5. Micro structure modeling

Heat input, temperature gradients, surface roughness, and melt pool characteristics are all essential parts of microscale process modeling, given that they provide vital insights into the following microstructures. Specific microscale models go further into the evolution of microstructural characteristics, concentrating on elements such as fractional phase, solidification phase, and porosity. Basak et al. investigated the highly sensitive microstructural properties of metal AM. They identified significant factors influencing component quality, such as porosity, unmelted particles, grain anisotropy, balling effects, microcracks, and material inhomogeneity. Porosity remains an essential concern because it directly impacts AM-fabricated components' mechanical characteristics and overall performance [151].

The field of porosity modeling is still largely unexplored despite its importance. Phase field (PF) approaches are most commonly used by researchers worldwide to handle solidification processes [152,153]. These approaches typically use FV or FE techniques with cellular automata (CA) models [154]. Boettinger et al. provide a thorough description of these methods [153]. Tang et al. developed a geometry-based model to predict porosity from LoF in powder bed AM processes, which was enhanced by analytically determined melt pool dimensions. This model explains porosity in terms of hatch rotation, hatch spacing, layer thickness, and melt pool dimensions. The geometry of the melt pool is determined via computational modeling or experimental measurement. In addition to the absence of fusion, many other parameters significantly impact porosity [155].

Barsoum employed a two-dimensional model to simulate a multi-pass welded tabular joint structure afflicted by LoF, unveiling the profound impact of LoF size on the structure's fatigue life [156]. Modeling fusion is correlated with the weld or melt pool profile in material processing. Wu et al. proposed a free surface profile model by minimizing the total [157]. Numerous researchers have directed efforts toward capturing the beam profile and beam overlap to establish a more physics-based model for investigating fusion or penetration conditions, modeling the weld bead cross-section as a half-circle [158], parabola [159], or sine/cosine function [160], with the actual shape contingent upon the energy input rate and processing speed. In light of this understanding, the PF method—which has shown effectiveness in simulating several microstructure evolution issues, including dendritic solidification and grain growth—becomes a suitable means of modeling the metal AM process.

Several attempts have been made to apply PF simulations to AM processes. Gong et al. and Sahoo et al. created a PF model to simulate the consolidation process of Fe powder [161,162], and Krivilyov et al. simulated the dendritic growth of Ti-6Al-4V alloy in an electron beam-induced melt pool [163]. Fig. 7 provides a representation of dendritic structure growth during simulation.

Early models of KH synthesis typically assumed a static equilibrium condition, assuming an energy-pressure balance within the KH generation process [164]. Recent models incorporate Fresnel absorption and reflection effects along KH walls, increasing the accuracy of simulated KH profiles [165]. Lankalapalli et al., for example, developed a two-dimensional heat conduction model based on the conical KH form, allowing for precise penetration depth estimates [166]. Ki et al. created a KH vapor/liquid interface development model using the level-set technique, which is a more computationally efficient alternative to the volume-of-fluid (VOF) method [167].

In laser welding, the change from conduction to KH mode occurs when laser radiation exceeds certain threshold parameters. King et al. studied the parameters required for KH formation, experimentally testing their models with 316L stainless steel and applying known welding models to L-PBF procedures. [168]. Watari et al. developed a metal powder-bed fusion simulation based on a two-fluid model as part of the TRAFAM project, which efficiently addresses KH-induced porosity, plume, and spatter formation caused by interfacial pressure variations between gas and liquid phases [169].

Kruth et al. [170] emphasized the balling phenomena commonly linked with porous materials in PBF processes. While Teng et al. explored numerous modeling techniques for balling effects and KH phenomena, a significant gap exists in models that link these processes to porosity development. This divergence hinders efforts to identify unmelted particles or voids during PBF processes, emphasizing the importance of more complete models incorporating balling and KH effects to forecast and minimize porosity within PBF approaches [171].

Recent advances in numerical modeling utilizing the finite element (FE) approach, which includes characteristics such as powder packing density and size distribution, have improved the accuracy of forecasting defects such as porosity [172,173]. Tan et al. [185] made significant advances by creating a numerical model to investigate porosity growth across different energy regimes in single-track scans. They verified their model by comparing computational findings to accurate data, emphasizing melt pool features and porosities in low- and high-energy density scenarios. To do this, this study simulated the melting and solidification processes of SS316L powders, using the discrete element method (DEM) and CFD approaches to examine porosity creation during L-PBF operations. Three different process parameter sets were chosen to model various energy densities, and the resulting melt pool dimensions were compared to experimental data. The model validation showed great

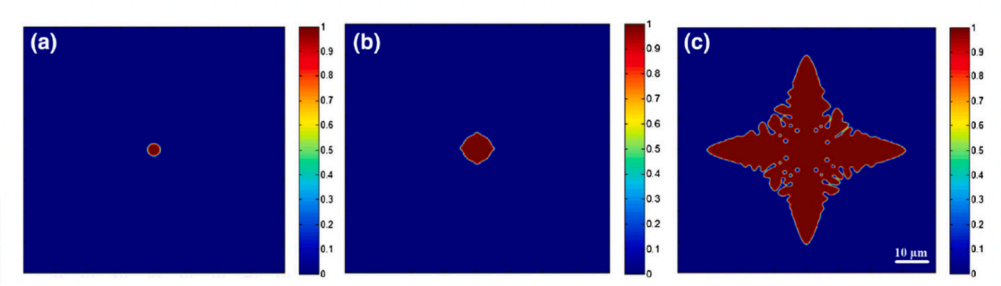



**Fig. 7.** Simulated dendrite structure growth at different times: (a) 0.01 ms, (b) 0.2 ms, and (c) 1.6 ms [161].

accuracy, as the generated melt pool width and depth closely matched experimental observations, with an error margin of up to 7.9%. This level of accuracy demonstrated the model's capability to show essential thermal and fluid dynamics in laser L-PBF correctly. Additional validation was gained by comparing pore characteristics to the model, which effectively predicted the shape and placement of porosities under both low- and high-energy density situations.

Further, for micro-sized parts fabricated using EP-BF, fatigue lifetime investigations used a combined machine learning (ML) and FE modeling approach, providing insights into how random porosity distributions and high surface roughness impact fatigue performance [174,175]. While the random distribution of porosity poses challenges in experimental analysis due to micro dimensions, numerical techniques like FE analysis offer insights into porosity effects. For instance, Wan et al. proposed a multi-scale damage mechanics model to predict the fatigue lifetime of L-PBF Ti6Al4V, exploring the impacts of building orientation and gas porosity [176].

Qi et al. used a simplified model of scanning techniques and component orientations to analyze defects like porosity or delamination preliminarily. Their methodology comprised counting the components still at the melting point and classifying them as faults. They also developed rotating scanning modes and splitting to improve component quality [177]. Moreover, overhang geometries and reasons for overhang warping were examined using activation techniques in thermo-mechanical modeling for Ti6Al4V during the EB-PBF process, considering the impact of powder porosity [178]. These analyses revealed that residual stress decreased as powder porosity decreased, with slower heat dissipation contributing to higher residual stresses [179].

Building upon the PF and CA approaches described above, coupled Cellular Automata–Finite Element (CAFE) frameworks use local thermal histories from macroscopic simulations to predict grain nucleation and growth within each layer. These methods have successfully reproduced columnar prior-β grain structures and epitaxial growth in LPBF Ti-6Al-4V, consistent with EBSD observations [180].

In more detailed formulations PF simulations are employed to capture dendritic solidification microstructure under LPBF conditions. A recent study by Pourmand et al. demonstrates a multiscale PF framework. A finite-volume CFD model provides the solidification parameters (temperature gradient G and solidification velocity V) to a microscopic phase-field simulation, enabling prediction of cellular/dendritic structures in a Fe—Cr alloy [181]. The PF model was able to simulate the transition from planar to cellular solidification and predict primary dendrite arm spacings in close agreement with analytical solidification models and experimental measurements. Importantly, it captured how higher laser energy (in conduction mode) led to larger cell spacing and more well-developed cellular microstructures, which correlates with increased melt pool stability.

Parallel efforts using multi-phase-field models report similar success in predicting features like primary and secondary dendrite arm spacings, melt pool edge grain morphologies, and columnar-to-equiaxed transition under different cooling conditions [130]. In addition to phase-field, fast Cellular Automaton models (often 3D and highly parallelized) are gaining traction for larger domains. They can approximate grain structure in whole parts by assigning state update rules governed by local thermal conditions. Recent works have combined 3D CA with efficient heat flow calculations to simulate grain structures in entire thin-walled components, capturing texture evolution across thousands of layers within reasonable computation [182,183].

There is also a move to integrate microstructure modeling with ML. for example, using neural networks to emulate the outcome of phase-field simulations under various cooling rates, or to invert the process–structure relationship (predicting needed process settings for a target microstructure) [184]. While still emerging, such hybrid data-driven approaches could dramatically speed up microstructure prediction for process optimization. Finally, it's worth noting that EB-PBF can involve different microstructure outcomes (e.g., larger prior-β grain size due to slower cooling and elevated base-plate temperature). Modeling approaches similar to LPBF have been applied to EB-PBF. Yan et al. developed a process–structure–property simulation framework for Ti-6Al-4V in EB-PBF, which integrated thermal modeling, grain growth modeling, and property prediction into an end-to-end tool [123]. Such integrated models can predict final build yield strength and fatigue life based on the simulated microstructure, highlighting the ultimate goal of microstructure modeling, to feed into performance predictions.

Microstructure models further strengthen defect detection frameworks by linking thermal history and solidification conditions to porosity morphology, grain anisotropy, and microcrack formation. These predictions support post-process defect quantification and enable indirect defect inference from microstructure-sensitive signals such as thermal gradients and acoustic emissions.

### 5.6. *Residual stress modeling*

Addressing residual stress in macroscale modeling is crucial for metallic components manufactured using AM methods. The inherent non-uniformity in heat distribution and fast temperature variations during manufacture provides significant tensile residual stress within the component. This process causes part deformation and the creation of microcracks. The consequences are a pair of ways that affected the geometrical correctness of the component and degraded the functional performance of the finished product. Pioneering efforts by Zaeh's team resulted in the development of the “equal layer” method [185], facilitating the simulation of residual stress and distortion in a steel cantilever beam fabricated via L-PBF. Meanwhile, Stucker's group introduced an FE solver leveraging numerical eigenmodes to accelerate AM process simulations [186].

In parallel, Michaleris's team [187], along with Mercelis & Kruth [46], formulated a simplified mathematical model to probe residual stresses. This model predicted the general properties of residual stresses while operating under several assumptions, such as uniform stress distribution inside each layer and production at room temperature. Using a 2D FE approach, Matsumoto et al. examined the top view of powder melting and its effects on residual stress production in their early studies of residual stresses during L-PBF [188].

One major challenge is the disconnect in scale between melt pool physics and part-scale stresses – fine-scale features like melt pool geometry and scan strategy affect local stress, but simulating an entire part with full melt pool resolution is impractical [123]. Recent efforts have introduced multiscale frameworks to alleviate this mismatch. For instance, "minimal element" models simulate a small region (a few layers) with detailed physics to extract thermal strain increments, which are then applied to a larger part model. A notable approach along these lines is the Inherent Strain Method, originally from welding, adapted for layer-by-layer AM. In the inherent strain approach, one first computes the inelastic strain accumulated in a representative volume (via a detailed thermal-mechanical simulation of a few scan layers or tracks), then embeds those strains as a predefined expansion/contraction in a coarse part-scale model [189].

Over the past few years, the modified inherent strain method (MISM) has been refined to capture the peculiarities of PBF processes [190]. Unlike the classical method (which assumed a constant plastic strain after cooling), MISM treats inherent strain as dependent on the thermal history of each layer. It separates contributions from thermal shrinkage and plastic deformation, applied layer-wise, to better mimic the accumulation of stress in a tall build [191]. This layer-by-layer inherent strain application greatly improves distortion predictions for additive builds. For example, Dong et al. showed that incorporating temperature-dependent material properties into the inherent strain calibration (applying the strain at an intermediate elevated temperature rather than only at ambient) reduced residual stress prediction errors from ~46% down to ~9% in a benchmark wall, and similarly cut distortion error from ~30% to ~8% [192]. More recently, an Inherent Strain Rate Method (ISRM) has been proposed to include viscoplastic, rate-dependent effects in the strain calculation. By treating the inelastic strain increment as a rate-dependent quantity (accounting for creep/relaxation during layer deposition), ISRM can capture time-dependent stress relaxation that MISM ignored, further enhancing accuracy in residual stress and deformation predictions [193].

These improvements do incur higher computational overhead (e.g., the advanced two-step MISM procedure increased solve time by ~5×), but they remain far cheaper than a fully explicit melt-pool-scale simulation of an entire part. In practice, many commercial AM simulation tools now implement some form of inherent strain or sequential thermal–mechanical approach, allowing engineers to predict warpage, residual stress distributions, and even crack-prone regions in complex geometries. Additionally, researchers continue to explore hybrid modeling for mechanics, such as combining analytical solutions with finite element results to expedite calculation of part-scale stress fields [194]. The overall trend is toward multi-scale thermo-mechanical modeling. Using high-fidelity sub-models to inform efficient part-scale simulations, thereby achieving both accuracy and tractability.

### 5.7. Other approaches

In addition to the previously mentioned approaches, additional views should be considered. One such technique is to examine the packing density of the powder layer, which is an essential element determined during the powder-spreading process [195]. This density considerably impacts the interaction of powder particles with the heat source or binder, which in turn influences the characteristics of the finished components. Denser powder layers, for example, provide more stable and continuous fusion in L-PBF [196] and EB-PBF [197], decreasing defects in manufacturing such as balling, shrinking, and porosity. As a result, modeling the powder-spreading process becomes an appropriate choice. Fig. 8 shows one of the results of a non-uniform single track from the top view.

Some researchers have turned to experiments and numerical simulations to overcome the challenge of directly measuring the packing density of thin powder layers. These investigations focus on studying powder packing density under conditions resembling powder heaps, where particles naturally form piles [198] or are deposited in cylinders [199], or rectangular containers [200], with dimensions several orders larger than the powder size.

Beyond providing mechanistic insight, multiscale models play a critical role in supporting data-driven defect detection frameworks. Simulated melt pool geometry, thermal gradients, and solidification conditions can be used to generate physically meaningful features and synthetic datasets for training ML models. In this way, numerical modeling serves not only as an explanatory tool but also as a direct enabler of defect detection by generating physically consistent synthetic datasets, defining defect labels, and bridging raw sensor signals with data-driven classification models, particularly when experimentally labeled defect data are limited.

To support a horizontal comparison across the modeling landscape,

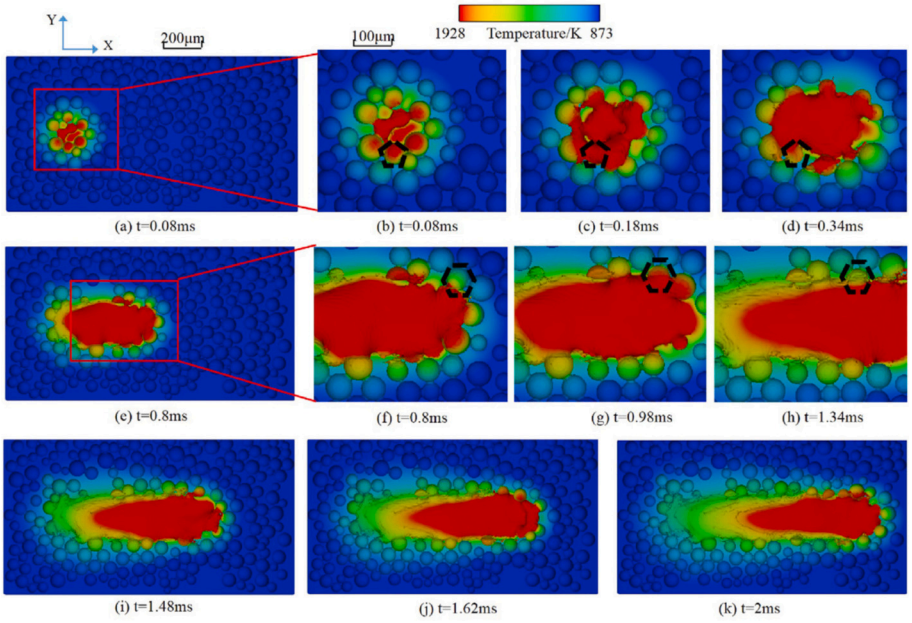



**Fig. 8.** Simulation results of the formation process of a nonuniform single track [201].

**Table 2**
Comparative summary of representative mechanistic and numerical modeling approaches for PBF-AM.

| Process | Model category | Scale | Numerical method | Software/code | Material | Defects | Key outputs | Validation | Ref. |
|---|---|---|---|---|---|---|---|---|---|
| L-PBF | Thermal fluid (keyhole) | Powder/track-scale (3D) | FE/VOF CFD (ALE3D) | LLNL ALE3D | 316L | Keyhole pores, spatter | 3D powder-scale: recoil-pressure flow → keyhole depression + pore/spatter mechanisms; multiple pore modes. | Qualitative match to observed spatter/pore trends | [202] |
| L-PBF | Keyhole stability | Track-scale (in situ) | In situ X-ray + CFD | APS + in-house | Ti–6Al–4V | Keyhole pores | X-ray showed keyhole collapse at turn-arounds traps gas → pores; power modulation stabilizes keyhole depth. | Synchrotron X-ray + ex situ pore quantification; mitigation validated by reduced porosity. | [203] |
| L-PBF | Keyhole stability | Track-scale (in situ) | High-speed X-ray + analysis/CFD | APS + modeling | Ti–6Al–4V | Keyhole pores | Identified keyhole-tip oscillations above threshold → cavity instability + pore pinch-off; cross-material trends. | In situ X-ray, compared with modeling/analysis of instability thresholds. | [204] |
| L-PBF | Keyhole threshold | Track-scale (in situ) | In situ X-ray imaging | APS | Ti–6Al–4V | Keyhole pores | Mapped conduction keyhole transition; deep unstable keyhole above threshold; pores cluster near turn points; normalized enthalpy proposed. | X-ray keyhole morphology + ex situ XCT pore stats. | [205] |
| L-PBF | Thermal (FE) | Track/layer-scale | 3D transient FE | ABAQUS | – | Melt pool overlap (LoF risk) | Early 3D FE: transient T-field + melt pool size; scan spacing/layer reheating govern overlap + gradients. | Melt pool dims vs micrographs; absorptivity calibration required. | [206] |
| L-PBF | Residual stress (analytical + FE) | Layer/part-scale | Analytical + FE | ABAQUS | Ti–6Al–4V | Distortion, cracking risk | Analytical residual stress trends + FE layer accumulation; scan alternation reduces warpage. | Distortion + XRD stress trends (qualitative). | [46] |
| L-PBF | Residual stress/distortion | Part-scale | Multi-scale FE + inherent strain | ABAQUS + subs | Ti–6Al–4V, IN718 | Distortion, stress | Multi-scale FE predicts residual stress + distortion for complex parts; scan optimization reduces peaks. | Neutron diffraction + deformation measurement. | [207] |
| L-PBF | Thermo-mech (reviewed FE) | Multi-scale | Survey (FE methods) | Multiple | Various | Stress/distortion | Review of FE approaches: activation/inherent strain; sensitivity to absorptivity/material data. | Cross-study comparisons to literature measurements. | [208] |
| All | Multi-physics modeling (review) | Multi-scale | FE/CFD/CA/PF | – | Various | Multi-defect | Thermal-fluid → microstructure → properties; gaps in predictive/control readiness. | Reviews validation approaches across studies. | [7] |
| All | Fundamentals (overview) | Multi-scale | Analytical + numerical | – | Various | Multi-defect | melt pool-powder interaction, thermal gradients; early modeling landscape. | Literature correlation (qualitative). | [209] |
| L-PBF | Microstructure (phase-field) | Track/layer-scale (3D) | 3D PF + nucleation | Custom | 316L | Grain evolution | 3D PF predicts competitive epitaxy + remelt/re-nucleation; nanoparticle refinement captured. | EBSD + thermal/melt pool trend comparisons. | [210] |
| L-PBF | Microstructure (CFD + PF) | Track-scale | CFD → PF coupling | OpenFOAM + MICRESS | Fe–17Cr | Dendrite morphology | Melt pool CFD feeds PF: predicts PDAS/SDAS + remelt effects (single vs overlap). | SEM dendrite spacing/morphology (≈10–15%). | [181] |
| DED/WAAM | Microstructure (FE + CA) | Multi-layer wall | FE thermal → CA | SYSWELD + CA | 921A steel | Grain/phase maps | FE thermal cycles drive CA grain growth + phase evolution; predicts spatial gradients. | Metallography + hardness profile (good trend match). | [211] |
| DED/WAAM | Microstructure + hardness | Multi-layer wall | FE + kinetics + hardness | MSC Marc | Low-C steel | Phase fraction, hardness | Thermal history → martensite fraction + grain size → hardness gradients (top vs bottom). | Microhardness + microstructure maps (~15% grain size). | [212] |
| L-PBF | ML-enhanced thermal | Part/track (surrogate) | FE + NN surrogate | ABAQUS + Python | IN738 | Thermal stability | NN surrogate predicts thermal histories fast; enabled real-time adjustment to stabilize pool temperature. | Compared vs FE + thermocouples; closed-loop validated by IR. | [213] |
| DED/WAAM | ML-enhanced (PINN) | Part/layer thermal field | PINN (physics-informed) | TensorFlow | ER70S-6 | Thermal control | PINN predicts temperature fields ahead in time; transferable across geometries. | FE + IR thermal validation; control-ready. | [214] |
| L-PBF | Thermal–fluid (SPH) | Powder/track-scale | Multi-res SPH | Custom | 316L | Keyhole, spatter | Multi-res SPH captures melt flow, keyhole onset, spatter/denudation trends vs power. | Qualitative imaging/X-ray consistency; pool dims ~10–15% vs literature. | [215] |
| PBF | Thermal–fluid (LBM) | Powder-scale (meso) | LBM | In-house | Ti–6Al–4V | LoF, balling | LBM resolves powder melting/wetting; predicts LoF threshold + balling vs continuous tracks. | Micrograph-based qualitative agreement; threshold trends match density curves. | [216] |
| DED | Thermo-mechanical | Part-scale | Coupled thermo-mechanical FE | In-house/commercial FEA | Ti–6Al–4V | Distortion/stress | 3D FE model predicts distortion and residual stresses under DED | Calibration and validation against measured distortions and temperature histories | [217] |
| DED/WAAM | Thermo-mechanical | Multi-layer wall | Thermo-mech FE | SYSWELD | Low-C steel | Distortion/stress | Early WAAM FE: thermal cycles + stress accumulation/relaxation; clamp stiffness effect. | Distortion + hole-drilling/XRD stress support. | [218] |
| DED/WAAM | Thermo-mechanical | Multi-layer wall | 3D FE | ABAQUS | Ti–6Al–4V | Distortion/stress | Inter-layer dwell time reduces residual stress/distortion; guidelines for dwell selection. | Distortion + thermocouple thermal cycles. | [219] |
| DED/WAAM | Thermo-mechanical | Multi-layer wall | Nonlinear FE | Simufact | HSLA steel | Distortion | Shows constant properties underpredict distortion; recommends T-dependent + phase effects. | Laser scan distortion + thermocouples | [220] |
| DED/WAAM | Thermal–fluid | Track/bead-scale | CFD heat + flow | In-house | ER70S | Porosity between beads | Enhanced heat source + convective pool flow; better bead shapes; bead merging + pore entrapment. | IR + macroetch bead geometry | [221] |
| DED | Thermal–fluid (multiphase) | Track/bead-scale | CFD + phase change | In-house/COMSOL | Ti–6Al–4V | Melt pool geometry & phase transitions | CFD predicts melt pool dimensions and temperature fields; phase change dynamics included | Compared with experimental pyrometry and cross-section measurements | [222] |
| L-PBF | Distortion (inherent strain) | Part-scale | FE (inherent strain) | COMET | IN718 | Distortion/stress | Inherent strain extracted from local thermo-mechanical simulations and applied to full-part distortion prediction | Comparison with 3D scan distortion measurements and residual stress trends (XRD/literature) | [223] |
| L-PBF | Thermal-fluid (CFD/VOF) | Track-scale | FV CFD + VOF | OpenFOAM | 316L | Keyhole pores, spatter | Evaporation + recoil + Marangoni: conduction → keyhole; pore bubbles + spatter mechanisms; oscillations. | Qualitative operando X-ray/video consistency; pool trends match. | [202] |

Table 2 summarizes representative journal studies covering (i) FE-based thermal and thermo-mechanical models, (ii) thermal–fluid and keyhole stability simulations, (iii) microstructure frameworks, and (iv) ML-enhanced hybrid/surrogate approaches. The table highlights each model's scale, numerical method, key outputs, and validation route to clarify how different modeling levels contribute to defect prediction and process understanding.

### 5.8. Limitations of numerical modeling

Despite substantial progress in numerical modeling of L-PBF, several fundamental limitations continue to constrain predictive accuracy, computational efficiency, and practical applicability. L-PBF is inherently a highly complex process governed by tightly coupled multi-physics phenomena occurring across a wide range of spatial and temporal scales. Microscale events such as powder–laser interaction, melt-pool dynamics, and rapid solidification occur over microseconds, while residual stress accumulation and part-scale thermal evolution develop over hours or even days. The coexistence of extreme temperature gradients, rapid heating and cooling rates, and non-equilibrium solidification introduces significant uncertainty in process behavior and material response, making accurate and comprehensive modeling particularly challenging. Moreover, capturing the interplay between metallurgical transformations and defect formation requires a holistic understanding of the entire L-PBF process chain [224].

To render simulations computationally tractable, most numerical models rely on simplifying assumptions, including constant or weakly temperature-dependent material properties, idealized boundary conditions, and the neglect of phenomena such as powder spatter, evaporation, or plume dynamics. While these assumptions reduce computational cost, they inevitably introduce discrepancies between simulated results and real LPBF behavior. In addition, finite-element and finite-volume models are often sensitive to mesh resolution, and inadequate discretization can significantly influence predicted thermal fields, melt-pool geometry, and solidification behavior, necessitating careful mesh-dependency assessments [225].

Another critical limitation lies in the high computational cost associated with high-fidelity multi-physics simulations that simultaneously resolve fluid flow, heat transfer, phase transformations, and free-surface dynamics. The resulting trade-off between model accuracy and computational efficiency restricts the applicability of such models for real-time process monitoring, feedback control, or large-scale parametric studies [225].

Model reliability is further constrained by the availability and accuracy of material property data. Numerical predictions depend strongly on temperature-dependent thermophysical and thermodynamic properties, such as thermal conductivity, specific heat, surface tension, and phase fractions, which are difficult to measure under the extreme thermal conditions characteristic of L-PBF [225]. Experimental validation is equally challenging, as in situ characterization of transient phenomena—including melt-pool morphology, keyhole behavior, and vapor plume dynamics—remains limited. Consequently, discrepancies between simulations and experiments are frequently reported, underscoring the need for advanced sensing techniques and more robust validation strategies.

Defect prediction represents an additional layer of complexity. The formation of defects such as lack-of-fusion porosity, keyhole-induced voids, or hot cracking is highly sensitive to local process conditions, material variability, and thermal history. Small variations in laser parameters, scan strategy, or powder characteristics can lead to substantial differences in defect populations. Furthermore, many existing studies treat metallurgical evolution and defect formation as separate modeling problems, limiting insight into how microstructural transformations directly influence defect nucleation and growth [224].

## 6. Machine learning algorithms

Machine learning has emerged as one potential strategy for tackling AM issues. The fundamental goal of ML is to create algorithms that allow computers to learn independently by finding patterns and revealing statistically significant trends in data. This learning method evaluates complicated data sets to find anomalies, predict outcomes, and improve process parameters. Adaptive programming is an essential approach in ML because it allows computers to spot patterns, learn from errors, develop new insights, and enhance processing speed and accuracy. ML approaches are especially good at dealing with high-dimensional data, making them relevant across numerous applications, including process optimization, defect identification, and predictive maintenance in AM systems [226]. ML approaches are classified according to the goals they want to attain, such as supervised, unsupervised, semi-supervised, and reinforcement learning (RL). These categories assist in categorizing algorithms based on the type of learning necessary to correctly translate inputs to desired outputs.

Supervised learning is one of the primary types of machine learning, divided into regression (predicting continuous outputs) and classification (predicting discrete categories). In this approach, labeled data is used during a two-phase process: training, where the model learns from the data, and testing, where predictions are validated using unseen samples. Algorithms such as linear regression, decision trees, random forests, support vector machines, and multi-layer perceptrons use statistical methods and tuning techniques like grid search and cross-validation to optimize performance and avoid overfitting or underfitting. More advanced models like ANN and CNN have been particularly successful in handling complex data like images, mimicking the structure and function of the human brain to extract patterns and make decisions.

On the other hand, unsupervised learning operates without labeled data, aiming to uncover hidden structures and patterns in the input. Techniques such as clustering (k-means, hierarchical), dimensionality reduction (Principal Component Analysis (PCA), Independent Component Analysis (ICA)), and data mining methods are employed to group similar data points or reduce data complexity. Semi-supervised learning bridges the gap between supervised and unsupervised approaches by leveraging a small amount of labeled data alongside a larger set of unlabeled examples to improve model accuracy. Lastly, reinforcement learning, inspired by behavioral psychology and optimal control theory, involves training agents to interact with an environment, learning optimal behaviors over time by maximizing cumulative rewards through techniques such as dynamic programming and value function optimization.

This study evaluates all PBF techniques and ML approaches used in this field. To the best of our knowledge, approximately 90% of the assessed studies focus on L-PBF, with the remaining 10% on EB-PBF. The comparatively low percentage of EB-PBF can be attributed to its novelty, which needs more ML integration research and development. Supervised learning approaches account for approximately 60% of all ML methods. Unsupervised learning accounts for approximately 12% of the remaining methodologies, followed by semi-supervised learning at 12%, classic statistical methods at 10%, and reinforcement learning at 6%.

## 7. Implementing machine learning in powder-based AM

When combined with physics-based modeling, ML methods can move beyond black-box classification toward mechanism-aware defect prediction. Model-informed features, physics-based constraints, and simulation-augmented datasets improve robustness and generalization across materials and machines. Such integration enables the translation of sensor data into actionable process knowledge, forming the basis for future closed-loop control strategies in PBF.

### 7.1. Statistical methods for prediction

Statistical approaches such as regression analysis have found relationships between process factors and experimental part porosity. The established regression models were used to estimate component porosity over various process factors. AlFaify et al. conducted regression analysis using ANOVA analysis to correlate part porosity, measured via metallographic analysis, with process parameters, including laser power, scan velocity, layer thickness, and hatch space in PBMAM [227]. Similarly, Tapia et al. employed a regression analysis using the spatial Gaussian method to correlate part porosity, measured by the Archimedes method, with process parameters [228].

Furthermore, Garg et al. used the genetic algorithm to do a regression analysis to link process parameters with open porosity on the part surface [229]. In addition, EB-PBF has become a viable method for producing complex-shaped components from heat-cracking-sensitive materials like AISI H13 hot-work tool steel, thanks to the decade-long rapid growth of technology in this field. A correlation between surface topography, internal porosity, and process parameters has been established, with a highly robust model describing the correlation between internal porosity and melting process parameters ($R^2_{adj} = 0.91$), as well as topography parameters and melting process parameters ($R^2_{adj} = 0.77–0.96$) [230].

### 7.2. Supervised learning methods

In defect classification, extensive efforts have been devoted to employing supervised ML methods, utilizing various inputs such as images, melt pool thermal images, optical images, AE signals, and data from computed tomography (CT) scans. Jingcnag et al. introduced a CNN-based multi-sensor fusion approach for in-situ quality monitoring of L-PBF [231]. Similarly, Zheren Song presented a hybrid deep generative prediction network (HDGPN) utilizing a variational autoencoder and Generative Adversarial Neural Network (GAN) to characterize complex pore microstructure and predict pore morphology under arbitrary processing parameters from images [232].

In addition, Imani et al. created a Deep Neural Network (DNN) model for the L-PBF process that uses spatial characterization pictures for real-time identification of incipient geometry flaws [233]. Additionally, Scime et al. identified and classified six different types of defects from pictures using a CNN algorithm for autonomous anomaly detection and classification architecture in L-PBF, as its of CNN is illustrated in Fig. 9 [234]. Employing high-speed Field-Programmable Gate Arrays or Application-Specific Integrated Circuits for data acquisition, alongside efficient CNNs, can enable the utilization of readily obtainable data for predicting a broader range of properties in real time and for closed-loop process control. Beyond optical or near-optical imaging, ultrafast X-ray imaging has been deployed to investigate the fusion mechanism [235,236] and irregularities in melt pools [237] in PBF.

In response to the poor adaptability and complexity of existing ML detection algorithms, one study proposed an improved version of the You Only Look Once version 3 (YOLOv3) algorithm to detect surface defects in metal AM based on multi-spectrum data (visual light/IR camera). The weighted k-means algorithm was employed to cluster target samples, enhancing the matching degree between the prior frame and the feature layer. Additionally, the network structure of YOLOv3 was modified and replaced with the lightweight structure of the original YOLOv3 algorithm [238]. These AI deep learning approaches have come a long way in recent years, especially in computer vision, where “You Only Look Once” (YOLO) has become a state-of-the-art method for a variety of tasks, such as object recognition, picture categorization, and segmentation [239].

When tested on a publicly available metallographic dataset, an end-to-end architecture for microstructural defect identification using YOLOv8 models, one of the pre-trained models for the computer vision area, produced excellent results. Compared to previous automatic defect recognition approaches, the YOLOv8 model rapidly recognized fractures and porosity in the metal AM dataset, increasing defect detection accuracy to 96% in just 0.5 h [240].

A dual-input CNN that fused defect parameter vectors and layer-wise pictures was proposed in a different research that employed an axis CMOS camera monitoring system to provide real-time online defect monitoring in the L-PBF process through a paraxial CMOS camera monitoring system. This model achieved recognition accuracies surpassing 80.00% for all defect categories by integrating picture and parameter information linked to defect creation. Furthermore, compared to traditional deep learning algorithms, this approach performed better than single-image input techniques, with a low parameter count, quick training time, and quick prediction speed, making it more appropriate for real-time live monitoring scenarios [241].

In another study, a fresh method was developed for the real-time identification of surface deformation issues from powder-bed images, employing a CNN-based solution in L-PBF. EOS machines with the EOSTATE suite, comprising four monitoring systems, including

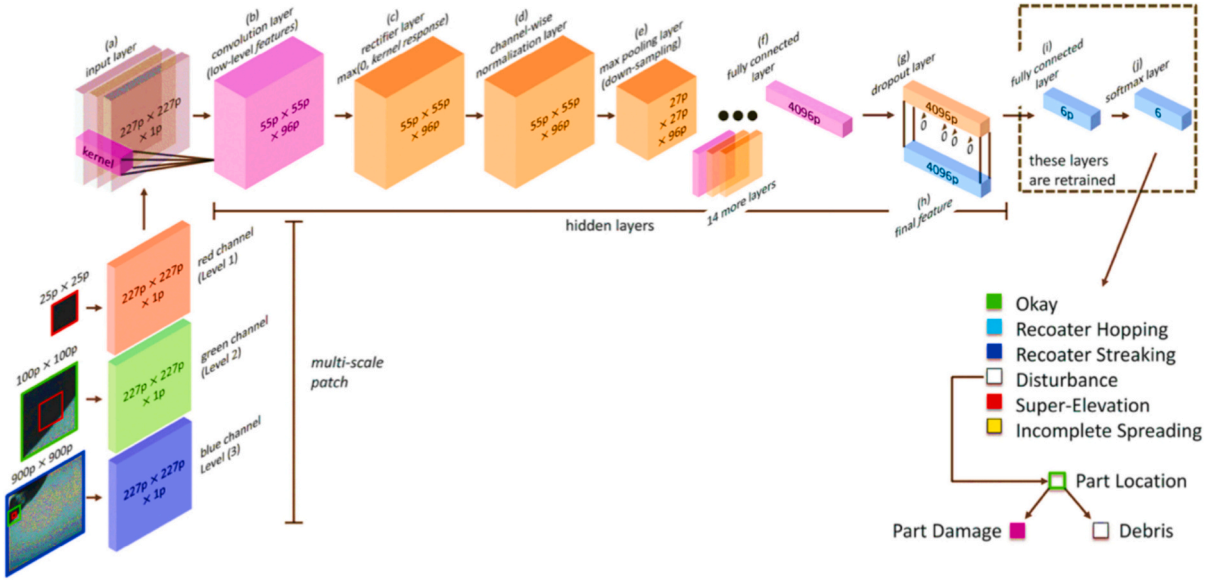



**Fig. 9.** Flowchart of implementing the MsCNN ML technique [234].

EOSTATE Exposure OT, EOSTATE Melt pool, EOSTATE System, and EOSTATE powder-bed supervision, achieved 99% classification accuracy for standard and defective prints [242].

A framework for defect identification in metal AM processes was presented using in-situ high-speed cameras. This approach sought to quickly classify regular and faulty prints by computer simulation and experimental investigation [243]. A Bayesian classifier was developed and trained in the L-PBF method to identify construction quality, indicating layers or areas that were deemed undesirable or faulty. These findings may direct process control in close to real-time, inform subsequent choices, or stimulate remedial measures [244].

A pioneering real-time monitoring system was proposed in a separate study to detect defects utilizing PCA and SVM automatically. This system used a coaxially mounted camera to capture molten pool images, extracting ten pool features via PCA to reduce dimensionality. Subsequently, an SVM classifier was employed to identify defects in the deposited layer, achieving a high detection rate for slag and bulge defects [245]. To discover defects, other researchers investigated the optical image characteristics. For example, Jiaming Li used optical microscopy (OM) pictures under different settings to construct a supervised classifier model [246]. In contrast, Jingchang Li used three clever ML methods to analyze 2D pores using OM characteristics [247]. Furthermore, Claudia Schwarz used the EOSTATE Exposure OT system for process monitoring using supervised classification approaches [248].

Furthermore, Convolution Neural Networks (CNNs) for infrared imaging have shown significant potential for real-time process monitoring. When compared to visible wavelength imaging, IR imaging has fewer sophisticated CNN requirements [249], needing less powerful processing equipment and allowing for quicker computations. This stresses the need to select a wavelength range for real-time imaging, particularly in closed-loop control settings where fast adjustments may be required.

Despite advancements in processing speed, the utilization of CNNs has primarily been confined to process monitoring due to the time required between data acquisition, processing, and subsequent action-taking. Moreover, Khanzadet al. used supervised learning techniques to create a black-box model for the probability distribution of class labels, such as porosity, based on data features like melt pool attributes. They used a thermal monitoring system to record time-varying melt pool signals [250]. The overall procedure from Thermal image to porosity prediction is depicted in Fig. 10. A related study used high-speed thermal emission measurements from the melt pool to identify defective individual struts in lattice structures.

A defect prediction calculation based on logistic regression of melt pool thermal emission aggregated over many layers was devised, and it predicted strut existence or defectiveness with over 94% accuracy [251]. Furthermore, it was demonstrated that short-wave IR thermography may predict discrete sub-volumes in L-PBF components for local porosity. A trained 1D CNN model showed positive findings, with an R2 score of 0.93 for predicting porosity in specific sub-volumes, indicating outstanding performance in porosity prediction [252]. Furthermore, merging deep learning-based neural network topologies with thermographic off-axis imaging showed promise for defect detection, with an impressive 96.80% accuracy in recognizing L-PBF-specific defects [253].

Considering the substantial memory requirements, computational expenses, and data density associated with high-resolution imagery, researchers have pursued alternative avenues utilizing numerical data derived from instrumentation. For instance, AE signals have emerged as a valuable input for defect detection in AM processes.

Ye et al. suggested a defect identification approach for the L-PBF process that uses SVM and features gathered from recorded acoustic signals to predict different melting stages accurately [265]. Ito et al. included an online monitoring system consisting of two AE sensors in the L-PBF process, detecting the occurrence time and location of microcracks and holes based on the time domain and amplitude difference of AE signals, with spatial positioning error maintained to 2–3 mm [254]. Kononenko et al. developed an in-situ monitoring system for fracture diagnosis in L-PBF by combining AE sensing with an ML model. They found that using the spectral components of AE signals as input

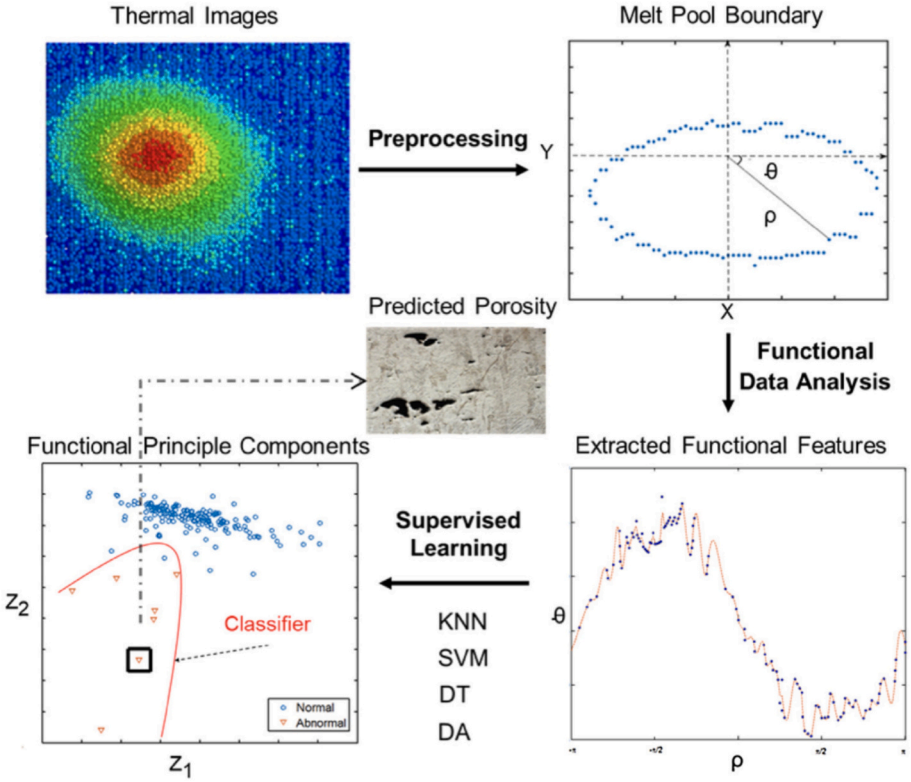



**Fig. 10.** Demonstration of porosity prediction using supervised machine learning [250].

resulted in the highest prediction accuracy [255].

Airborne AE sensing reduced structural noise and allowed for more flexible installation. Pandiyan et al.'s investigation of AE characteristics in L-PBF under different laser regimes revealed a strong correlation between AE features and melting mode, with laser energy density being the primary component determining AE characteristics [256]. Shevchik et al. divided samples into low, medium, and high-quality categories based on part porosity ratings using AES and ANN analysis [49]. With a laser Bragg grating acting as the acoustic sensor element, the system was able to classify flaws into the appropriate part category with an accuracy rate of about 80%. This demonstrates how ML approaches are now effective in simplifying the interpretation of complicated AE data from the PBF process.

Similarly, CT has become a powerful method for defect diagnosis, providing non-destructive examination throughout the entire volume. Researchers used CT data from X-ray images as input for supervised machine learning algorithms to categorize defects. In-situ X-ray imaging offers excellent spatial resolution, promising to improve basic physical processes in PBF. However, the potential of X-ray imaging for real-time process control is still largely unexplored. Jiafeng Ye et al. investigated LR-XCT scanning settings to classify defects [257], and Mathieu Vandecasteele used XCT to identify pore types based on geometric features using supervised learning methods [258].

Ubaid Aziz et al. used XCT data and supervised machine learning, including classification algorithms such as KNN and DT, to automatically identify distinct defects in AM-produced nickel alloys [259]. G. Minerva used classical extreme value statistics with supervised machine learning approaches, and specifically X-ray micro-CT parameters as input data, for defect analysis [260].

Arun Poudel et al. achieved great accuracy compared to traditional statistical and threshold-based techniques in classifying pore types utilizing nine parameters acquired from XCT through supervised DT and ANN [48]. The representation of defects in the 3D box and its classification are illustrated in Fig. 11. These studies highlight the effectiveness of numerical data for defect identification and classification in AM processes, which may be obtained via devices like CT scans and AE signals. Besides numerical data from CT images, in a particular study, to discern pixel data from CT images as pores or inclusions from L-PBF, the proposed methodology employs SVM, a supervised ML algorithm trained with an Area Under the Curve (AUC) of 0.94.

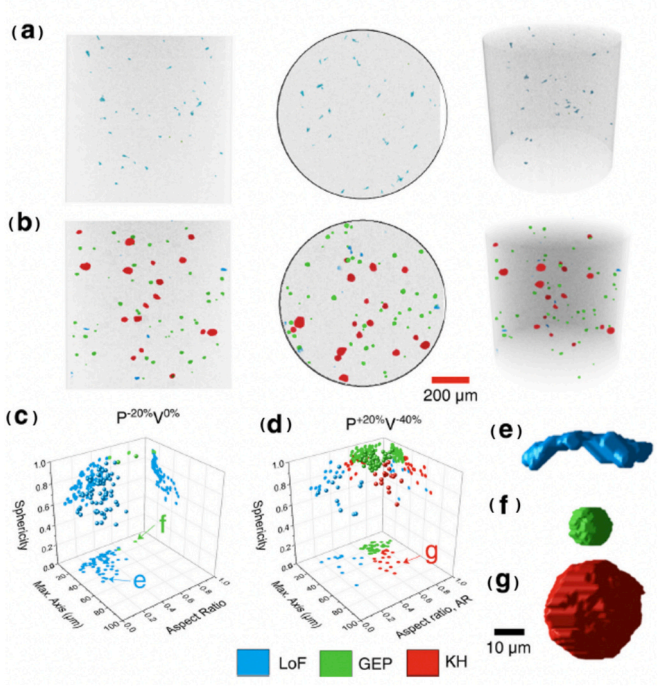



**Fig. 11.** Visualization of volumetric defects in L-PBF coupons. Front, top, and isometric views of the XCT scan region of coupons fabricated using (a) P − 20% V0% and (b) P + 20%V − 40% parameters. Scatterplots in the 3D space of size, aspect ratio, and sphericity show the volumetric defects observed in (c) P − 20%V and (d) P + 20%V − 40% coupons. Appearances of selected defects, (e) a LoF, (f) a GEP, and (g) a KH-Induced porosites, are also shown [48].

Another study investigated two labeling procedures using computer-aided design (CAD) files and XCT scan data. A unique CNN was trained from scratch and optimized by fine-tuning many hyperparameters with a Hyperband tuner. The model obtained 90% accuracy with CAD-assisted labeling and 97% with XCT-assisted labeling, recognizing holes as small as 0.2 mm. The study presented two labeling methodologies, CAD-assisted and XCT-assisted, for in-process image labeling of test cylinders with seeded holes ranging in size from 0.02 mm to 2 mm, intending to distinguish pore and non-porosity pictures [261].

Despite their high accuracy in defect classification, supervised deep learning models such as CNNs and DNNs often face challenges in real-time deployment due to memory and processing demands. Additionally, their generalization across different machines or materials may be limited unless augmented with simulation-informed datasets or retrained on diverse experimental data.

### 7.3. *Unsupervised machine learning methods*

Previous research has demonstrated that ML approaches, mainly supervised algorithms, are robust and accurate in defect classification tasks. However, one key restriction of supervised ML is the manual labeling procedure, which requires significant time and skill, limiting its application to diverse materials and AM processes. Researchers are turning to unsupervised machine learning algorithms that recognize significant data properties without labeled input to overcome this challenge.

This change to unsupervised learning not only decreases the need for manual labeling but also enables researchers to use automatic pattern recognition while still requiring human supervision to understand complicated discoveries. Unsupervised learning approaches such as SVD, agglomerative hierarchy, PCA, K-means clustering, SOM, and agglomerative hierarchy have become popular in AM-based scenarios, particularly for a broad range of data sources such as pictures, thermal imaging, IR imagery, and AE signals. Luke Scime, for example, used computer vision to identify six types of defects during the powder spreading process, using k-means unsupervised clustering for automated defect detection and classification [262]. Similarly, Marco Grasso proposed employing photo k-means clustering analysis to automate defect detection and localization in each layer [263].

Grasso et al. utilized PCA and K-means clustering to continuously acquire images through an off-axis-mounted thermal camera to detect unstable melting conditions [264]. Examples of this research are illustrated in Fig. 12. Although this method is susceptible to the choice of hyperparameters and its results vary greatly depending on the density and distribution of data, its application on visible-NIR camera data could be considered to predict the melt pool dimension [265].

Unsupervised machine learning models have also been used in CT scanning to classify defects. Taherkhani, for example, used an unsupervised machine learning method (SOM) to identify abnormalities in light-intensity data and determine their placements using post-processing CT scans [266]. Similarly, Robert Snell used K-means unsupervised clustering on 3D pore data from XCT and 2D pore data from microscopy across several alloys [267].

Nonetheless, lacking validation metrics is a significant difficulty in unsupervised machine learning systems. Unlike supervised learning, unsupervised learning does not allow for external validation through test datasets. Instead, internal validation measures are used to determine group similarities and variances.

Furthermore, while SOM is widely used for visualization, simple K-

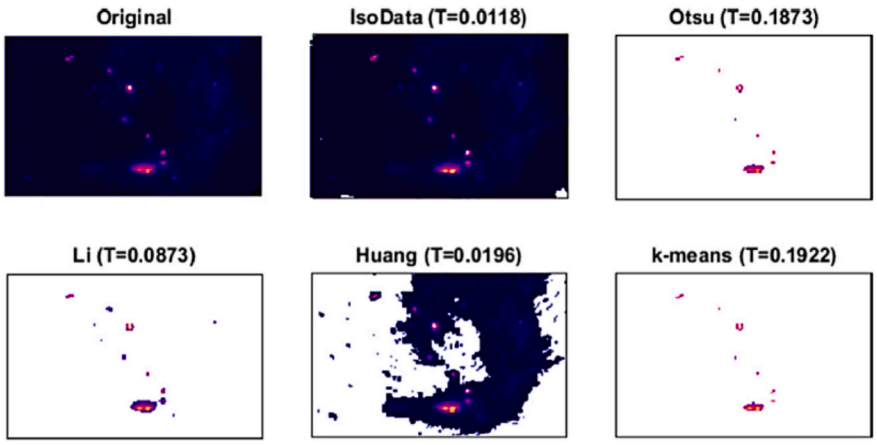



**Fig. 12.** Example of an IR image where only the LHZ and the spatters are evident, and Segmentation results based on IsoData, Otsu's, Li's, Huang's, and k-means methods [264].

means may not always capture underlying patterns adequately. Another alternate approach for L-PBF noisy data is density-based spatial clustering with the application of noise (DBSCAN). DBSCAN is then used to split the discovered pixels into discrete faults, followed by a convex hull to define the clusters based on their size and shape. The final classification involves segmenting the CT scan picture and classifying each pixel as background, pore, substance, or inclusion. Additionally, 2D defect clustering is conducted using K-means, while 3D is accomplished using DBSCAN [268].

In other words, a hybrid learning technique that mixes labeled and unlabeled data has been devised to use both benefits. Okaroa et al. [269] introduced a semi-supervised ML strategy for automatic defect identification in laser-based AM. Fig. 13 depicts many random outcomes from this investigation. Their findings, which came from tensile test bars constructed from Inconel 718, reveal that the semi-supervised ML system successfully identified laser-based manufacturing defects in the

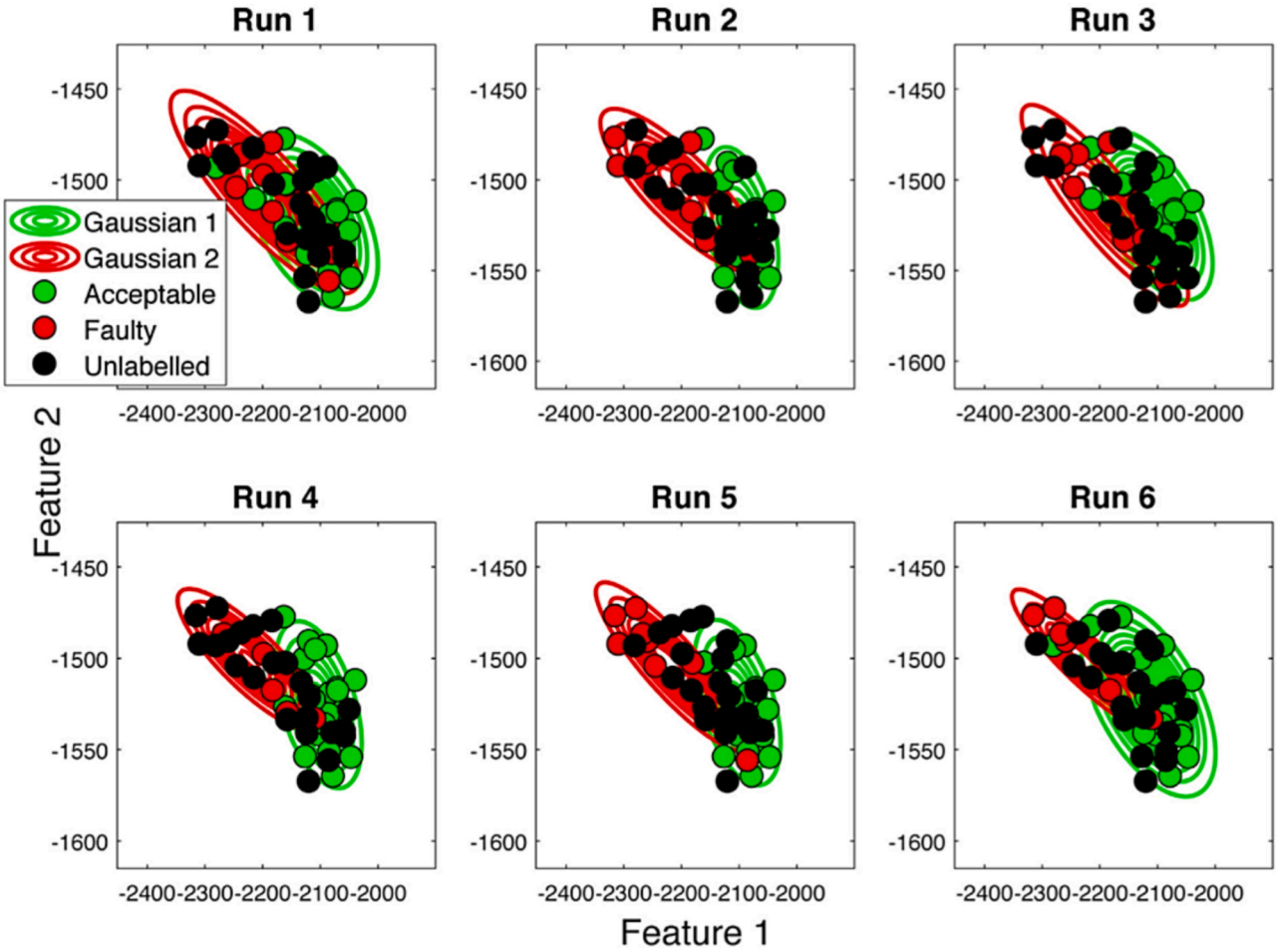



**Fig. 13.** SSL results obtained for six runs of a Monte Carlo simulation where, for each run, 24 unlabelled points were selected randomly [269].

product, generating results comparable to those from completely labeled training data. In the other work, Yadav et al. proposed a semi-supervised approach to detect inline drift in the L-PBF process by utilizing certified product CT as input data [270]. This method uses labeled data from an unsupervised ML K-means clustering methodology to train a supervised ML-based KNN algorithm. Semi-supervised CNNs boost flaw detection efficiency in AM methods by overcoming the challenges of acquiring large-scale labeled data. Similarly, Li et al. proposed a DCNN model to assess the quality of the final product during the metal printing process. Their approach used semi-supervised training data to decrease the need for vast labeled picture data. The suggested algorithm identified under-melt, typical, and over-melt situations in products containing ASTM F75 CoCrMo powder with 100% accuracy [271].

This involved developing an ML model to categorize surface appearances using reference monitoring data. The following classification, post-process properties, including surface roughness, morphology, and tensile strength, are associated with the appearances. Thanks to this association, key features, such as anomaly-free, lack-of-fusion, and hot areas, suggest the printed sample quality. Predictions made on test samples with different geometries served as additional validation of this ML approach's efficacy [272].

Moreover, when there are few labeled samples, an innovative CNN architecture with a mutual correction classifier and an SSL approach utilizing soft pseudo labels was suggested to improve defect inspection accuracy. The performance of the technique was shown on two benchmark datasets: one widely used for industrial defect inspection, and the other is a realistic dataset containing pictures of real injection molding manufacturing lines. The suggested technique produced an accuracy of 99.03% on the benchmark defect dataset, which is around 13.2% higher than previous methods when the training dataset had just 45 labeled photos and 135 unlabeled samples per category [273]. Furthermore, reference monitoring photos were used to train the semi-supervised ML model, which classified the surface appearances of samples produced with and without typical L-PBF problems, such as overheating. This trained ML model makes detecting overheated areas in L-PBF products easier during printing [274].

There has been little study in the field of RL on optimizing agents' actions to maximize cumulative rewards under certain situations. Wasmer et al. used RL to evaluate acoustic data obtained during printing AE methods to develop quality monitoring in AM [275]. The technique achieved excellent classification accuracy for a cuboid form made of stainless steel 316L, showing a high degree of in situ and real-time application potential. Yao et al. have created a sensor-based product quality control model for the AM process, which employs a restricted Markov decision process [276]. This strategy has not been widely used, but it is a great place to start. According to relevant literature, more study is needed, particularly when estimating surface roughness in L-PBF [277]. The CNN architecture of this research is illustrated in Fig. 14.

Unsupervised models, including PCA, K-means, and SOM, offer the advantage of working with unlabeled datasets, reducing manual labeling effort. However, their performance can be sensitive to noise, hyperparameter choices, and data density, which may limit robustness across different machines or powder materials. Hybrid or semi-supervised approaches can help mitigate these challenges by combining labeled and unlabeled data to improve generalization.

### 7.4. Utilizing new algorithms

Recent advances in using new approaches for defect identification in the PBF have shown promising outcomes. Ye et al. used a microphone to record AE signals during L-PBF and then discovered a correlation between these signals and process parameters. They used a deep belief network to detect defects based on AE signals, demonstrating that their intelligent identification approach was more accurate and efficient than standard techniques [87].

Researchers employed CAD models with certain artifacts to focus on defect identification instead of categorization in a different study. They used CAD-based simulations to create realistic training data using a GAN. The first stage's data was then used to train a DNN, which produced accurate 3D reconstructions. Promising results were obtained when this strategy was used in two case studies employing X-ray pictures from AM procedures [278]. A different examination looked into several defect categories, such as holes, spattering, incandescence, horizontal, vertical, and profile monitoring of printed components. In addition to layer-wise monitoring of the printed component profile, the study proposed a low-cost camera-based in-situ monitoring system for metal PBF that allowed real-time identification of five different defects. The technology further enabled the offline production of synthetic pictures via GAN for dataset augmentation [279].

Reinforcement learning and generative models such as GANs show potential for adaptive, mechanism-aware defect detection and dataset augmentation. Nevertheless, their deployment in real-time monitoring remains challenging due to the need for rapid sensor feedback and computational overhead. Careful integration with physics-based models

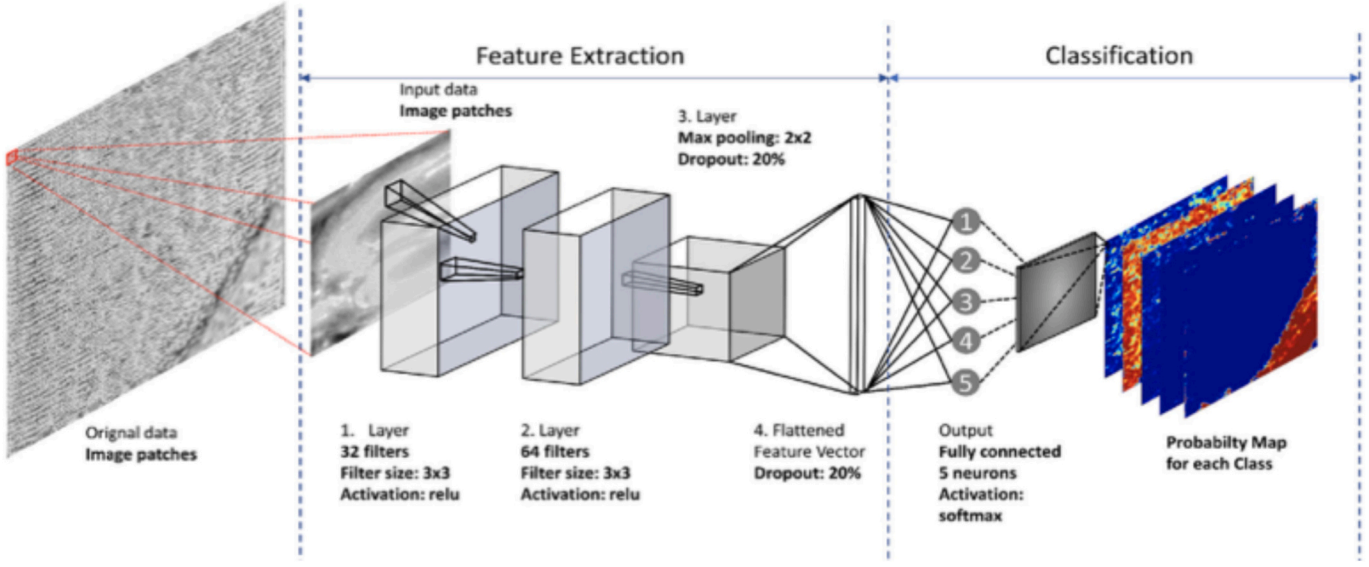



**Fig. 14.** The architecture of the proposed CNN model is used to predict surface roughness and defective areas [277].

can help address these limitations and enhance transferability across materials and machine platforms.

### 7.5. Physics-informed and hybrid simulation–machine learning approaches

Physics-informed machine learning (PIML) represents a transformative shift in defect detection for L-PBF and EB-PBF by moving beyond traditional "black-box" models. Standard data-driven approaches often rely on machine-specific settings like laser power and scan speed, which lack transferability between different manufacturing systems. By integrating physical laws and mechanistic modeling, PIML creates more interpretable and generalizable solutions for identifying critical defects such as porosity, balling, and lack of fusion.

The core methodology of these models involves converting raw machine settings into fundamental physical effects before they are processed by a learning algorithm. For instance, instead of using raw laser parameters directly, a physics-informed model interprets these inputs into physical machine-independent features such as laser energy density and radiation pressure. This approach ensures that the model focuses on the actual heat and thermal pressure histories that drive defect generation, rather than just statistical correlations [280].

In L-PBF applications, PIML has been successfully implemented to enhance real-time melt pool monitoring (MPM) through advanced generative models. These frameworks often utilize CNN Transformers and GANs to predict future melt pool behavior by incorporating spatial-temporal effects. By accounting for the thermal interactions between adjacent melt pools and local cooling fluctuations, these models can accurately predict geometry changes—such as area and length—that are pivotal in determining final part porosity [281].

The synergy between mechanistic modeling and machine learning also allows for the identification of hierarchical variable importance in defect formation. Mechanistic models can compute complex physical attributes, such as molten pool velocity fields and cooling rates, which are often difficult to measure experimentally. When these calculated variables are used as inputs for machine learning, they provide a quantitative formalism capable of predicting defects like balling or cracking before any physical printing occurs.

Ultimately, the primary advantage of physics-informed models lies in their ability to bridge the gap between idealized simulations and actual manufacturing behavior while reducing the need for costly trial-and-error experiments. By combining experimental data with the rigor of fluid dynamics and heat transfer principles, PIML offers a robust diagnostic tool for the additive manufacturing industry. These models not only improve prediction accuracy but also provide actionable knowledge for process optimization and feedback control [282].

### 7.6. Machine learning for defect detection in EB-PBF

Recent ML developments in EB-PBF open the path for advanced quality control and detection of defects approaches in this arena. In one prominent study, researchers investigated how changes in surface flatness can predict and discover certain surface qualities (such as uniform, uneven, and porous textures) linked to various types of internal defects. They used five machine learning algorithms to fine-tune the process parameters for EB-PBF with S30C alloy: logistic regression, SVM, DT, XGBoost, and naive Bayes. SVM proved to be an advantageous technique, allowing for the building of a process map that matched process windows to internal defect features. CFD modeling aided this method by replicating temperature fields, fluid flow, and melt pool shape,

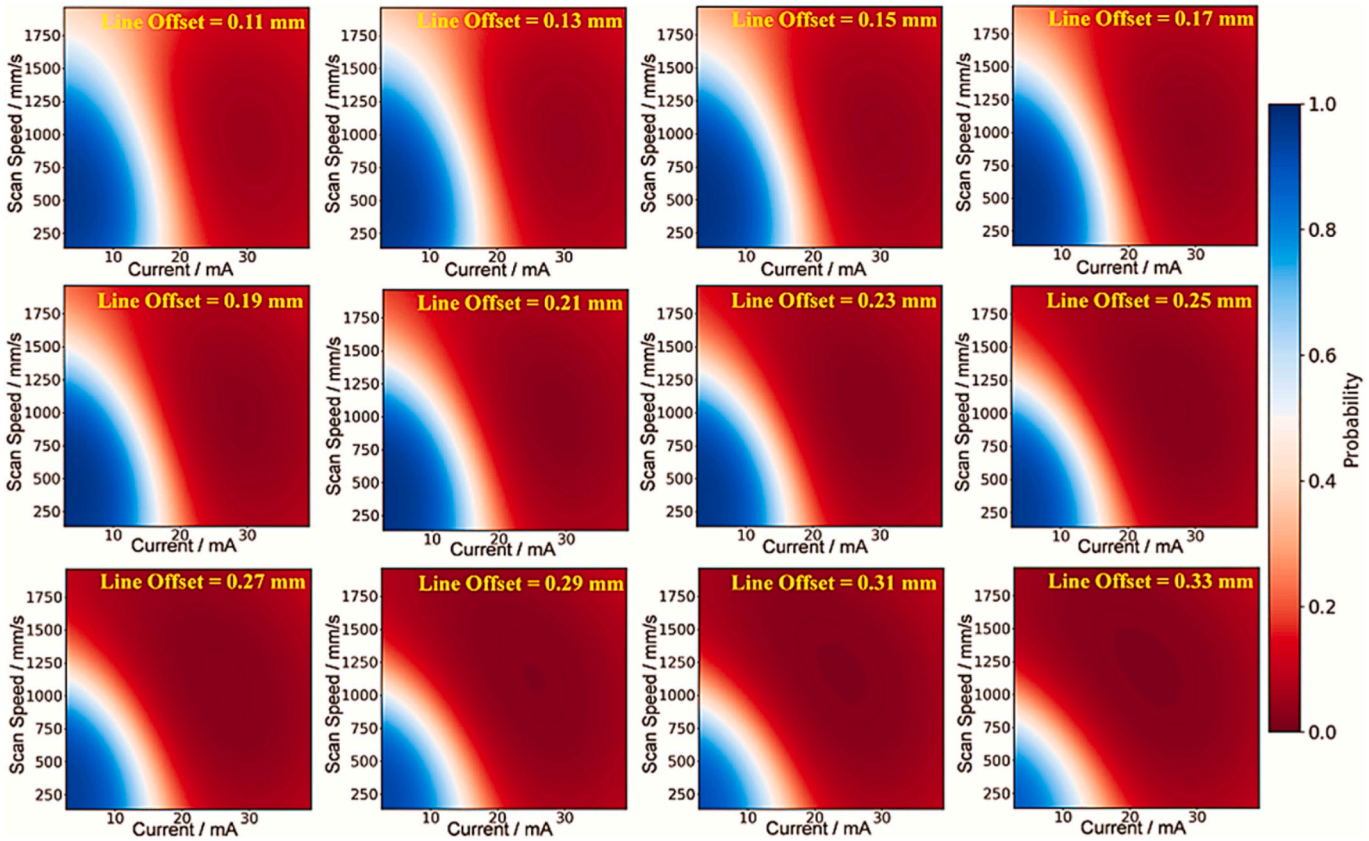



**Fig. 15.** Cross-sections of multidimensional process maps constructed using SVM as scan speed, current, and line offset functions. Dark blue (probability: 1.0) indicates that the surface morphology of the part printed by the processing parameters is predicted to be a good (even) surface without internal defects, and dark red (probability: 0.0) indicates a bad (uneven or porous) surface with internal defects [283]. (For interpretation of the references to color in this figure legend, the reader is referred to the web version of this article.)

separating high-quality constructs from ones with defects [283]. Fig. 15 shows the cross-sections of multidimensional process maps created with SVM as the scan speed, current, and line offset functions.

Another research investigated the automated classification of AM layer quality using deep learning, which was applied to electron-optical images collected during the EB-PBF procedure. The study employed many CNNs to achieve 95% classification accuracy by observing changes in surface topography and categorizing layers as usual, porous, or bulging using electron-optical images [284]. Finally, a different study combined neural networks with cascading 3D image processing and analysis algorithms to provide an early defect detection strategy for EB-PBF operations. The goal of this approach is to possibly solve the need for fault identification in industrial processes involving EB-PBF synthesis [285].

Table 3 presents ML approaches for defect detection in PBF, categorizing methods by learning type, algorithm (e.g., SVM, neural networks), PBF type (L-PBF, EB-PBF), and material (e.g., titanium, stainless steel). It highlights target defect types like porosity and LOF and specifies dataset sources, including real-time and experimental data, essential for accurate defect identification in AM.

### 7.7. Impact of data quality and quantity on ML performance

The performance of ML models in powder-based additive manufacturing is strongly dependent on the availability, quality, and consistency of data. Many studies rely on relatively small or heterogeneous datasets, which can limit the generalizability of trained models when applied to different alloys, machines, or geometries. This data scarcity remains a fundamental challenge, particularly in EB-PBF, where fewer studies and less publicly available datasets exist compared to L-PBF [233]. Variability in data acquisition protocols further complicates model development. Differences in imaging modalities (e.g., optical, infrared, X-ray), sensor settings, environmental conditions, and monitoring strategies introduce inconsistencies that can reduce model robustness and predictive accuracy. For example, even slight variations in camera calibration, frame rate, or lighting conditions can significantly affect the features extracted for defect classification, posing challenges for reproducibility across laboratories and industrial setups. Another critical challenge is the absence of standardized datasets for ML in PBF. Currently, no widely adopted benchmarks exist that would enable direct comparison of ML methods or facilitate transfer learning across different systems. The lack of standardized, high-quality datasets prevents rigorous quantitative evaluation of model performance and hinders the establishment of universally applicable best practices [271,286].

Addressing these challenges requires careful dataset curation, preprocessing, and feature engineering to ensure that models capture meaningful process–structure–property relationships rather than dataset-specific artifacts. Furthermore, the development of open-access repositories, shared experimental protocols, and collaborative data-sharing frameworks is essential for accelerating progress, enabling reproducibility, and fostering industrial adoption of ML-driven defect detection in PBF [287]. In summary, while ML holds great promise for predictive process control and defect detection, its effectiveness is fundamentally constrained by data availability, variability, and standardization. Future research must focus not only on algorithmic advances but also on creating robust, high-quality datasets to ensure reliable and transferable ML applications in metal additive manufacturing.

## 8. Challenges and future directions

Although PBF has witnessed remarkable development, outstanding challenges must be addressed when fabricating defect-free, high-performance components. Mastering these challenges is becoming crucial for the mechanical reliability, process scalability, and cost-efficiency of PBF as industries increasingly turn toward the technology for mission-critical applications.

A key challenge involves attaining real-time process monitoring and implementing closed-loop control. Current PBF systems primarily function under open-loop conditions, with predetermined process parameters that do not adjust to dynamic changes in powder spreading, laser–powder interaction, or melt-pool stability. As a result, defects, including LoF or porosity, may develop undetected during the fabrication process. The forthcoming generation of systems should integrate multi-sensor data, including optical, infrared, acoustic, and tomographic signals, with advanced algorithms designed to detect variations in real-time. Integrating real-time analysis within the machine, facilitated by edge computing and high-speed data processing, enables automatic parameter correction during the build process. The shift from reactive to self-corrective manufacturing signifies a crucial advancement in attaining reliable PBF.

At the same time, a growing consensus exists that data-driven ML approaches, despite their effectiveness, frequently function as black boxes with restricted physical interpretability. The future involves the integration of physics-based models with ML to create hybrid, mechanism-aware predictive frameworks. PINNs integrate governing equations, including heat conduction, mass conservation, and fluid flow, into their architecture. This integration diminishes reliance on extensive labeled datasets and enhances generalization across various materials and geometries. Combining FE or CFD simulations with ML facilitates the development of models that predict defect occurrence and elucidate the underlying physical mechanisms. Hybrid approaches offer solutions for process optimization and control that are interpretable, computationally efficient, and transferable.

However, the success of any data-driven framework relies on the quality, diversity, and accessibility of data. Most studies still depend on small or heterogeneous datasets collected under different experimental conditions, leading to poor generalization of trained models. The community urgently needs standardized, large-scale repositories that link process parameters, in-situ sensor outputs, and ex-situ characterization data. Collaborative data-sharing initiatives and federated learning frameworks could enable the creation of secure, open datasets while preserving proprietary information. Alongside this, consistent benchmarking protocols are necessary to evaluate ML algorithms objectively across materials, machines, and defect types. Establishing such a data infrastructure is a prerequisite for reliable and reproducible defect prediction in AM.

Beyond digital advancements, the quality and consistency of powder feedstock are essential physical challenges that directly impact defect formation. Differences in particle size distribution, morphology, and surface chemistry influence flowability, energy absorption, and melting uniformity, resulting in variable porosity or incomplete fusion. Repeated reuse of powder may lead to oxidation, contamination, and alterations in composition, which can compromise the integrity of the part. Future research should concentrate on real-time monitoring of powder quality through inline optical or hyperspectral sensing, in conjunction with enhanced recycling protocols and predictive models for powder aging. The development of novel alloy systems specifically designed for powder bed fusion, including high-entropy and functionally graded materials with enhanced thermal stability, presents an opportunity to minimize defect sensitivity from the initial stages of material design.

Ultimately, the path forward lies in convergence. Progress in PBF will emerge from the integration of sensing technologies, multi-physics modeling, ML, and material science into intelligent systems capable of detecting, understanding, and preventing defects before they occur. Establishing strong connections between experimental observation, physical modeling, and data-driven prediction will enable adaptive control strategies that ensure process stability and part reliability. Through this synergistic approach, PBF can evolve from a trial-and-error fabrication method into a self-optimizing, mechanism-aware manufacturing process—paving the way for the reliable production of mission-critical components for extreme environments.

**Table 3**
Different ML methods used in PBF.

| ML category | ML Algorithm | AM method | Material type | Defect type | Dataset type | Ref |
|---|---|---|---|---|---|---|
| Statistical | Response surface method | pulsed-L-PBF | 316L stainless steel | Relative density | Process parameters | [227] |
| Statistical | Spatial Gaussian process regression | L-PBF | 17–4 PH stainless steel | Porosity | Speed and power | [228] |
| Statistical | Multi-gene genetic programming | SLS | Hydroxyapatite (HA)-polyamide (PA) composites | Porosity, shrinkage, strength, density | Process parameters | [229] |
| Statistical | Generalized Linear Model and ANOVA | EB-PBF | AISI H13 | Internal porosity and surface topography correlation | Data obtained from Image | [230] |
| Statistical | Analytical methods | L-PBF | 316L stainless steel | Failure modes classification | Acoustic emission signal | [256] |
| Supervised ML | Convolutional Neural Network | L-PBF | 316L stainless steel | Quality analysis | Off-axial in-situ monitoring system equipped with three types of sensors | [231] |
| Supervised ML | Hybrid deep generative prediction network | L-PBF | 316L stainless steel | Pore morphology prediction | High-dimensional images | [232] |
| Supervised ML | Deep Neural Networks | L-PBF | CAD files | Detection of layerwise flaws and variant geometry in each layer | DSLR camera | [233] |
| Supervised ML | Convolutional Neural Network | L-PBF | AlSi10Mg, bronze, Inconel 625, Inconel 718, stainless steel 316L, stainless steel 17–4 PH, and Ti-6Al-4V | Classification anomalies (Hopping, streaking, debris, part damage) | Stock powder bed camera and lighting configuration | [234] |
| Supervised ML | Convolutional Neural Network | not said | Metallography dataset from additive manufacturing of steels (Metal DAM) | Detection of microstructural | Metallographic | [240] |
| Supervised ML | Convolutional Neural Network | L-PBF | Ti6-Al-4V, 316L stainless steel | Defect classification | Off-axis CMOS camera monitoring | [241] |
| Supervised ML | Convolutional Neural Network | L-PBF | AlSi10Mg metal | Classification | EOSTATE monitoring | [242] |
| Supervised ML | KM, SVM, Neural network | L-PBF | Synthetic functional dataset | Defect classification | Video-imaging data (in-situ high-speed cameras) | [243] |
| Supervised ML | Bayesian classifier | L-PBF | Inconel 625 | Defective or non-defective | Digital Camera | [244] |
| Supervised ML | SVM and RBF neural network | L-PBF | AlSi12 | Slag inclusion defect classification | Molten pool image (CCD Camera) | [245] |
| Supervised ML | Deep learning | L-PBF | Stainless steel, titanium alloys, and aluminum alloys | Defect detection | Optical microscopy images | [246] |
| Supervised ML | Artificial neural network, support vector machine, and deep belief network | L-PBF | 316L stainless steel | Porosity classification | Melt pool images (coaxial high-speed in situ monitoring) | [247] |
| Supervised ML | Convolutional Neural Network | L-PBF | Hastelloy X | Porosity classification(KH-induced porosity, LOF, residual porosity) | EOSTATE monitoring | [248] |
| Supervised ML | Logistic regression | L-PBF | 316L stainless steel | Defect detection | Fiber-coupled InGaAs-based infrared pyrometer and Si-based photodiode | [251] |
| Supervised ML | Convolutional Neural Network | L-PBF | Haynes282 (nickel-based superalloy) | Discrete sub-volumes detection | Short-wave infrared thermography | [252] |
| Supervised ML | Deep Neural Networks | L-PBF | H13 | Print defect detection | Thermographic off-axis imaging | [253] |
| Supervised ML | Support Vector Machine | L-PBF | 304L stainless steel | Defect classification (overheating, normal, and underheating) | Acoustic emission signal | [288] |
| Supervised ML | Logistic regression, SVCM random forest, Gaussian process | L-PBF | Al92Mn6Ce2 | Crack detection | Acoustic emission signal | [255] |
| Supervised ML | Artificial Neural Network | L-PBF | CL20ES stainless steel | Low, medium, and high quality | Acoustic Emission Spectroscopy | [49] |
| Supervised ML | Linear regression, Random forest, GPR | L-PBF | Ti64 | Defect classification | LR-XCT | [257] |
| Supervised ML | Bayes classifier | L-PBF | 316L stainless steel, a cobalt-chrome alloy, and Ti6AI4V titanium | Defect classification | X-ray computed tomography | [258] |
| Supervised ML | k-Nearest neighbors and decision trees | L-PBF | Nickel alloys (CM247LC, LR8 and Alloy 713C.) | Defect classification | X-ray computed tomography | [259] |
| Supervised ML | Neural Network | L-PBF | AlSi10Mg | Defect classification | X-ray micro-computed tomography | [260] |
| Supervised ML | Neural network, Decision tree | L-PBF | Ti-6Al-4V | Defect classification | High-resolution X-ray computed tomography | [48] |
| Supervised ML | CNN | L-PBF | A20X powder | Classification(Porosity, non-porosity) | CAD file and XCT scan data | [261] |
| Supervised ML | DBN | L-PBF | 304 stainless steel | Defect detection | Acoustic emission signal | [87] |
| Supervised ML | Logistic regression, support vector machine, decision tree, XGBoost, and naive Bayes | EB-PBF | S30C alloy | Classification (even, uneven, and porous) | SEM and X-ray CT | [283] |

(*continued on next page*)

**Table 3** (*continued*)

| ML category | ML Algorithm | AM method | Material type | Defect type | Dataset type | Ref |
|---|---|---|---|---|---|---|
| Supervised ML | Convolutional Neural Network | EB-PBF | Ti-6Al-4V | Classify the quality | Electron-optical images | [284] |
| Supervised ML | Convolutional Neural Network | EB-PBF | Ti-6Al-4V | Quality classification (defective, non-defective) | Video camera | [285] |
| Unsupervised ML | k-Means clustering | L-PBF | Ti-6Al–4V (four powder types), AlSi10Mg, Inconel 718 (two powder types), stainless steel 316L, stainless steel 17–4, and a bronze alloy. | Classification of six types of faults | Camera EOS M290 | [262] |
| Unsupervised ML | k-Means clustering | L-PBF | AISI 316L | Detection and the spatial localization of local defects | Camera CMOS | [263] |
| Unsupervised ML | k-Means clustering | L-PBF | Zinc Powders | – | IR images | [264] |
| Unsupervised ML | Self-Organizing Map (SOM) | L-PBF | Hastelloy-X [EOS Nickel Alloy HX] | Detection of defects (LOF) | CT scanning | [266] |
| Unsupervised ML | k-Means clustering | L-PBF | Ti-6Al-4V, Inconel 718, Ti-5553 and Haynes 282 | – | X-ray Computed Tomography | [267] |
| Unsupervised ML | SVM + DBSCAN | L-PBF | Ti6Al4V | Defect detection and characterization | CT | [268] |
| Semi-Supervised Ml | CNN | L-PBF | 316L stainless steel | Track average width, track continuity | In-situ videos | [249] |
| Semi-Supervised Ml | GMM | L-PBF | Inconel 718 | Faulty or acceptable classification | Photodiode data | [269] |
| Semi-Supervised Ml | KNN and k-means clustering | L-PBF | AISilOMg | Classification (“Drift” or “No-drift”) | Computer tomography | [270] |
| Semi-Supervised Ml | Deep learning models | L-PBF | 316L stainless steel | Classify surface appearances | Optical in-situ monitoring data | [272] |
| Semi-Supervised Ml | Deep learning models | L-PBF | 316L stainless steel | Classify surface appearances | Digital camera | [274] |
| Reinforcement Learning | – | L-PBF | 316L stainless steel | Classification (poor, medium and high quality). | Acoustic emission signal | [275] |
| Reinforcement Learning | Constrained Markov decision process (CMDP) | L-PBF | – | Predict the stochastic evolving dynamics of defect states | X-ray computed tomography (XCT) and scanning optical microscopy | [276] |
| Reinforcement Learning | – | L-PBF | – | Spatially resolved and layer-wise prediction of the surface roughness | High dynamic range (HDR) optical imaging | [277] |

## 9. Conclusion

This review has presented an integrated assessment of defect formation, detection, and characterization in PBF additive manufacturing, with particular emphasis on LPBF. The discussion systematically connected the physical origins of common defects with the sensing modalities, data-driven methods, and numerical models used to identify and analyze them. By organizing the literature around defect mechanisms rather than individual techniques, this work clarifies how process instabilities manifest as measurable signatures during fabrication.

A critical evaluation of in-situ and ex-situ sensing technologies showed how optical, infrared, thermographic, acoustic, and tomographic methods provide complementary information on melt-pool dynamics, thermal history, subsurface porosity, and geometric deviations. While each technique has inherent limitations, their combined use enables a more complete representation of the process state and improves the reliability of defect detection in PBF systems.

The role of ML in transforming sensor data into process-relevant information was examined across supervised, unsupervised, semi-supervised, and reinforcement learning approaches. Although these methods demonstrate strong capability for defect classification and quality prediction, the review highlighted the importance of integrating physical understanding to enhance interpretability and generalization. In this context, multiscale numerical modeling, spanning thermal, melt-pool, microstructural, and residual-stress simulations was shown to provide both mechanistic insight and physically meaningful descriptors that can be linked to sensing data and ML models.

Overall, this review offers a unified perspective that explicitly links defect mechanisms, sensing technologies, ML approaches, and multi-scale modeling within a single framework. By synthesizing these traditionally separate research streams, the work provides a consolidated reference for improving reliability, consistency, and qualification readiness in PBF processes, supporting the advancement of high-reliability additive manufacturing for mission-critical applications.

## CRediT authorship contribution statement

**Mohammad Taghian:** Writing – original draft, Visualization, Investigation, Formal analysis, Data curation. **Ali Pilehvar Meibody:** Writing – original draft, Visualization, Software, Methodology, Investigation, Formal analysis, Data curation. **Abdollah Saboori:** Writing – review & editing, Validation, Supervision, Resources, Project administration, Conceptualization. **Luca Iuliano:** Writing – review & editing, Validation, Supervision, Resources.

## Declaration of competing interest

The authors declare that they have no known competing financial interests or personal relationships that could have appeared to influence the work reported in this paper.

## References

[1] Shamsaei N, Yadollahi A, Bian L, Thompson SM. An overview of Direct Laser Deposition for additive manufacturing; part II: mechanical behavior, process parameter optimization and control. Addit Manuf 2015;8:12–35. https://doi.org/10.1016/j.addma.2015.07.002.

[2] Aiza I, Baldi C, de la Vega FM, Sebastiani S, Veronese NE, Yousefi M, et al. Effects of build orientation and inclined features on physical, microstructural and mechanical properties of powder bed fusion additively manufactured metallic parts. Prog Mater Sci 2025;147:101357. https://doi.org/10.1016/j.pmatsci.2024.101357.

[3] Sanaei N, Fatemi A. Defects in additive manufactured metals and their effect on fatigue performance: a state-of-the-art review. Prog Mater Sci 2021;117:100724. https://doi.org/10.1016/j.pmatsci.2020.100724.
[4] Dadkhah M, Tulliani J-M, Saboori A, Iuliano L. Additive manufacturing of ceramics: advances, challenges, and outlook. J Eur Ceram Soc 2023;43:6635–64. https://doi.org/10.1016/j.jeurceramsoc.2023.07.033.
[5] Oliveira JP, LaLonde AD, Ma J. Processing parameters in laser powder bed fusion metal additive manufacturing. Mater. Des. 2020;193:108762.
[6] Ghanavati R, Lannunziata E, Norouzi E, Bagherifard S, Iuliano L, Saboori A. Design and development of SS316L-IN718 functionally graded materials via laser powder bed fusion. Mater Lett 2023;349:134793. https://doi.org/10.1016/j.matlet.2023.134793.
[7] DebRoy T, Wei HL, Zuback JS, Mukherjee T, Elmer JW, Milewski JO, et al. Additive manufacturing of metallic components – process, structure and properties. Prog Mater Sci 2018;92:112–224. https://doi.org/10.1016/j.pmatsci.2017.10.001.
[8] Saboori A, Biamino S, Lombardi M, Tusacciu S, Busatto M, Lai M, et al. How the nozzle position affects the geometry of the melt pool in directed energy deposition process. Powder Metall 2019;62:213–7. https://doi.org/10.1080/00325899.2019.1627490.
[9] Snow Z, Nassar AR, Reutzel EW. Invited review article: review of the formation and impact of flaws in powder bed fusion additive manufacturing. Addit. Manuf. 2020;36:101457.
[10] Saboori A, Aversa A, Marchese G, Biamino S, Lombardi M, Fino P. Application of directed energy deposition-based additive manufacturing in repair. Appl. Sci. 2019;9. https://doi.org/10.3390/app9163316.
[11] Ye C, Zhang C, Zhao J, Dong Y. Effects of post-processing on the surface finish, porosity, residual stresses, and fatigue performance of additive manufactured metals: a review. J Mater Eng Perform 2021;30:6407–25. https://doi.org/10.1007/s11665-021-06021-7.
[12] Davoodi F, Taghian M, Carbone G, Saboori A, Iuliano L. An overview of the latest progress in internal surface finishing of the additively manufactured metallic components. Materials (Basel) 2023;16. https://doi.org/10.3390/ma16103867.
[13] Mutiargo B, Pavlović M, Malcolm AA, Goh BH, Krishnan M, Shota T, et al. Evaluation of x-ray computed tomography (CT) images of additively manufactured components using deep learning. 2020.
[14] Taghian M, Mosallanejad MH, Lannunziata E, Del Greco G, Iuliano L, Saboori A. Laser powder bed fusion of metallic components: latest progress in productivity, quality, and cost perspectives. J Mater Res Technol 2023;27:6484–500. https://doi.org/10.1016/j.jmrt.2023.11.049.
[15] Mosallanejad MH, Ghanavati R, Behjat A, Taghian M, Saboori A, Iuliano L. Untapped opportunities in additive manufacturing with metals: from new and graded materials to post-processing. Metals (Basel) 2024;14:425. https://doi.org/10.3390/met14040425.
[16] Moheimani SK, Iuliano L, Saboori A. The role of substrate preheating on the microstructure, roughness, and mechanical performance of AISI 316L produced by directed energy deposition additive manufacturing. Int J Adv Manuf Technol 2022. https://doi.org/10.1007/s00170-021-08564-4.
[17] Mosallanejad MH, Abdi A, Karpasand F, Nassiri N, Iuliano L, Saboori A. Additive manufacturing of titanium alloys: processability, properties, and applications. Adv Eng Mater 2023;25(24):2301122.
[18] Bandekhoda MR, Mosallanejad MH, Atapour M, Iuliano L, Saboori A. Investigation on the potential of laser and electron beam additively manufactured Ti–6Al–4V components for orthopedic applications. Met Mater Int 2023. https://doi.org/10.1007/s12540-023-01496-6.
[19] Behjat A, Shamanian M, Taherizadeh A, Lannunziata E, Bagherifard S, Gadalińska E, et al. Microstructure-electrochemical behavior relationship in post processed AISI316L stainless steel parts fabricated by laser powder bed fusion. J Mater Res Technol 2023;23:3294–311. https://doi.org/10.1016/j.jmrt.2023.01.229.
[20] Shrestha S, Chou K. Formation of keyhole and lack of fusion pores during the laser powder bed fusion process. Manuf. Lett. 2022;32:19–23.
[21] Esmaeilizadeh R, Keshavarzkermani A, Ali U, Mahmoodkhani Y, Behravesh B, Jahed H, et al. Customizing mechanical properties of additively manufactured Hastelloy X parts by adjusting laser scanning speed. J Alloys Compd 2020;812:152097.
[22] Liang H, Xie D, Mao Y, Shi J, Wang C, Shen L, et al. The size effect on forming quality of Ti–6Al–4V solid struts fabricated via laser powder bed fusion. Metals (Basel) 2019;9(4):416.
[23] Mosallanejad MH, Gashmard H, Javanbakht M, Niroumand B, Saboori A. A novel feature engineering approach for predicting melt pool depth during LPBF by machine learning models. Addit Manuf Lett 2024;10:100214. https://doi.org/10.1016/j.addlet.2024.100214.
[24] Guo W, Feng B, Yang Y-G, Ren Y, Liu Y, Yang H, et al. Effect of laser scanning speed on the microstructure, phase transformation and mechanical property of NiTi alloys fabricated by LPBF. Mater. Des. 2022;215:110460.
[25] Mao Y, Gao Y, Hu J, Shen X, Zhou H. Effect of hatch spacing on the quality of Inconel 718 alloy part. Materials (Basel) 2024;17.
[26] Gunnerek R, Chen Z, Hryha E. Impact of high-productivity process parameters in powder bed fusion – laser beam on microstructure of stainless steel 316L. Eur J Mater 2023;3.
[27] Zhang L, Liu Y, Li S, Hao Y. Additive manufacturing of titanium alloys by electron beam melting: a review. Adv Eng Mater 2018;20:1700842.
[28] Mosallanejad MH, Niroumand B, Ghibaudo C, Biamino S, Salmi A, Fino P, et al. In-situ alloying of a fine grained fully equiaxed Ti-based alloy via electron beam powder bed fusion additive manufacturing process. Addit Manuf 2022;56:102878. https://doi.org/10.1016/j.addma.2022.102878.
[29] Taminger KMB, Hafley RA. Electron beam freeform fabrication: a rapid metal deposition process. 2003.
[30] Gong H, Rafi K, Gu H, Starr T, Stucker B. Analysis of defect generation in Ti-6Al-4V parts made using powder bed fusion additive manufacturing processes. Addit Manuf 2014;1. https://doi.org/10.1016/j.addma.2014.08.002.
[31] Gong X, Anderson T, Chou K. Review on powder-based electron beam additive manufacturing technology. Manuf Rev 2014;1:2.
[32] King WE, Anderson AT, Ferencz RM, Hodge NE, Kamath C, Khairallah SA, et al. Laser powder bed fusion additive manufacturing of metals; physics, computational, and materials challenges. Appl Phys Rev 2015;2. https://doi.org/10.1063/1.4937809.
[33] Huang Y, Fleming TG, Clark SJ, Marussi S, Fezzaa K, Thiyagalingam J, et al. Keyhole fluctuation and pore formation mechanisms during laser powder bed fusion additive manufacturing. Nat Commun 2021;13.
[34] Avegnon KLM, Menendez A, Liu J, Mittal YG, Karunakaran KP, Sealy MP. Patterned keyhole porosity formation in laser powder bed fusion caused by local disturbances in the shielding gas flow. Manuf. Lett. 2023;35:677–82.
[35] Wang J, Zhou XL, Li J, Brochu M, Zhao YF. Microstructures and properties of SLM-manufactured Cu-15Ni-8Sn alloy. Addit Manuf 2020;31. https://doi.org/10.1016/J.ADDMA.2019.100921.
[36] Snow Z, Scime L, Ziabari A, Fisher BA, Paquit VC. Observation of spatter-induced stochastic lack-of–fusion in laser powder bed fusion using in situ process monitoring. Addit Manuf 2023;61:103298.
[37] Hadibeyk S, Beidokhti B, Sajjadi SA. The effect of interlayer thickness, bonding temperature and atmosphere on transient liquid phase bonding of GTD-111 to FSX-414. J Mater Process Technol 2018;255:673–8. https://doi.org/10.1016/J.JMATPROTEC.2018.01.022.
[38] Everton SK, Hirsch M, Stravroulakis P, Leach RK, Clare AT. Review of in-situ process monitoring and in-situ metrology for metal additive manufacturing. Mater. Des. 2016;95:431–45.
[39] O'Donnell K, Quintana MJ, Collins PC. Understanding the effect of electron beam melting scanning strategies on the aluminum content and materials state of single Ti-6Al-4V feedstock. Materials (Basel) 2023;16.
[40] Flint TF, Anderson MJ, Akrivos V, Roy MJ, Francis JA, Vasileiou A, et al. A fundamental analysis of factors affecting chemical homogeneity in the laser powder bed fusion process. Int. J. Heat Mass Transf. 2022;194:122985.
[41] Panwisawas C, Tang YT, Ghoussoub JN, Reed RC. Additive manufacturability of nickel-based superalloys: composition-process induced vapourization. 2020.
[42] Saroukhani S, Warner DH. Investigating dislocation motion through a field of solutes with atomistic simulations and reaction rate theory. Acta Mater 2017;128:77–86. https://doi.org/10.1016/J.ACTAMAT.2017.02.001.
[43] Maleki E, Bagherifard S, Bandini M, Guagliano M. Surface post-treatments for metal additive manufacturing: progress, challenges, and opportunities. Addit Manuf 2021;37:101619. https://doi.org/10.1016/J.ADDMA.2020.101619.
[44] Kazemi Movahed A, Ghanavati R, Saboori A, Iuliano L. A review of strategies for in situ mitigating of residual stress in laser-based metal additive manufacturing: insights, innovations, and challenges. Acta Metall Sin English Lett 2025;38:1657–98. https://doi.org/10.1007/s40195-025-01902-5.
[45] Bartolomeu F, Costa MM, Gomes JR, Alves N, Abreu C, Silva F, et al. Implant surface design for improved implant stability–a study on Ti6Al4V dense and cellular structures produced by selective laser melting. Tribol Int 2019;129:272–82.
[46] Mercelis P, Kruth JP. Residual stresses in selective laser sintering and selective laser melting. Rapid Prototyp J 2006;12:254–65. https://doi.org/10.1108/13552540610707013.
[47] Dall'Ava L, Hothi H, Di Laura A, Henckel J, Hart A. 3D printed acetabular cups for total hip arthroplasty: a review article. Metals 2019;9:729. https://doi.org/10.3390/MET9070729.
[48] Poudel A, Yasin M, Ye J, Liu J, Vinel A, Shao S, et al. Feature-based volumetric defect classification in metal additive manufacturing. Nat Commun 2022;13:6369.
[49] Shevchik SA, Kenel C, Leinenbach C, Wasmer K. Acoustic emission for in situ quality monitoring in additive manufacturing using spectral convolutional neural networks. Addit Manuf 2018;21:598–604.
[50] Ji Z, Han Q. A novel image feature descriptor for SLM spattering pattern classification using a consumable camera. Int J Adv Manuf Technol 2020;110:2955–76. https://doi.org/10.1007/S00170-020-05995-3.
[51] Gunenthiram V, Peyre P, Schneider M, Dal M, Coste F, Koutiri I, et al. Experimental analysis of spatter generation and melt-pool behavior during the powder bed laser beam melting process. J Mater Process Technol 2018;251:376–86. https://doi.org/10.1016/J.JMATPROTEC.2017.08.012.
[52] Rodriguez E, Mireles J, Terrazas CA, Espalin D, Perez MA, Wicker RB. Approximation of absolute surface temperature measurements of powder bed fusion additive manufacturing technology using in situ infrared thermography. Addit Manuf 2015;5:31–9.
[53] Jalalahmadi B, Liu J, Rios J, Slotwinski J, Peitsch C, Goldberg A, et al. In-process defect monitoring and correction in additive manufacturing of aluminum alloys. In: Vert. flight soc. 75th annu. forum technol. display, Philadelphia, PA, USA; 2019.
[54] Bamberg J, Dusel KH, Satzger W. Overview of additive manufacturing activities at MTU aero engines. In: AIP conf. proc; 2015. p. 156–63.
[55] Binega E, Yang L, Sohn H, Cheng JCP. Online geometry monitoring during directed energy deposition additive manufacturing using laser line scanning. Precis Eng 2022;73:104–14.

[56] Fischer FG, Birk N, Rooney L, Jauer L, Schleifenbaum JH. Optical process monitoring in laser powder bed fusion using a recoater-based line camera. Addit Manuf 2021;47:102218.
[57] Liu Y, Guo L, Gao H, You Z, Ye Y, Zhang B. Machine vision based condition monitoring and fault diagnosis of machine tools using information from machined surface texture: a review. Mech Syst Signal Process 2022;164:108068.
[58] Liu R, Yang H. Multimodal probabilistic modeling of melt pool geometry variations in additive manufacturing. Addit Manuf 2023;61:103375.
[59] Perani M, Baraldo S, Decker M, Vandone A, Valente A, Paoli B. Track geometry prediction for laser metal deposition based on on-line artificial vision and deep neural networks. Robot Comput Integr Manuf 2023;79:102445.
[60] Lazaros N, Sirakoulis GC, Gasteratos A. Review of stereo vision algorithms: from software to hardware. In: Lazaros Taylor Fr, Sirakoulis GC, Gasteratos A, editors. International j. optomechatronics. vol. 2. Taylor Fr.; 2008. p. 435–62. https://doi.org/10.1080/15599610802438680.
[61] Kanko JA, Sibley AP, Fraser JM. In situ morphology-based defect detection of selective laser melting through inline coherent imaging. J Mater Process Technol 2016;231:488–500.
[62] Colosimo BM, Grasso M. Spatially weighted PCA for monitoring video image data with application to additive manufacturing. J Qual Technol 2018;50:391–417. https://doi.org/10.1080/00224065.2018.1507563.
[63] Craeghs T, Clijsters S, Yasa E, Kruth JP. Online quality control of selective laser melting. In: Int. solid free. fabr. symp; 2011.
[64] Wei J, He Y, Wang F, He Y, Rong X, Chen M, et al. Convolutional neural network assisted infrared imaging technology: an enhanced online processing state monitoring method for laser powder bed fusion. Infrared Phys Technol 2023;131:104661. https://doi.org/10.1016/j.infrared.2023.104661.
[65] Li Y, Xiao W, Xiao H, Liu X, He K, Xie P, et al. Enhanced molten-pool boundary stability for microstructure control using quasi-continuous-wave laser additive manufacturing. J Mater Res Technol 2023;23:238–44.
[66] Smurov I, Doubenskaia M. Temperature monitoring by optical methods in laser processing. In: Laser-assisted fabr. mater; 2012. p. 375–422.
[67] Dinwiddie RB, Dehoff RR, Lloyd PD, Lowe LE, Urlich JB. Thermographic in-situ process monitoring of the electron-beam melting technology used in additive manufacturing. In: Thermosense therm. infrared appl. XXXV; 2013.
[68] Kim S, Jeon I, Sohn H. Infrared thermographic imaging based real-time layer height estimation during directed energy deposition. Opt Lasers Eng 2023;168:107661.
[69] Kayacan MY, Yılmaz N. An investigation on the measurement of instantaneous temperatures in laser assisted additive manufacturing by thermal imagers. Measurement 2020;160:107825.
[70] Mazzoleni L, Demir AG, Caprio L, Pacher M, Previtali B. Real-time observation of melt pool in selective laser melting: spatial, temporal, and wavelength resolution criteria. IEEE Trans Instrum Meas 2020;69:1179–89.
[71] Raplee J, Plotkowski A, Kirka MM, Dinwiddie RB, Babu SS. Thermographic microstructure monitoring in electron beam additive manufacturing. Sci Rep 2017;7:43554.
[72] Heigel JC, Michaleris P, Reutzel EW. Thermo-mechanical model development and validation of directed energy deposition additive manufacturing of Ti–6Al–4V. Addit Manuf 2015;5:9–19.
[73] Zheng L, Zhang Q, Cao H, Wu W, Ma H, Ding X, et al. Melt pool boundary extraction and its width prediction from infrared images in selective laser melting. Mater. Des. 2019;183:108110.
[74] Demir AG, De Giorgi C, Previtali B. Design and implementation of a multisensor coaxial monitoring system with correction strategies for selective laser melting of a maraging steel. J Manuf Sci Eng 2018;140:041003.
[75] Mitchell JA, Ivanoff TA, Dagel D, Madison JD, Jared B. Linking pyrometry to porosity in additively manufactured metals. Addit Manuf 2020;31:100946.
[76] Schwerdtfeger J, Singer RF, Körner C. In situ flaw detection by IR-imaging during electron beam melting. Rapid Prototyp. J. 2012;18:259–63. https://doi.org/10.1108/13552541211231572/FULL/HTML.
[77] Chen Y, Jiang L, Peng Y, Wang M, Xue Z, Wu J, et al. Ultra-fast laser ultrasonic imaging method for online inspection of metal additive manufacturing. Opt Lasers Eng 2023;160:107244.
[78] Tempelman JR, Wachtor AJ, Flynn EB, Depond P, Forien J, Guss G, et al. Detection of keyhole pore formations in laser powder-bed fusion using acoustic process monitoring measurements. Addit Manuf 2022;55:102735.
[79] Tempelman JR, Wachtor AJ, Depond P, Forien JB, Guss G, Calta N, et al. Sensor fusion of pyrometry and acoustic measurements for localized keyhole pore identification in laser powder bed fusion. J Mater Process Technol 2022;308:117656.
[80] Segreto T, Bottillo A, Teti R. Advanced ultrasonic non-destructive evaluation for metrological analysis and quality assessment of impact damaged non-crimp fabric composites. Procedia CIRP 2016;41:1055–60.
[81] Dai T, Jia X-J, Zhang J, Wu J-F, Sun Y-W, Yuan S-X, et al. Laser ultrasonic testing for near-surface defects inspection of 316L stainless steel fabricated by laser powder bed fusion. China Foundry 2021;18:360–8. https://doi.org/10.1007/s41230-021-1063-1.
[82] Lv G, Yao Z, Chen D, Li Y, Cao H, Yin A, et al. Fast and high-resolution laser-ultrasonic imaging for visualizing subsurface defects in additive manufacturing components. Mater. Des. 2023;225:111454.
[83] Aleshin NP, Murashov VV, Shchipakov NA, Krasnov IS, Lozhkova DS. Experimental research into possibilities and peculiarities of ultrasonic testing of additive manufactured parts. Russ. J. Nondestruct. Test. 2016;52:17–24. https://doi.org/10.1134/S1061830916120020.
[84] Text OR, Popovich A, Masaylo DV, Sufiiarov Vs, Borisov E, Polozov I, et al. A laser ultrasonic technique for studying the properties of products manufactured by additive technologies. Russ J Nondestruct Test 2016;52:3–10. https://doi.org/10.1134/S1061830916060097.
[85] Rieder H, Dillhöfer A, Spies M, Bamberg J, Hess T. Online monitoring of additive manufacturing processes using ultrasound. In: Proc. 11th eur. conf. non-destructive test; 2014.
[86] Rieder H, Spies M, Bamberg J, Henkel B. On-and offline ultrasonic characterization of components built by SLM additive manufacturing. AIP Conf. Proc. 2016;1706:130002.
[87] Ye D, Hong GS, Zhang Y, Zhu K, Fuh JYH. Defect detection in selective laser melting technology by acoustic signals with deep belief networks. Int J Adv Manuf Technol 2018;96:2791–801. https://doi.org/10.1007/s00170-018-1728-0.
[88] Smith RJ, Hirsch M, Patel R, Li W, Clare AT, Sharples SD. Spatially resolved acoustic spectroscopy for selective laser melting. J Mater Process Technol 2016;236:93–102.
[89] Pieris D, Patel R, Dryburgh P, Hirsch M, Li W, Sharples SD, et al. Spatially resolved acoustic spectroscopy towards online inspection of additive manufacturing. Insight - Non-Destructive Test Cond Monit 2019;61:132–7.
[90] Liu T, Lough CS, Sehhat H, Ren YM, Christofides PD, Kinzel EC, et al. In-situ infrared thermographic inspection for local powder layer thickness measurement in laser powder bed fusion. Addit Manuf 2022;55:102873. https://doi.org/10.1016/j.addma.2022.102873.
[91] Zhao C, Fezzaa K, Cunningham RW, Wen H, De Carlo F, Chen L, et al. Real-time monitoring of laser powder bed fusion process using high-speed X-ray imaging and diffraction. Sci Rep 2017;7:3602.
[92] Zenzinger G, Bamberg J, Ladewig A, Henkel B, Satzger W. Process monitoring of additive manufacturing by using optical tomography. AIP Conf Proc 2014;1650:164–70. https://doi.org/10.1063/1.4914606.
[93] Du Plessis A, Tshibalanganda M, Le Roux SG. Not all scans are equal: X-ray tomography image quality evaluation. Mater Today Commun 2020;22:100792.
[94] Townsend A, Pagani L, Scott P, Blunt L. Areal surface texture data extraction from X-ray computed tomography reconstructions of metal additively manufactured parts. Precis Eng 2017;48:254–64.
[95] Du Plessis A, Yadroitsev I, Le Roux S. X-ray microcomputed tomography in additive manufacturing: a review of the current technology and applications. 3D Print Addit Manuf 2018;5.
[96] Neef A, Seyda V, Herzog D, Emmelmann C, Schönleber M, Kogel-Hollacher M. Low coherence interferometry in selective laser melting. Phys Procedia 2014;56:82–9.
[97] Senin N, Thompson A, Leach RK. Characterisation of the topography of metal additive surface features with different measurement technologies. Meas Sci Technol 2017;28.
[98] Karagadde S, Leung CL, Lee PD. Progress on in situ and operando X-ray imaging of solidification processes. Materials (Basel) 2021;14. https://doi.org/10.3390/ma14092374.
[99] Suresh V, Balasubramaniam B, Yeh L-H, Li B. Recent advances in in situ 3D surface topographical monitoring for additive manufacturing processes. J. Manuf. Mater. Process 2025;9. https://doi.org/10.3390/jmmp9040133.
[100] Schoinochoritis B, Chantzis D, Salonitis K. Simulation of metallic powder bed additive manufacturing processes with the finite element method: a critical review. Proc Inst Mech Eng Part B J Eng Manuf 2017;231:96–117. https://doi.org/10.1177/0954405414567522.
[101] Mindt HW, Desmaison O, Megahed M, Peralta A, Neumann J. Modeling of powder bed manufacturing defects. J. Mater. Eng. Perform. 2018;27:32–43.
[102] N'Dri N, Mindt HW, Shula B, Megahed M, Peralta A, Kantzos P, et al. DMLS process modelling and validation. In: TMS 2015 144 th annu. meet. exhib. suppl. proc; 2015. p. 389–96.
[103] Vogel M, Khan M, Ibara-Medina J, Pinkerton A, N'Dri N, Megahed M. A coupled approach to weld pool, phase and residual stress modelling of laser direct metal deposition (LDMD) processes. In: Proc. 2nd world congr. integr. comput. mater. eng; 2013. p. 231–6. https://doi.org/10.1007/978-3-319-48194-4_37.
[104] Goldak JA, Akhlaghi M. Computational welding mechanics. 2005.
[105] Fu CH, Guo YB, Sealy MP. A predictive model and validation of laser cutting of nitinol with a novel moving volumetric pulsed heat flux. J Mater Process Technol 2014;214:2926–34.
[106] Li C, Fu CH, Guo YB, Fang FZ. Fast prediction and validation of part distortion in selective laser melting. Procedia Manuf 2015;1:355–65.
[107] Hodge NE, Ferencz RM, Solberg JM. Implementation of a thermomechanical model for the simulation of selective laser melting. Comput Mech 2014;54:33–51. https://doi.org/10.1007/S00466-014-1024-2.
[108] Markl M, Ammer R, Ljungblad U, Rüde U, Körner C. Electron beam absorption algorithms for electron beam melting processes simulated by a three-dimensional thermal free surface lattice Boltzmann method in a distributed and parallel environment. Procedia Comput Sci 2013;18:2127–36.
[109] Mcvey RW, Melnychuk RM, Todd JA, Martukanitz RP. Absorption of laser irradiation in a porous powder layer. J Laser Appl 2007;19:214–24. https://doi.org/10.2351/1.2756854.
[110] Zhou J, Zhang Y, Chen JK. Numerical simulation of laser irradiation to a randomly packed bimodal powder bed. Int. J. Heat Mass Transf. 2009;52:3137–46.
[111] Safdar S, Li L, Sheikh MA. Numerical analysis of the effects of non-conventional laser beam geometries during laser melting of metallic materials. J Phys D Appl Phys 2007;40:593.

[112] Yao XX, Zhang Z. Laser-particle interaction-based heat source model of laser powder bed fusion additive manufacturing. Opt. Laser Technol. 2022;155: 108402. https://doi.org/10.1016/j.optlastec.2022.108402.
[113] Yan W, Smith J, Ge W, Lin F, Liu WK. Multiscale modeling of electron beam and substrate interaction: a new heat source model. Comput. Mech. 2015;56:265–76. https://doi.org/10.1007/s00466-015-1170-1.
[114] Kusano M, Watanabe M. Heat source model development for thermal analysis of laser powder bed fusion using Bayesian optimization and machine learning. Integr Mater Manuf Innov 2024;13:288–304. https://doi.org/10.1007/s40192-023-00334-2.
[115] Trapp J, Rubenchik AM, Guss G, Matthews MJ. In situ absorptivity measurements of metallic powders during laser powder-bed fusion additive manufacturing. Appl Mater Today 2017;9:341–9. https://doi.org/10.1016/j.apmt.2017.08.006.
[116] Zeng K, Pal D, Stucker B. A review of thermal analysis methods in laser sintering and selective laser melting. 2012.
[117] Cheng B, Price S, Lydon J, Cooper K, Chou K. On process temperature in powder-bed electron beam additive manufacturing: model development and validation. J Manuf Sci Eng 2014;136:061018.
[118] Chen T, Zhang Y. Numerical simulation of two-dimensional melting and resolidification of a two-component metal powder layer in selective laser sintering process. Numer Heat Transf Part A Appl 2010;46:633–49. https://doi.org/10.1080/104077890504177.
[119] Körner C, Helmer H, Bauereiß A, Singer RF. Tailoring the grain structure of IN718 during selective electron beam melting. In: EUROSUPERALLOYS 2014 – 2nd Eur. symp. superalloys their appl. vol. 14; 2014. p. 8001. https://doi.org/10.1051/matecconf/20141408001.
[120] Ransenigo C, Tocci M, Palo F, Ginestra P, Ceretti E, Gelfi M, et al. Evolution of melt pool and porosity during laser powder bed fusion of Ti6Al4V alloy: numerical modelling and experimental validation. Lasers Manuf Mater Process 2022;9:481–502. https://doi.org/10.1007/s40516-022-00185-3.
[121] Philo AM, Butcher D, Sillars S, Sutcliffe CJ, Sienz J, Brown SGR, et al. A multiphase CFD model for the prediction of particulate accumulation in a laser powder bed fusion process. In: Nastac L, Pericleous K, Sabau AS, Zhang L, Thomas BG, editors. CFD model. simul. mater. process. 2018. Cham: Springer International Publishing; 2018. p. 65–76.
[122] Shrestha S, Kevin Chou Y. A numerical study on the keyhole formation during laser powder bed fusion process. J Manuf Sci Eng 2019;141:101002. https://doi.org/10.1115/1.4044100.
[123] De Leon E, Riensche A, Bevans BD, Billings C, Siddique Z, Liu Y. A review of modeling, simulation, and process qualification of additively manufactured metal components via the laser powder bed fusion method. J Manuf Mater Process 2025;9. https://doi.org/10.3390/jmmp9010022.
[124] Todhunter LD, Leach RK, Lawes SDA, Blateyron F. Industrial survey of ISO surface texture parameters. CIRP J. Manuf. Sci. Technol. 2017;19:84–92.
[125] Wei PS. Thermal science of weld bead defects: a review. Artic J Heat Transf 2011. https://doi.org/10.1115/1.4002445.
[126] Helmer H, Bauereiß A, Singer RF, Körner C. Grain structure evolution in Inconel 718 during selective electron beam melting. Mater Sci Eng A 2016;668:180–7.
[127] King W, Anderson AT, Ferencz RM, Hodge NE, Kamath C, Khairallah SA. Overview of modelling and simulation of metal powder bed fusion process at Lawrence Livermore National Laboratory. Mater Sci Technol 2015;31:957–68. https://doi.org/10.1179/1743284714Y.0000000728.
[128] Markl M, Körner C. Multiscale modeling of powder bed–based additive manufacturing. Annu Rev Mat Res 2016;46:93–123. https://doi.org/10.1146/annurev-matsci-070115-032158.
[129] Moser D, Cullinan M, Murthy J. Particle-scale melt modeling of the selective laser melting process. In: Olid free. fabr. 2016 proc. 27th annu. int; 2016.
[130] Panwisawas C, Sovani Y, Anderson M, Turner R, Palumbo N, Saunders BC, et al. A multi-scale multi-physics approach to modelling of additive manufacturing in nickel-based superalloys. In: Nickel-based superalloys; 2016. p. 1021–30.
[131] Fu CH, Guo YB. Three-dimensional temperature gradient mechanism in selective laser melting of Ti-6Al-4V. J Manuf Sci Eng 2014;136:061004.
[132] Cheng B, Chou K. Melt pool evolution study in selective laser melting. In: 26th annu. int. solid free. fabr. symp. - an addit. manuf. conf. Austin, TX, USA; 2015.
[133] Jamshidinia M, Kong F, Kovacevic R. Numerical modeling of heat distribution in the electron beam melting® of Ti-6Al-4V. J Manuf Sci Eng 2013;135:061010.
[134] Repossini G, Laguzza V, Grasso M, Colosimo BM. On the use of spatter signature for in-situ monitoring of laser powder bed fusion. Addit Manuf 2017;16:35–48.
[135] Scharowsky T, Osmanlic F, Singer RF, Körner C. Melt pool dynamics during selective electron beam melting. Appl. Phys. A Mater. Sci. Process. 2014;114: 1303–7. https://doi.org/10.1007/S00339-013-7944-4.
[136] Teng C, Gong H, Szabo A, Dilip J, Ashby K, Zhang S, et al. Simulating melt pool shape and lack of fusion porosity for selective laser melting of cobalt chromium components. J Manuf Sci Eng 2017;139:011009.
[137] Lee YS, Zhang W. Modeling of heat transfer, fluid flow and solidification microstructure of nickel-base superalloy fabricated by laser powder bed fusion. Addit Manuf 2016;12:178–88.
[138] Qiu C, Panwisawas C, Ward M, Basoalto HC, Brooks JW, Attallah MM. On the role of melt flow into the surface structure and porosity development during selective laser melting. Acta Mater 2015;96:72–9. https://doi.org/10.1016/j.actamat.2015.06.004.
[139] Leitz KH, Grohs C, Singer P, Tabernig B, Plankensteiner A, Kestler H, et al. Fundamental analysis of the influence of powder characteristics in selective laser melting of molybdenum based on a multi-physical simulation model. Int J Refract Met Hard Mater 2018;72:1–8.
[140] Matthews MJ, Guss G, Khairallah SA, Rubenchik AM, Depond PJ, King WE. Denudation of metal powder layers in laser powder-bed fusion processes. Acta Mater 2016;114:33–42.
[141] Wu YC, San CH, Chang CH, Lin H, Marwan R, Baba S, et al. Numerical modeling of melt-pool behavior in selective laser melting with random powder distribution and experimental validation. J Mater Process Technol 2018;254:72–8.
[142] Bayat M, Mohanty S, Hattel JH. Multiphysics modelling of lack-of-fusion voids formation and evolution in IN718 made by multi-track/multi-layer L-PBF. Int J Heat Mass Transf 2019;139:95–114.
[143] Wang L, Felicelli S, Gooroochurn Y, Wang PT, Horstemeyer M. Optimization of the LENS® process for steady molten pool size. Mater Sci Eng A 2008;474: 148–56.
[144] Shen N, Chou K. Thermal modeling of electron beam additive manufacturing process: powder sintering effects. Int Manuf Sci Eng 2013:287–95.
[145] Shen N, Chou K. Simulations of thermo-mechanical characteristics in electron beam additive manufacturing. ASME Int Mech Eng Congr 2013:67–74.
[146] Zhao Y, Aoyagi K, Yamanaka K, Chiba A. Role of operating and environmental conditions in determining molten pool dynamics during electron beam melting and selective laser melting. Addit Manuf 2020;36:101559.
[147] Luding S. From molecular dynamics and particle simulations towards constitutive relations for continuum theory. Adv Comput Methods Sci Eng 2009:453–92.
[148] Monaghan JJ. Why particle methods work. SIAM J Sci Stat Comput 1982;3: 422–33. https://doi.org/10.1137/0903027.
[149] Li S, Liu WK. Meshfree particle methods. 2007.
[150] Cundall PA, Strack ODL. A discrete numerical model for granular assemblies. Geotechnique 1979;29:47–65. https://doi.org/10.1680/GEOT.1979.29.1.47.
[151] Basak A, Das S. Epitaxy and microstructure evolution in metal additive manufacturing. Annu Rev Mat Res 2016;46:125–49. https://doi.org/10.1146/ANNUREV-MATSCI-070115-031728.
[152] Chen LQ. Phase-field models for microstructure evolution. Annu Rev Mater Sci 2002;32:113–40. https://doi.org/10.1146/ANNUREV.MATSCI.32.112001.132041.
[153] Boettinger WJ, Coriell SR, Greer AL, Karma A, Kurz W, Rappaz M, et al. Solidification microstructures: recent developments, future directions. Acta Mater 2000;48:43–70.
[154] Rappaz M, Gandin CA. Probabilistic modelling of microstructure formation in solidification processes. Acta Metall Mater 1993;41:345–60.
[155] Tang M, Pistorius PC, Beuth JL. Prediction of lack-of-fusion porosity for powder bed fusion. Addit Manuf 2017;14:39–48.
[156] Barsoum Z. Residual stress analysis and fatigue of multi-pass welded tubular structures. Eng Fail Anal 2008;15:863–74.
[157] Wu CS, Dorn L. Computer simulation of fluid dynamics and heat transfer in full-penetrated TIG weld pools with surface depression. Comput Mater Sci 1994;2: 341–9.
[158] Aiyiti W, Zhao W, Lu B, Tang Y. Investigation of the overlapping parameters of MPAW-based rapid prototyping. Rapid Prototyp. J. 2006;12:165–72. https://doi.org/10.1108/13552540610670744/FULL/.
[159] Spencer JD, Dickens PM, Wykes CM. Rapid prototyping of metal parts by three-dimensional welding. Proc. Inst. Mech. Eng. Part B J. Eng. Manuf. 1998;212: 175–82. https://doi.org/10.1243/0954405981515590.
[160] Cao Y, Zhu S, Liang X, Wang W. Overlapping model of beads and curve fitting of bead section for rapid manufacturing by robotic MAG welding process. Robot. Comput. Integr. Manuf. 2011;27:641–5.
[161] Gong X, Chou K. Phase-field modeling of microstructure evolution in electron beam additive manufacturing. JOM 2015;67:1176–82. https://doi.org/10.1007/S11837-015-1352-5.
[162] Sahoo S, Chou K. Phase-field simulation of microstructure evolution of Ti–6Al–4V in electron beam additive manufacturing process. Addit Manuf 2016;9:14–24.
[163] Krivilyov MD, Mesarovic SD, Sekulic DP. Phase-field model of interface migration and powder consolidation in additive manufacturing of metals. J Mater Sci 2017; 52:4155–63. https://doi.org/10.1007/S10853-016-0311-Z.
[164] Dowden J, Postacioglu N, Davis M, Kapadia P. A keyhole model in penetration welding with a laser. J Phys D Appl Phys 1987;20.
[165] Beck M, Berger P, Dausinger F, Huegel H. Aspects of keyhole/melt interaction in high-speed laser welding. In: 8th intl symp gas flow chem. lasers; 1991. p. 1397.
[166] Lankalapalli KN, Tu JF, Gartner M. A model for estimating penetration depth of laser welding processes. J Phys D Appl Physics 1996;29.
[167] Ki H, Mohanty PS, Mazumder J. Modeling of laser keyhole welding: part I. Mathematical modeling, numerical methodology, role of recoil pressure, multiple reflections, and free surface evolution. Metall Mater Trans A Phys Metall Mater Sci 2002;33:1817–30. https://doi.org/10.1007/S11661-002-0190-6.
[168] King WE, Barth HD, Castillo VM, Gallegos GF, Gibbs JW, Hahn DE, et al. Observation of keyhole-mode laser melting in laser powder-bed fusion additive manufacturing. J Mater Process Technol 2014;214:2915–25.
[169] Watari N, Ogura Y, Yamazaki N, Inoue Y, Kamitani K, Fujiya Y, et al. Two-fluid model to simulate metal powder bed fusion additive manufacturing. J Fluid Sci Technol 2018;13:JFST0010.
[170] Kruth JP, Froyen L, Rombouts M, Van Vaerenbergh J, Mercells P. New ferro powder for selective laser sintering of dense parts. CIRP Ann 2003;52:139–42.
[171] Teng C, Pal D, Gong H, Zeng K, Briggs K, Patil N, et al. A review of defect modeling in laser material processing. Addit Manuf 2017;14:137–47.
[172] Wei P, Wei Z, Chen Z, He Y, Du J. Thermal behavior in single track during selective laser melting of AlSi10Mg powder. Appl. Phys. A Mater. Sci. Process. 2017;123. https://doi.org/10.1007/S00339-017-1194-9.
[173] Chen Z, Xiang Y, Wei Z, Wei P, Lu B, Zhang L, et al. Thermal dynamic behavior during selective laser melting of K418 superalloy: numerical simulation and

experimental verification. Appl Phys A Mater Sci Process 2018;124. https://doi.org/10.1007/S00339-018-1737-8.
[174] Le VD, Pessard E, Morel F, Prigent S. Fatigue behaviour of additively manufactured Ti-6Al-4V alloy: the role of defects on scatter and statistical size effect. Int J Fatigue 2020;140:105811.
[175] Galarraga H, Lados DA, Dehoff RR, Kirka MM, Nandwana P. Effects of the microstructure and porosity on properties of Ti-6Al-4V ELI alloy fabricated by electron beam melting (EBM). Addit Manuf 2016;10:47–57. https://doi.org/10.1016/j.addma.2016.02.003.
[176] Wan H, Wang Q, Jia C, Zhang Z. Multi-scale damage mechanics method for fatigue life prediction of additive manufacture structures of Ti-6Al-4V. Mater Sci Eng A 2016;669:269–78. https://doi.org/10.1016/J.MSEA.2016.05.073.
[177] Qi HB, Yan YN, Lin F, Zhang RJ. Scanning method of filling lines in electron beam selective melting. Proc Inst Mech Eng Part B 2007;221:1685–94. https://doi.org/10.1243/09544054JEM913.
[178] Cheng B, Chou K. Thermal stresses associated with part overhang geometry in electron beam additive manufacturing: process parameter effects. 2014.
[179] Cheng B, Chou K. Geometric consideration of support structures in part overhang fabrications by electron beam additive manufacturing. Comput Des 2015;69:102–11.
[180] Singh A, Haase C, Barrales-Mora LA. Cellular automaton simulation model for predicting the microstructure evolution of an additively manufactured X30Mn21 austenitic advanced high-strength steel. Metals (Basel) 2025;15:770. https://doi.org/10.3390/met15070770.
[181] Pourmand S, Kermanpur A, Rezaeian A, Jafari-Ramiani A. Phase field simulation of solidification microstructure for Fe-17 wt%Cr model alloy fabricated by laser powder bed fusion. Mater Des 2025;260:115226. https://doi.org/10.1016/j.matdes.2025.115226.
[182] Ling P-H, Jiang W-G, Zhan Z-C, Chen T, Qin Q-H, Mao L-H. Insights into microstructural variations in GH4169 thin-walled parts by laser powder bed fusion: a coupling finite-element/cellular-automaton study. Acta Mech Sin 2025;42:124808. https://doi.org/10.1007/s10409-025-24808-x.
[183] Dezfoli ARA, Lo Y-L, Raza MM. Prediction of epitaxial grain growth in single-track laser melting of IN718 using integrated finite element and cellular automaton approach. Materials (Basel) 2021;14.
[184] Ma L, Liu H, Williams M, Levine L, Ramazani A. Integrating phase field modeling and machine learning to develop process-microstructure relationships in laser powder bed fusion of IN718. Metallogr Microstruct Anal 2024;13:983–95. https://doi.org/10.1007/s13632-024-01130-w.
[185] Zaeh MF, Branner G. Investigations on residual stresses and deformations in selective laser melting. Prod Eng 2010;4:35–45. https://doi.org/10.1007/s11740-009-0192-y.
[186] Patil N, Pal D, Stucker B. A new finite element solver using numerical eigen modes for fast simulation of additive manufacturing processes. 2013.
[187] Denlinger ER, Irwin J. Thermomechanical modeling of additive manufacturing large parts. J Manuf Sci Eng 2014;136:061007.
[188] Matsumoto M, Shiomi M, Osakada K, Abe F. Finite element analysis of single layer forming on metallic powder bed in rapid prototyping by selective laser processing. Int J Mach Tools Manuf 2002;41:61–7. https://www.sciencedirect.com/science/article/pii/S0890695501000931.
[189] Ravichandran K. Calibrating inherent strain for additive manufacturing an investigation of different subscale geometries. 2020.
[190] Zhang M, Ji C, Hou Y, Jin P, He J, Wu J, et al. Modified inherent strain method coupled with shear strain and dynamic mechanical properties for predicting residual deformation of Inconel 738LC part fabricated by laser powder bed fusion. Int. J. Therm. Sci. 2024;203:109163.
[191] Lorin S, Sagar VR, Cromvik C, Edelvik F, Wärmefjord K, Söderberg R. Geometry prediction simulation for metal additive manufacturing: a calibration-free approach. Adv. Manuf. 2024;2.
[192] Dong W, Jimenez XA, To AC. Temperature-dependent modified inherent strain method for predicting residual stress and distortion of Ti6Al4V walls manufactured by wire-arc directed energy deposition. Addit Manuf 2023;62:103386.
[193] Bellet M, Tematio JK, Zhang Y. The inherent strain method for additive manufacturing: critical analysis and new inherent strain rate method. IOP Conf. Ser. Mater. Sci. Eng. 2023;1281.
[194] Downing D, Leary M, McMillan M, Alghamdi A, Brandt M. Heat transfer in lattice structures during metal additive manufacturing: numerical exploration of temperature field evolution. Rapid Prototyp. J. 2020;26:911–28. https://doi.org/10.1108/RPJ-11-2018-0288.
[195] Cao S, Qiu Y, Wei XF, Zhang HH. Experimental and theoretical investigation on ultra-thin powder layering in three dimensional printing (3DP) by a novel double-smoothing mechanism. J Mater Process Technol 2015;220:231–42. https://doi.org/10.1016/J.JMATPROTEC.2015.01.016.
[196] Xia M, Gu D, Yu G, Dai D, Chen H, Shi Q. Porosity evolution and its thermodynamic mechanism of randomly packed powder-bed during selective laser melting of Inconel 718 alloy. Int J Mach Tools Manuf 2017;116:96–106. https://doi.org/10.1016/J.IJMACHTOOLS.2017.01.005.
[197] Yan W, Lian Y, Yu C, Kafka OL, Liu Z, Liu W, et al. An integrated process–structure–property modeling framework for additive manufacturing. Comput Methods Appl Mech Eng 2018;339:184–204.
[198] Bai Y, Wagner G, Williams CB. Effect of particle size distribution on powder packing and sintering in binder jetting additive manufacturing of metals. J Manuf Sci Eng Trans ASME 2017;139. https://doi.org/10.1115/1.4036640.
[199] Karapatis NP, Egger G, Gygax P-E, Glardon R. Optimization of powder layer density in selective laser sintering. 1999.
[200] Zhou J, Zhang Y, Chen JK. Numerical simulation of random packing of spherical particles for powder-based additive manufacturing. J Manuf Sci Eng 2009;131:310041–8. https://doi.org/10.1115/1.3123324.
[201] Yan W, Ge W, Qian Y, Lin S, Zhou B, Liu WK, et al. Multi-physics modeling of single/multiple-track defect mechanisms in electron beam selective melting. Acta Mater 2017;134:324–33. https://doi.org/10.1016/J.ACTAMAT.2017.05.061.
[202] Khairallah SA, Anderson AT, Rubenchik A, King WE. Laser powder-bed fusion additive manufacturing: physics of complex melt flow and formation mechanisms of pores, spatter, and denudation zones. Acta Mater 2016;108:36–45. https://doi.org/10.1016/j.actamat.2016.02.014.
[203] Martin AA, Calta NP, Khairallah SA, Wang J, Depond PJ, Fong AY, et al. Dynamics of pore formation during laser powder bed fusion additive manufacturing. Nat Commun 2019;10:1987. https://doi.org/10.1038/s41467-019-10009-2.
[204] Zhao C, Parab ND, Li X, Fezzaa K, Tan W, Rollett AD, et al. Critical instability at moving keyhole tip generates porosity in laser melting. Science 2020;370:1080–6. https://doi.org/10.1126/science.abd1587.
[205] Cunningham R, Zhao C, Parab N, Kantzos C, Pauza J, Fezzaa K, et al. Keyhole threshold and morphology in laser melting revealed by ultrahigh-speed x-ray imaging. Science 2019;363:849–52. https://doi.org/10.1126/science.aav4687.
[206] Roberts IA, Wang CJ, Esterlein R, Stanford M, Mynors DJ. A three-dimensional finite element analysis of the temperature field during laser melting of metal powders in additive layer manufacturing. Int J Mach Tools Manuf 2009;49:916–23. https://doi.org/10.1016/j.ijmachtools.2009.07.004.
[207] Song X, Feih S, Zhai W, Sun C-N, Li F, Maiti R, et al. Advances in additive manufacturing process simulation: residual stresses and distortion predictions in complex metallic components. Mater. Des. 2020;193:108779. https://doi.org/10.1016/j.matdes.2020.108779.
[208] Rashid A, Gopaluni A. A review of residual stress and deformation modeling for metal additive manufacturing processes. Chin J Mech Eng Addit Manuf Front 2023;2:100102. https://doi.org/10.1016/j.cjmeam.2023.100102.
[209] Herzog D, Seyda V, Wycisk E, Emmelmann C. Additive manufacturing of metals. Acta Mater 2016. https://doi.org/10.1016/j.actamat.2016.07.019.
[210] Yang M, Wang L, Yan W. Phase-field modeling of grain evolutions in additive manufacturing from nucleation, growth, to coarsening. Npj Comput Mater 2021;7:56. https://doi.org/10.1038/s41524-021-00524-6.
[211] Shi L, Lyu X, Chen J, Wu C, Kumar A, Zhai M, et al. Multi-scale simulation of thermal processes and microstructure evolution in wire arc additive manufacturing of 921A steel. Mater Solidif 2025;1:9580003. https://doi.org/10.26599/MAS.2025.9580003.
[212] Ling Y, Ni J, Antonissen J, Ben Hamouda H, Vande Voorde J, Abdel Wahab M. Numerical prediction of microstructure and hardness for low carbon steel wire Arc additive manufacturing components. Simul Model Pract Theory 2023;122:102664. https://doi.org/10.1016/j.simpat.2022.102664.
[213] Yong W, Zhang G, Wang J, Gui Y, Fu C, Fu H. Finite element modeling and simulation of IN738 laser powder bed fusion process assisted via machine learning. Mater Today Commun 2024;40:109848. https://doi.org/10.1016/j.mtcomm.2024.109848.
[214] Tian M, Mu H, Liu T, Li M, Ding D, Zhao J. Physics-informed machine learning-based real-time long-horizon temperature fields prediction in metallic additive manufacturing. Commun Eng 2025;4:168. https://doi.org/10.1038/s44172-025-00501-7.
[215] Afrasiabi M, Lüthi C, Bambach M, Wegener K. Multi-resolution SPH simulation of a laser powder bed fusion additive manufacturing process. Appl Sci 2021;11:2962. https://doi.org/10.3390/app11072962.
[216] Körner C, Bauereiß A, Attar E. Fundamental consolidation mechanisms during selective beam melting of powders. Model Simul Mater Sci Eng 2013;21:085011. https://doi.org/10.1088/0965-0393/21/8/085011.
[217] Lu X, Lin X, Chiumenti M, Cervera M, Hu Y, Ji X, et al. Residual stress and distortion of rectangular and S-shaped Ti-6Al-4V parts by directed energy deposition: modelling and experimental calibration. Addit Manuf 2019;26:166–79. https://doi.org/10.1016/j.addma.2019.02.001.
[218] Ding J, Colegrove P, Mehnen J, Ganguly S, Almeida PMS, Wang F, et al. Thermo-mechanical analysis of Wire and Arc Additive Layer Manufacturing process on large multi-layer parts. Comput Mater Sci 2011;50:3315–22. https://doi.org/10.1016/j.commatsci.2011.06.023.
[219] Montevecchi F, Venturini G, Scippa A, Campatelli G. Finite element modelling of wire-arc-additive-manufacturing process. Procedia CIRP 2016;55:109–14. https://doi.org/10.1016/j.procir.2016.08.024.
[220] Graf M, Hälsig A, Höfer K, Awiszus B, Mayr P. Thermo-mechanical modelling of wire-arc additive manufacturing (WAAM) of semi-finished products. Metals (Basel) 2018;8:1009. https://doi.org/10.3390/met8121009.
[221] Ou W, Knapp GL, Mukherjee T, Wei Y, DebRoy T. An improved heat transfer and fluid flow model of wire-arc additive manufacturing. Int. J. Heat Mass Transf. 2021;167:120835. https://doi.org/10.1016/j.ijheatmasstransfer.2020.120835.
[222] Weisz-Patrault D. Fast simulation of temperature and phase transitions in directed energy deposition additive manufacturing. Addit Manuf 2020;31:100990. https://doi.org/10.1016/j.addma.2019.100990.
[223] Liao Z, Zhang Y, Chen J, Ouyang J, Chen H. Finite element simulation of selective laser melting based on the layer thickness-dependent shrinkage ratio model. Opt Laser Technol 2024;174:110565. https://doi.org/10.1016/j.optlastec.2024.110565.
[224] Yeganeh M, Shahryari Z, Shoushtari MT, Eskandari M. Discontinuities in the laser powder bed fusion alloys: a review. J Mater Res Technol 2025;37:3193–229. https://doi.org/10.1016/j.jmrt.2025.06.202.

[225] Wahlquist S, Ali A. Roles of modeling and artificial intelligence in LPBF metal print defect detection: critical review. Appl. Sci. 2024;14. https://doi.org/10.3390/app14188534.
[226] Goh GD, Sing SL, Yeong WY. A review on machine learning in 3D printing: applications, potential, and challenges. Artif Intell Rev 2021;54:63–94. https://doi.org/10.1007/s10462-020-09876-9.
[227] AlFaify A, Hughes J, Ridgway K. Controlling the porosity of 316L stainless steel parts manufactured via the powder bed fusion process. Rapid Prototyp. J. 2019; 25:162–75. https://doi.org/10.1108/RPJ-11-2017-0226/FULL/HTML.
[228] Tapia G, Elwany AH, Sang H. Prediction of porosity in metal-based additive manufacturing using spatial Gaussian process models. Addit. Manuf. 2016;12: 282–90.
[229] Garg A, Lam JSL, Savalani MM. A new computational intelligence approach in formulation of functional relationship of open porosity of the additive manufacturing process. Int J Adv Manuf Technol 2015;80:555–65. https://doi.org/10.1007/s00170-015-6989-2.
[230] Ghibaudo C, Maculotti G, Gobber F, Saboori A, Galetto M, Biamino S, et al. Information-rich quality controls prediction model based on non-destructive analysis for porosity determination of AISI H13 produced by electron beam melting. Int J Adv Manuf Technol 2023;126:1159–73. https://doi.org/10.1007/s00170-023-11153-2.
[231] Li J, Zhou Q, Cao L, Wang Y, Hu J. A convolutional neural network-based multi-sensor fusion approach for in-situ quality monitoring of selective laser melting. J. Manuf. Syst. 2022;64:429–42.
[232] Song Z, Wang X, Gao Y, Son J, Wu J. A hybrid deep generative network for pore morphology prediction in metal additive manufacturing. J Manuf Sci Eng 2023; 145:071005.
[233] Imani F, Chen R, Diewald E, Reutzel E, Yang H. Deep learning of variant geometry in layerwise imaging profiles for additive manufacturing quality control. J Manuf Sci Eng 2019;14:111001.
[234] Scime L, Beuth J. A multi-scale convolutional neural network for autonomous anomaly detection and classification in a laser powder bed fusion additive manufacturing process. Addit Manuf 2018;24:273–86.
[235] Parab ND, Zhao C, Cunningham R, Escano LI, Fezzaa K, Everhart W, et al. Ultrafast X-ray imaging of laser–metal additive manufacturing processes. J Synchrotron Radiat 2018;25:1467–77. https://doi.org/10.1107/S1600577518009554.
[236] Sun T. Probing ultrafast dynamics in laser powder bed fusion using high-speed X-ray imaging: a review of research at the advanced photon source. JOM 2020;72: 999–1008. https://doi.org/10.1007/S11837-020-04015-9.
[237] Guo Q, Zhao C, Qu M, Xiong L, Escano LI, Hojjatzadeh S, et al. In-situ characterization and quantification of melt pool variation under constant input energy density in laser powder bed fusion additive manufacturing. Addit Manuf 2019;28:600–9.
[238] Kong L, Peng X, Chen Y. Fast and accurate defects detection for additive manufactured parts by multispectrum and machine learning. 3D Print Addit Manuf 2023;10:393–405. https://doi.org/10.1089/3DP.2021.0191.
[239] Zhao W, Chen F, Huang H, Li D, Cheng W. A new steel defect detection algorithm based on deep learning. Comput Intell Neurosci 2021;2021. https://doi.org/10.1155/2021/5592878.
[240] Zubayer MH, Zhang C, Wang Y. Deep learning-based automatic defect detection of additive manufactured stainless steel. Met (Basel) 2023;13:1987.
[241] Jiang Z, Zhang A, Chen Z, Ma C, Yuan Z, Deng Y, et al. A deep convolutional network combining layerwise images and defect parameter vectors for laser powder bed fusion process anomalies classification. J Intell Manuf 2024;35: 2929–59. https://doi.org/10.1007/S10845-023-02183-4.
[242] Ansari MA, Crampton A, Parkinson S. A layer-wise surface deformation defect detection by convolutional neural networks in laser powder-bed fusion images. Mater (Basel) 2022;15:7166.
[243] Bugatti M, Colosimo BM. Towards real-time in-situ monitoring of hot-spot defects in L-PBF: a new classification-based method for fast video-imaging data analysis. J Intell Manuf 2022;33:293–309. https://doi.org/10.1007/S10845-021-01787-Y.
[244] Aminzadeh M, Kurfess TR. Online quality inspection using Bayesian classification in powder-bed additive manufacturing from high-resolution visual camera images. J Intell Manuf 2019;30:2505–23. https://doi.org/10.1007/S10845-018-1412-0.
[245] Liu T, Huang L, Chen B. Real-time defect detection of laser additive manufacturing based on support vector machine. J Phys Conf Ser 2019;1213: 052043.
[246] Li J, Zhang X, Ma F, Wang S, Huang Y. Simultaneous pore detection and morphological features extraction in laser powder bed fusion with image processing. Mater. (Basel). 2024;17:1373.
[247] Li J, Cao L, Xu J, Wang S, Zhou Q. In situ porosity intelligent classification of selective laser melting based on coaxial monitoring and image processing. Measurement 2022;187:110232.
[248] Schwerz C, Nyborg L. A neural network for identification and classification of systematic internal flaws in laser powder bed fusion. CIRP J Manuf Sci Technol 2022;37:312–8.
[249] Yuan B, Giera B, Guss G, Matthews I, McMains S. Semi-supervised convolutional neural networks for in-situ video monitoring of selective laser melting. In: 2019 IEEE winter conf. appl. comput. vis; 2019. p. 744–53.
[250] Khanzadeh M, Chowdhury S, Marufuzzaman M, Tschopp M, Bian L. Porosity prediction: supervised-learning of thermal history for direct laser deposition. J. Manuf. Syst. 2018;47:69–82.
[251] Forien JB, Guss GM, Khairallah SA, Smith WL, Depond P, Matthews MJ, et al. Detecting missing struts in metallic micro-lattices using high speed melt pool thermal monitoring. Addit. Manuf. Lett. 2023;4:100112.
[252] Oster S, Scheuschner N, Chand K, Altenburg SJ, Gerlach G. Potentials and challenges of deep-learningassisted porosity prediction based on thermographic in situ monitoring in laser powder bed fusion. Tech Mess 2023;90:85–96. https://doi.org/10.1515/TEME-2023-0062/HTML.
[253] Baumgartl H, Tomas J, Buettner R, Merkel M. A deep learning-based model for defect detection in laser-powder bed fusion using in-situ thermographic monitoring. Prog Addit Manuf 2020;5:277–85. https://doi.org/10.1007/S40964-019-00108-3.
[254] Ito K, Kusano M, Demura M, Watanabe M. Detection and location of microdefects during selective laser melting by wireless acoustic emission measurement. Addit Manuf 2021;40:101915.
[255] Kononenko DY, Nikonova V, Seleznev M, Van den Brink J, Chernyavsky D. An in situ crack detection approach in additive manufacturing based on acoustic emission and machine learning. Addit. Manuf. Lett. 2023;5:100130.
[256] Pandiyan V, Drissi-Daoudi R, Shevchik S, Masinelli G. Analysis of time, frequency and time-frequency domain features from acoustic emissions during laser powder-bed fusion process. Procedia CIRP 2020;94:392–7.
[257] Ye J, Poudel A, Liu J, Vinel A, Silva D, Shao S, et al. Machine learning augmented X-ray computed tomography features for volumetric defect classification in laser beam powder bed fusion. Int J Adv Manuf Technol 2023;126:3093–107. https://doi.org/10.1007/S00170-023-11281-9.
[258] Vandecasteele M, Heylen R, Iuso D, Thanki A, Philips W, Witvrouw A, et al. Towards material and process agnostic features for the classification of pore types in metal additive manufacturing. Mater. Des. 2023;227:111757.
[259] Aziz U, Bradshaw A, Lim J, Thomas M. Classification of defects in additively manufactured nickel alloys using supervised machine learning. Mater Sci Technol (United Kingdom) 2023;39:2464–8. https://doi.org/10.1080/02670836.2023.2207337.
[260] Minerva G, Awd M, Tenkamp J, Walther F, Beretta S. Machine learning-assisted extreme value statistics of anomalies in AlSi10Mg manufactured by L-PBF for robust fatigue strength predictions. Mater. Des. 2023;235:112392.
[261] Ansari MA, Crampton A, Garrard R, Cai B, Attallah M. A convolutional neural network (CNN) classification to identify the presence of pores in powder bed fusion images. Int J Adv Manuf Technol 2022;120:5133–50.
[262] Scime L, Beuth J. Anomaly detection and classification in a laser powder bed additive manufacturing process using a trained computer vision algorithm. Addit Manuf 2017;19. https://doi.org/10.1016/j.addma.2017.11.009.
[263] Grasso M, Laguzza V, Semeraro Q, Colosimo BM. In-process monitoring of selective laser melting: spatial detection of defects via image data analysis. J Manuf Sci Eng 2017;139:51001.
[264] Grasso M, Demir AG, Previtali B, Colosimo BM. In situ monitoring of selective laser melting of zinc powder via infrared imaging of the process plume. Robot. Comput. Integr. Manuf. 2018;49:229–39.
[265] Vasileska E, Demir AG, Colosimo BM, Previtali B. A novel paradigm for feedback control in LPBF: layer-wise correction for overhang structures. Adv Manuf 2022; 10:326–44. https://doi.org/10.1007/S40436-021-00379-6.
[266] Taherkhani K, Eischer C, Toyserkani E. An unsupervised machine learning algorithm for in-situ defect-detection in laser powder-bed fusion. J Manuf Process 2022;81.
[267] Snell R, Tammas-Williams S, Chechik L, Lyle A, Hernández-Nava E, Boig C, et al. Methods for rapid pore classification in metal additive manufacturing. JOM 2020; 72:101–9. https://doi.org/10.1007/s11837-019-03761-9.
[268] Bordekar H, Cersullo N, Brysch M, Philipp J, Hühne C. eXplainable artificial intelligence for automatic defect detection in additively manufactured parts using CT scan analysis. J Intell Manuf 2023. https://doi.org/10.1007/S10845-023-02272-4.
[269] Okaro IA, Jayasinghe S, Sutcliffe C, Black K, Paoletti P, Green PL. Automatic fault detection for laser powder-bed fusion using semi-supervised machine learning. Addit Manuf 2019;27:42–53.
[270] Yadav P, Singh VK, Joffre T, Rigo O, Arvieu C, Le Guen E, et al. Inline drift detection using monitoring systems and machine learning in selective laser melting. Adv Eng Mater 2020;22. https://doi.org/10.1002/ADEM.202000660.
[271] Li X, Jia X, Yang Q, Lee J. Quality analysis in metal additive manufacturing with deep learning. J Intell Manuf 2020;31:2003–17. https://doi.org/10.1007/S10845-020-01549-2.
[272] Nguyen NV, Hum AJW, Do T, Tran T. Semi-supervised machine learning of optical in-situ monitoring data for anomaly detection in laser powder bed fusion. Virtual Phys Prototyp 2022;18. https://doi.org/10.1080/17452759.2022.2129396.
[273] Liu J, Guo F, Zhang Y, Hou B, Zhou H. Defect classification on limited labeled samples with multiscale feature fusion and semi-supervised learning. Appl Intell 2022;52:8243–58. https://doi.org/10.1007/S10489-021-02917-Y.
[274] Nguyen NV, Hum AJW, Tran T. A semi-supervised machine learning approach for in-process monitoring of laser powder bed fusion. Mater Today Proc 2022;70: 583–6.
[275] Wasmer K, Le-Quang T, Meylan B, Shevchik SA. In situ quality monitoring in AM using acoustic emission: a reinforcement learning approach. J. Mater. Eng. Perform. 2019;28:666–72. https://doi.org/10.1007/S11665-018-3690-2.
[276] Yao B, Yang H. Constrained Markov decision process modeling for sequential optimization of additive manufacturing build quality. IEEE Access 2018: 54786–94.

[277] Knaak C, Masseling L, Duong E, Abels P, Gillner A. Improving build quality in laser powder bed fusion using high dynamic range imaging and model-based reinforcement learning. IEEE Access 2021;9:55214–31.
[278] Ziabari A, Venkatakrishnan S, Dubey A, Lisovich A, Brackman P, Frederick C, et al. Simurgh: a framework for CAD-driven deep learning based X-ray CT reconstruction. In: 2022 IEEE Int. Conf. Image Process; 2022. p. 3836–67.
[279] Cannizzaro D, Varrella AG, Paradis S, Sampieri R, Chen Y, Macii A, et al. In-situ defect detection of metal additive manufacturing: an integrated framework. IEEE Trans Emerg Top Comput 2022;10:74–86.
[280] Liu R, Liu S, Zhang X. A physics-informed machine learning model for porosity analysis in laser powder bed fusion additive manufacturing. Int J Adv Manuf Technol 2021;113:1943–58. https://doi.org/10.1007/s00170-021-06640-3.
[281] Kim J, Yang Z, Lu Y. A physics-guided deep generative model for predicting melt pool behavior in laser powder bed fusion additive manufacturing. J Intell Manuf 2025;36:5715–35. https://doi.org/10.1007/s10845-024-02504-1.
[282] Du Y, Mukherjee T, DebRoy T. Physics-informed machine learning and mechanistic modeling of additive manufacturing to reduce defects. Appl Mater Today 2021;24:101123. https://doi.org/10.1016/j.apmt.2021.101123.
[283] Gui Y, Aoyagi K, Bian H, Chiba A. Detection, classification and prediction of internal defects from surface morphology data of metal parts fabricated by powder bed fusion type additive. Addit Manuf 2022;54:102736.
[284] Le Roux L, Liu C, Ji Z, Kerfriden P, Gage D, Feyer F, et al. Automatised quality assessment in additive layer manufacturing using layer-by-layer surface measurements and deep learning. Procedia CIRP 2021;99:342–7.
[285] Martone F, Leoncini P, Fusco G, Toscano C. A combined Neural Network/3D image analysis approach to defect detection in EBM ALM imaging. In: 2022 IEEE 9th int. work. metrol. aerosp; 2022. p. 275–80.
[286] Mohammed AS, Almutahhar M, Sattar K, Alhajeri A, Nazir A, Ali U. Deep learning based porosity prediction for additively manufactured laser powder-bed fusion parts. J Mater Res Technol 2023;27:7330–5. https://doi.org/10.1016/j.jmrt.2023.11.130.
[287] Xie J, Sun L, Zhao YF. On the data quality and imbalance in machine learning-based design and manufacturing—a systematic review. Engineering 2025;45:105–31. https://doi.org/10.1016/j.eng.2024.04.024.
[288] Dongsen Y, Fuh J, Zhang Y, Hong G-S, Zhu K. Defects recognition in selective laser melting with acoustic signals by SVM based on feature reduction. IOP Conf Ser Mater Sci Eng 2018;436:12020.